Dissertation

submitted to the

Combined Faculties of the Natural Sciences and Mathematics

of the Ruperto-Carola-University of Heidelberg, Germany

for the degree of

Doctor of Natural Sciences

Put forward by

Stefan Lieder

born in: Torgau, Germany

Oral examination: May 26, 2014

FOSSIL GROUPS IN THE COURSE OF GALAXY EVOLUTION

STEFAN LIEDER

REFEREES

Priv.-Doz. Dr. Thorsten Lisker
Prof. Dr. Volker Springel

EXAMINERS

Prof. Dr. Klaus Meisenheimer
Prof. Dr. Ulrich Uwer

March 2014

ABSTRACT

Fossil groups are X-ray bright galaxy groups characterized by a central elliptical galaxy that dominates the total light of the group in the optical. We present here a photometric analysis of the nearest fossil group NGC 6482 down to $M_r \simeq -10.5$ mag — to our knowledge the deepest fossil group study yet, which can probe its faint satellite system in a meaningful way. We find signatures that the brightest group galaxy must have undergone a gas-rich merger in the past, favoring the cannibalism scenario for NGC 6482, i.e., the brightest galaxies in the group center have merged to form the dominant central elliptical. We find the faint-end slope of the luminosity function to be within the range of values typically found in ordinary cluster environments. We thus conclude that the NGC 6482 fossil group shows photometric properties consistent with those of regular galaxy clusters and groups, including a normal abundance of faint satellites. We additionally investigate fossil groups in a state-of-the-art semi-analytical model. From a sample of 59 fossil groups with masses comparable to NGC 6482 we find that their properties are similar to non-fossil systems. Both reside in similarly dense environments and have similar number density distributions of dwarf galaxies. We do not find a "missing satellite problem" in the semi-analytical model. The faint-end slopes of the luminosity functions cover a range that is covered by observations. In particular, the faint-end slope of NGC 6482 is in good agreement with the slopes determined in the 59 fossil groups of the model. Specifically, we confirm the picture of a transient fossil phase as both fossil and non-fossil systems spent similar time periods in the fossil phase. Therefore, this suggests that fossil and non-fossil groups are representations of the same evolutionary track of ordinary galaxy groups, supporting the cannibalism scenario. From the perspective of galaxy evolution there is no difference between fossil and non-fossil systems.

ZUSAMMENFASSUNG

Fossile Gruppen sind Galaxiengruppen, die im Röntgenlicht hell erscheinen und sich durch eine zentrale elliptische Galaxie auszeichnen, deren optisches Licht das der gesamten Gruppe dominiert. Wir präsentieren hier eine photometrische Analyse der nächsten Fossilen Gruppe NGC 6482 bis zu aboluten Helligkeiten von $M_r \simeq -10.5$ mag — nach unserem Kenntnisstand ist das die tiefste Studie einer Fossilen Gruppe, die es ermöglicht, deren System lichtschwacher Galaxien aussagekräftig zu erforschen. Wir finden Anzeichen, dass die hellste Gruppengalaxie einen gasreichen Verschmelzungsprozess hinter sich hat, was für das Kannibalismus Szenario für NGC 6482 spricht, d.h., die dominante, zentrale Galaxie ist aus einer Verschmelzung der hellsten Gruppengalaxien entstanden. Wir finden eine Steigung des lichtschwachen Endes der Leuchtkraftfunktion, die in Einklang mit publizierten Werten normaler Galaxienhaufen ist. Wir folgern daher, dass die Fossile Gruppe NGC 6482 photometrische Eigenschaften normaler Galaxienhaufen und -gruppen besitzt, einschließlich eines normalen Reichtums lichtschwacher Satellitengalaxien. Darüberhinaus untersuchen wir Fossile Gruppen in einem der neuesten semi-analytischen Modelle. In einer Auswahl von 59 Fossilen Gruppen, mit Massen vergleichbar zu NGC 6482, finden wir heraus, dass diese Eigenschaften haben ähnlich derer nicht-fossiler Systeme. Beide Typen befinden sich in ähnlich dichten Umgebungen und haben einen

ähnlichen Reichtum an Zwerggalaxien. Wir finden kein "missing satellite"-Problem im semi-analytischen Model. Insbesondere bestätigen wir das Bild einer vergänglichen fossilen Phase, da sowohl fossile als auch nicht-fossile Systeme ähnliche Zeiträume in der fossilen Phase verbringen. Daher folgern wir, dass fossile und nicht-fossile Gruppen Repäsentationen ein und derselben Entwicklung von gewöhnlichen Galaxiengruppen sind, was das Kannibalismus Szenario unterstützt. Aus der Sicht der Galaxienentwicklung bestehen keine Unterschiede zwischen Fossilen Gruppen und deren nicht-fossilen Pendants.

PUBLICATIONS

1. Lieder et al. 2013, A&A 559, A67:
   A normal abundance of faint satellites in the fossil group NGC 6482

REFEREED PUBLICATION THAT IS NOT PART OF THIS THESIS

2. Lieder, Lisker et al. 2012, A&A 538, A69:
   A deep view on the Virgo cluster core

DECLARATION

This thesis contains no material that has been accepted for the award of any other degree or diploma.

Heidelberg, March 2014

Stefan Lieder

CONTENTS

Part I

INTRODUCTION

INTRODUCTION

1.1 COSMOLOGY

About a hundred years ago, Einstein (1916) presented a set of equations to describe gravitational processes comprehensively. His theory, commonly known as General Theory of Relativity, treated gravitation as a geometrical property of space and time and gave physicists a tool to answer fundamental questions about the Universe. In the 1920's and 1930's several scientists developed a homogeneous and isotropic class of universe models based on a curved spacetime that is the foundation of the cosmological standard model (Friedmann 1922; Lemaître 1927; Robertson 1929; Walker 1935). Its application to Einstein's field equations revealed that space has an expanding nature. Independently, Lemaître (1927) and Hubble (1929) concluded that an expanding universe causes the observed increasing recessional velocity[1] of galaxies with increasing distance from Earth. It was the first convincing cosmological evidence that the Universe is actually expanding. In return, Lemaître (1931) concluded that – if going back in time – all energy must have been packed in a "unique quantum". The Universe began as a very hot and very dense spot and is expanding since. This model of a hot *Big Bang* became the standard model of cosmology (see the monumental Weinberg 1972 for a review).

In the 1960's first doubts arose concerning the Big Bang model. In the Friedmann-Lemaître-Robertson-Walker (FLRW) models the Universe was nearly flat in the beginning and its curvature evolves away from flatness if the Universe is dominated by either matter or radiation. That we seem to live in a flat universe today (Hinshaw *et al.* 2013) is a very special case and known as the *flatness problem* (Dicke & Peebles 1979). On large scales, the Universe is homogeneous (Maddox *et al.* 1990). If this is a result of physical processes occurring shortly after the Big Bang, the question arises how different regions right after the Big Bang can be causally connected since information can propagate only with speed of light. In conclusion, the large-scale homogeneity must be an initial condition. This striking problem is called *horizon problem* (Rindler 1956 for a general discussion, McCrea 1968 and Misner 1969 for the first awareness of the problem, and the celebrated Dicke & Peebles 1979 for a review). Another problem is given by the structure of the present universe. Stars, galaxies and galaxy clusters have grown by gravitational instability. There must have been a seed for this growth. A causing perturbation must also be considered as initial condition for the Big Bang – known as *structure problem*. Guth (1981) and Linde (1982, 1983) proposed a phase of accelerated expansion in the very early universe – called *inflation* – in order to solve all the three mentioned problems. The phase is characterized by a domination of vacuum energy – which Einstein called cosmological parameter Λ in his equations – that drives the Universe naturally flat. It suggests that our universe even today is practically flat. This is supported by observations as indicated in Fig. 1.

Inflation also solves the horizon problem since the region in causal contact becomes arbitrarily large between the Big Bang in the inflationary phase. According to the theory by Guth and Linde, at temperatures greater than 10^{27}K (Grand Unification) matter was in a state known in

1 Hubble took spectra of galaxies and observed that they were redshifted. He supposed that the redshift origins from a Doppler shift, i.e., the galaxy is moving away from us – it recedes. The farther away a galaxy the longer it took the light to reach us but also the higher its redshift as Hubble observed. Therefore, redshift describes the same fact (in a first approximation) as lookback time and distance do. In astronomy, those three expressions are often arbitrarily replaced by each other.

quantum field theory as vacuum. In this vacuum, quantum fluctuations can occur, i.e., temporary changes of the amount of energy in a point in space as predicted by Heisenberg's uncertainty principle. For a virtual time Δt a particle-antiparticle pair with the energy ΔE is created. During inflation the scale length of quantum fluctuations grow faster than the horizon expands so that initially causally connected quantum fluctuations become suddenly supra-horizon (curvature) perturbations. After inflation, the horizon continues to expand and the perturbations cross the horizon again and become true density perturbations (see Lyth & Riotto 1999 for a review on physical models of inflation). These density perturbations will cause gravitational instabilities.

Summarizing, quantum fluctuations are proposed to cause density perturbations which are the seeds of the structures of the Universe we observe today. Thus inflation predicts structure growth (see Sect. 1.2). Guth (1981) also mentions that all initial inhomogeneities and anisotropies are smoothed and inflation naturally results in a "huge region of space which is homogeneous and isotropic". Inflation is thought to end in a transition phase when "inflating" matter is converted to ordinary matter (including dark matter, see below) and radiation. But in this picture the Big Bang is not looking like an expanding fireball anymore (Linde *et al.* 1994). Instead, we are now considering a huge amount of inflating balls (Guth calls it "bubbles") producing new balls, producing new balls, etc. And although inflation solves many problems and plays a major role in cosmology, it should kept in mind that it is only a hypothesis and not supported by any other field of physics.

Following inflation, the Universe was very hot and radiation-dominated. Photons can create spontaneously matter–antimatter pairs which again "immediately" annihilate. A macroscopic separation of matter from antimatter therefore should be excluded. One the other hand, today we observe a matter-dominated universe. It was pointed out first by Sakharov (1967) that baryon number violation (essentially needed to form a baryon excess), CP and C violation as well as interaction without being in thermal equilibrium (both to maintain the baryon excess) are conditions that can form a matter-dominated universe. The interested reader is referred to Dine & Kusenko (2003) for a review of *baryogenesis* – how the baryon excess is formed. As a result of this asymmetric process we can assume that once the temperature of the Universe has dropped below $\sim 10^{12}$K, approximately 10^{-4}s after the Big Bang, its constituents are all known (and unknown) matter particles like photons, electrons, neutrinos, protons and neutrons, and maybe a species of dark matter (see Sect.1.2). As the Universe continues to expand, particles drift out of thermal equilibrium. About 1s after the Big Bang at temperatures around 10^{10}K weak interactions, that had kept neutron/proton ratio in equilibrium, were not possible anymore so that this ratio was frozen at 0.25 (Beringer *et al.* 2012). But long before the remaining free neutrons decayed, nucleosynthesis began.

Today we know that the abundance of ^{4}He as compared to hydrogen in stellar atmospheres is in the range of $0.2 \leqslant Y \leqslant 0.3$ in mass units (see e.g., Caloi & D'Antona 2007; Tremblay & Bergeron 2008). Even in the 1940's it was known, that the He/H ratio was much higher (Unsöld 1944; Schwarzschild 1946) than hydrogen burning in stars can account for (simple calculations show that $Y \simeq 0.05$, Bartelmann 2010). Thus, the observed abundance of ^{4}He is unlikely produced in stars and we need to consider that ^{4}He was in place already before stars have been formed. In the 1940's nuclear physicists began to work out how nuclear fusion may have proceeded in the early universe. Gamow (1946) gave the important note that in the Big Bang model "the conditions necessary for rapid nuclear reactions were existing only for a very short time ($\sim 10^2$s), so that it may be quite dangerous to speak about an equilibrium state" like the process of hydrogen burning in stars. The important step in ^{4}He fusion is the fusion of deuterium because it is more efficiently able to fuse to ^{4}He than pure hydrogen.

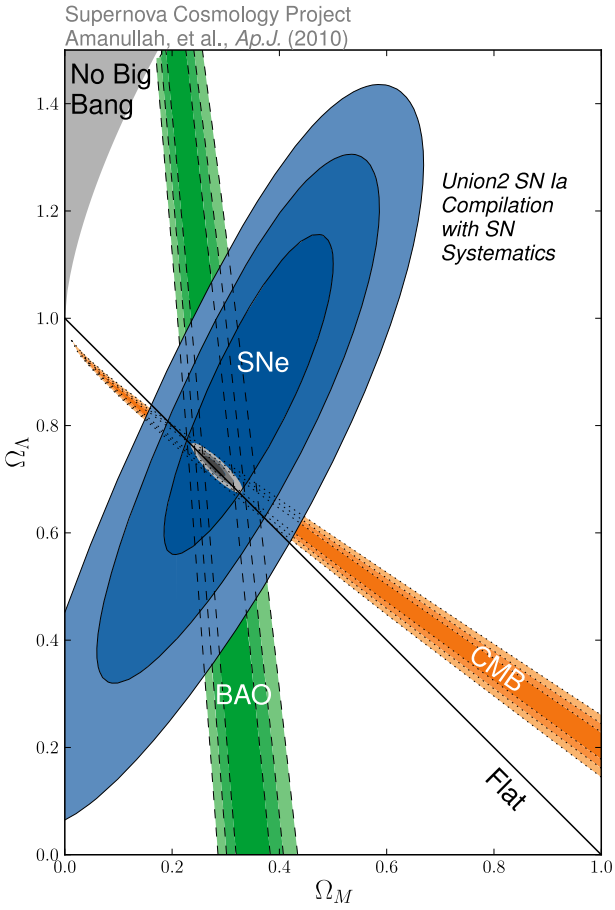

Figure 1: Parameter space for cosmological FLRW models in which the current radiation density is negligible. The solutions are parametrized by the current matter density Ω_M and vacuum/dark energy density Ω_Λ, both relative to the critical density. A flat universe as expected from inflation corresponds to $\Omega_M + \Omega_\Lambda = 1$. Shaded regions belong to 1σ, 2σ and 3σ confidence regions and are constrained by independent measurements of the CMB fluctuations (CMB), baryon acoustic oscillation (BAO) and the Supernova Cosmology Project (SNe), respectively. The measurements indicate that we are living in a flat universe dominated by dark energy, i.e., the expansion of the Universe is accelerating. Figure taken from Amanullah & the Supernova Cosmology Project (2010), their Fig. 10.

Alpher *et al.* (1953) reason the early period of the standard model of nucleosynthesis. By that time it was clear that no other stable nuclei with mass numbers between 5 and 8 exist (but traces of D, ^{3}He and ^{7}Li which are used to end up in ^{4}He, see Tytler *et al.* 2000; Beringer *et al.* 2012 for a review). The conditions needed for nucleosynthesis (temperatures around 10^9K) were in place about 100s after the Big Bang. While the Universe expands, its temperature drops, being unable to produce heavier stable elements so that after 100s more the Universe was too cold and nucleosynthesis was essentially completed. Thus, cosmological nucleosynthesis can only generate light elements (H, D, ^{3}He and ^{4}He) and heavier elements are the result of further processing in stars. Beringer *et al.* (2012) estimates a ^{4}He mass abundance of $Y \simeq 0.25$, i.e., the Big Bang model predicts that 25% of mass has been produced in primordial Helium, strongly in agreement with observations.

Based on temperature estimates at nucleosynthesis, Gamow (1948) showed that the energy budget in the early universe must have been dominated by radiation. He introduced the concept to put the radiation to the epoch when matter and radiation energy densities had the same amplitude – about 60.000 years after the Big Bang. At this time, matter was still fully ionized

($T \simeq 3.000K$) and the plasma was locked to the photons by Thomson scattering. As the Universe continues to expand, ~ 400.000 years after the Big Bang electrons and protons combined to form neutral atomic hydrogen. After this *recombination*, photons could move relative to the baryonic matter so that the Universe became transparent and the photons kept their properties from their last scattering – a black body spectrum.

Based on temperature estimations from nucleosythesis, Alpher & Herman (1948) predicted a radiation corresponding to a present time temperature of the order of 5 K. It was an antenna "temperature excess" of 3.5 ± 1 K, accidentally found by Penzias & Wilson (1965), that Dicke *et al.* (1965) identified as the cosmic microwave background (CMB) radiation – a relic of the Big Bang. The COSMIC BACKGROUND EXPLORER (COBE) satellite (Mather *et al.* 1990) has shown that the CMB radiation occurs as an almost ideal black body radiation with a temperature of 2.725 K (Fixsen 2009). This is a strong evidence for the Big Bang theory since photons can be thermalized in less than a Hubble time (see below) only from a hot, dense initial state (Binney & Tremaine 2008).

In 1970, Peebles & Yu and Sunyaev & Zeldovich, independently, investigated density perturbations (see above) which lead to the formation of structure in the Universe, i.e., to formation of galaxies (see Sect. 1.2). They predicted that these perturbations should excite sound waves in the relativistic plasma which cause spatial fluctuations in the CMB radiation with an amplitude of the order of 10^{-4} which subsequently were not found. Already thirty years earlier Zwicky (1933) and Oort (1940) found by the analysis of velocity distributions in galaxy clusters and galaxies that most of the containing matter is non-luminous – Zwicky called it *dark matter*. Peebles (1982) came up with a solution of the seemingly non-existing CMB fluctuations if connecting it to the dark matter. Given that dark matter consists of "very massive, weakly interacting particles and that the primeval fluctuations were adiabatic[2]", the fluctuations in the CMB may be of an order of magnitude lower than originally predicted.

In simulations by Davis *et al.* (1985) it turned out that the cosmological structure formation can be only explained if the dark matter was cold already in the early universe, i.e., its thermal velocity was negligible as compared to the Hubble flow[3] (Blumenthal *et al.* 1984; Bond & Efstathiou 1984). Finally, COBE discovered the predicted CMB anisotropy at the expected amplitude (Smoot *et al.* 1992) and dark matter became "confirmed" part of our universe. Follow-up missions WMAP (Spergel *et al.* 2003; Hinshaw *et al.* 2013) and PLANCK (Planck Collaboration 2013) increased the spatial resolution of the temperature anisotropies significantly and put narrow constraints not only on the dark matter content of the Universe (see Hu & Dodelson 2002 for the effects of cosmological parameters on the CMB anisotropies).

There have been tremendous efforts to determine precisely the key cosmological parameters describing our universe using different approaches, like:

- type 1a supernovae luminosities and light curves at different distances (Riess *et al.* 1998; Perlmutter & Supernova Cosmology Project 1999; Suzuki *et al.* 2012),
- Cepheids and type 1a supernovae using the HUBBLE SPACE TELESCOPE (HST, Freedman *et al.* 2001; Riess *et al.* 2009),
- the anisotropies of the CMB by WILKINSON MICROWAVE ANISOTROPY PROBE (WMAP, see also Sec. 1.2, Spergel *et al.* 2003; Hinshaw *et al.* 2013) and PLANCK (Planck Collaboration 2013)

2 Also known as curvature perturbations because they induce inhomogeneities in the spatial curvature. Adiabatic perturbations correspond to fluctuations in the energy density of a system.

3 The Hubble flow is the motion of galaxies due to the expansion of the Universe.

- and the baryon acoustic oscillation (BAO), an imprint of the plasma sound waves on large scale galaxy structures (Eisenstein *et al.* 2005; Blake *et al.* 2011; Beutler *et al.* 2011; Anderson *et al.* 2012).

The expansion of the Universe can be expressed by the Hubble parameter which varies with time. Of cause, it can be taken as a constant at present time – commonly termed *Hubble constant* H_0 – and represents the proportionality of recession velocity and distance found by Lemaître (1927) and Hubble (1929) as mentioned above. Those measurements which focussed on the Hubble constant revealed values in the range $67.3 \leqslant H_0 \leqslant 74.2\,\mathrm{km\,s^{-1}\,Mpc^{-1}}$. The inverse of the Hubble constant has the dimension of time and is called *Hubble time*. Under the assumption of a uniform expansion, it would correspond to the age of the Universe. But as a consequence of the FLRW metric the expansion depends on the ratio of mass to dark energy. Since this ratio can vary with time, the Universe may either accelerate or decelerate and the age of the Universe needs to be corrected. Using a Hubble constant of $69.7\,\mathrm{km\,s^{-1}\,Mpc^{-1}}$, the Hubble time is $\simeq 14.0\,\mathrm{Gyr}$ which gives an age of the Universe as $t_0 \simeq 13.76\,\mathrm{Gyr}$ (Hinshaw *et al.* 2013). Hence, the expansion in past was almost uniform and the Hubble time can be used as proxy for the age of the Universe.

Two more points are worth mentioning regarding the cosmological measurements. First, the baryon content of the Universe makes up 4.6% whereas the dark matter comprises 23.6% (Hinshaw *et al.* 2013; Planck Collaboration 2013). Hence, the dominant matter component in the Universe interacts only gravitationally (and maybe through weak interaction). It is pointed out above (and in Sect. 1.2) that it has to be "cold", therefore it is dubbed *cold dark matter*. Second, since measurements of the cosmological parameters are determined independently, they constrain the model of the Universe using FLRW metric without any assumptions. The anisotropies of the CMB as well as the BAO and the Supernova measurements in union yield a universe with almost perfectly flat geometry that requires a significant amount of dark energy at present time ($\sim$ 71.8%, Hinshaw *et al.* 2013; Planck Collaboration 2013). That means, the expansion is accelerating or in other words, the Universe has entered a second phase of inflation (see Fig.1).

Summarizing, the inflationary Big Bang theory is strongly supported by observations but it needs an invisible matter component (CDM) and an unknown (dark) energy component – corresponding to Einstein's cosmological constant Λ. This thesis is based on the ideas of this ΛCDM universe and in particular use measurements of its cosmological parameters.

1.2 STRUCTURE FORMATION

The primary process for formation of large-scale structures in the Universe is gravitational instability. But the detailed growth depends on the nature of the initial fluctuation. Jeans (1902) discovered that gas pressure prevents gravitational collapse on small spatial scales and can cause acoustic oscillations in the mass density as pressure and gravitation balance. On large scales gravitation dominates and mass density inhomogeneities grow exponentially with time. The growth of structure by gravitational instability is accurately described by linear perturbation theory but the growth of small density and velocity perturbations must take into account expansion. Lifshitz (1946) put structure formation on a relativistic perturbation foundation as he worked out how density perturbations grow outside the horizon (during inflation). In luminous galaxies the density is many orders of magnitudes larger than the critical density. Galaxy formation therefore needs highly non-linear density fluctuations. Zel'dovich (1970) gave an approximate solution for the growth of large density perturbations. Although his approximation

breaks down as the non-linear evolution proceeds, it allows the computation of gravitationally collapsing matter and arrives at the conclusion that the collapse must be anisotropic. This leads to disk-like structures which will appear as filaments and sheets (Doroshkevich 1970; see below). Moreover, it provides an explanation for the origin of the angular momentum of cosmic structures. The whole formalism of non-linear perturbation and its application to cosmology is reviewed by Bernardeau *et al.* (2002).

When radiation decouples from matter during recombination, the Jeans analysis of a gas mix of hydrogen an helium at a temperature of $T \simeq 4000\mathrm{K}$ shows that baryonic clouds with masses larger than $10^6\,M_\odot$ (solar masses) collapse gravitationally (Doroshkevich *et al.* 1967; Peebles & Dicke 1968), i.e., stars with masses we see today should not be formed from these clouds. Silk (1968) showed that the photon-baryon fluid becomes less perfect during the expansion. While photons are still coupled to the baryons the mean free path increases. Viscosity and conductivity are large, leading to a damping of fluctuations smaller than the horizon. This Silk damping essentially eliminates all fluctuations on scales smaller than $10\,\mathrm{Mpc}$ or $10^{14}\,M_\odot$, respectively. Hence, galaxy sized perturbations are washed out.

As pointed out in the previous section, dark matter (DM) is the key to explain the fluctuations in the CMB radiation, i.e., for galaxy formation (Peebles & Yu 1970; Peebles 1982). DM particles are considered to be collisionless and not interacting electromagnetically (as well as strongly) so that photon pressure does not affect them. The motion of relativistic DM particles will wash out any perturbation because the particles can freely propagate from overdense to underdense regions (free streaming). Once the particles cool down, i.e., they have non-relativistic thermal velocity, free streaming is not important anymore and the particles can clump (Blumenthal *et al.* 1984). According to the epoch when DM particle become non-relativistic, DM is called cold (very early), warm (early) or hot (late)[4]. Basically, the more massive the DM particle is, the earlier it will cool down and become non-relativistic. Free streaming is the reason, why the only known DM candidate, the neutrino, is not viable for DM because it is hot (Shandarin *et al.* 1983; White *et al.* 1984).

It has been shown by Davis *et al.* (1985) that cold DM is able to reproduce large scale structures of the Universe and can explain the CMB anisotropies the best. Such weakly interacting massive particles (WIMPs) that lack strong and electromagnetic interaction have not been discovered yet and are only predicted if the standard model of particle physics is extended[5]. Since small-scale fluctuations in the CDM are not subject to Silk damping, after recombination baryons can fall into potential wells already generated by CDM clumps. Baryon density fluctuations can then grow faster in those and the gas clouds will fragment (Hoyle 1953) and collapse gravitationally, igniting star formation (Abel *et al.* 2002). During the collapse, gas dissipates energy, which along with angular momentum conversation leads to the formation of protogalaxies containing disk structures as shown by Larson (1976) and Fall & Efstathiou (1980).

As outlined in Sect. 1.1, baryons have decoupled at redshift $z \simeq 1100$, 4×10^5 years after the big bang[6], and could form neutral hydrogen and helium (Spergel *et al.* 2003). Additionally, the photon pressure lowered and the atoms have fallen into the potential wells of the preexisting DM overdensities. Hydrogen and helium atoms will settle down and undergo violent relaxations as they can collide (see below). Therefore, they will be heated an get exited, resulting

4 The reference to "early" and "late" is given by the epoch and the corresponding radiation temperature when the largest galaxy-sized perturbations ($M \simeq 10^{13}\,M_\odot$) enter the horizon (Blumenthal *et al.* 1984).

5 There a many WIMP candidates with masses $\geqslant 1\mathrm{GeV}$ available in Supersymmetry. The thermal motion of such a particle would become non-relativistic at temperatures of $\sim 10^{13}\mathrm{K}$ corresponding to a cooling time of $10^{-6}\mathrm{s}$ after the Big Bang – long before recombination. See Jungman *et al.* (1996) for a review on supersymmetric WIMP candidates.

6 As pointed out in footnote 1, age of the Universe t (likewise the lookback time) and the spectroscopic redshift z of galaxies are cosmologically correlated as $t(z) \propto (1+z)^{2/3}$.

in emission of photons and free electrons. These electrons then can be used to form molecular hydrogen, radiating at lower temperatures. Thus, by radiation the atoms and molecules loose energy enabling them to cool. Due to that dissipational process baryons cool faster than the collisionless DM particles. This is probably the reason why we observe more baryonic mass than DM in the centers of galaxies (Cappellari *et al.* 2006). The gas will sink down to the bottom of the DM potential wells and condense into clouds which eventually collapse gravitationally so that stars can be formed. These first stars were not polluted by metals[7], but we do not know how they looked like and we do not know their typical mass.

However, the CMB provides evidence[8] for a great ionizing radiation at $z \simeq 10$ (Hinshaw *et al.* 2013). In the framework of the described picture, this suggests that during this period, 400 million years after the big bang, first stars must have ionized the surrounding gas. Since temperatures $\geqslant 10^4$ K are needed to ionize hydrogen (for helium it is even more), the first stars must have been very massive ($\sim 100\,M_\odot$, see Abel *et al.* 2002). With the growing number of those stars, the fraction of ionized gas increased and until $z \simeq 6$ the Universe was completely filled with ionized intergalactic medium[9] (Kashikawa *et al.* 2006). The whole process is called *reionization* because the Universe has entered a second epoch of ionization after decoupling (see Chap. 6 of Barkana & Loeb 2001 for a review of reionization).

Let us continue with the collapse of DM halos, which one can think of the "top hat" model of a sphere (Padmanabhan 1993). In a homogeneous universe the matter outside this sphere will not exert any forces on the particles within it. Basically, the larger the density within this sphere the faster the particles within it will collapse. In practice, density fluctuations are neither spherically symmetric nor isolated and as the sphere collapses the particles within it will undergo violent relaxation[10] and settle into virial equilibrium[11]. This configuration is called a *halo* and the whole process is often referred to as *virialization*. During the collapse the density of the halo inceases and its radius shrinks. The oldest halos have had the most time to collapse, being able to form the highest densities. That is indirectly seen in Fig. 2. Lacey & Cole (1993, see their Appendix A) calculate a lower limit for the radius within a galaxy cluster is in virial equilibrium – the *virial radius*. They estimate the density within this sphere with $\simeq 178$ times the critical density of the Universe (that is needed for a region to collapse). At larger radii, i.e., in regions with lower density, the sphere can not be relaxed and in virial equilibrium. In galaxy clusters, the region denser than 200 times the critical density often is considered to be in virial equilibrium. The virial radius then is labeled r_{200} or r_{vir} and the mass enclosed by that radius is called the *virial mass* (M_{200} or M_{vir}), often considered to be the cluster mass. However, even the relaxed core of a galaxy cluster will be disturbed if new galaxies fall in and join the cluster.

Critical to any theory of structure formation is the prediction of the abundance of halos, i.e., the number density of halos as a function of mass. From that prediction constraints can be drawn towards the abundance of galaxies in the Universe. A successful analytical model to gain understanding of the physics of structure growth was developed by Press & Schechter (1974). The so-called *Press-Schechter theory* is based on the ideas of density perturbations, linear

7 In astronomy, all elements heavier then He are termed metal, basically all elements which were formed in stars.

8 The CMB appears to be polarized. The degree of polarization depends on the probability that a CMB photon has been Thompson-scattered since recombination. From the degree of polarization the redshift of reionization can be estimated from the optical depth with respect to Thompson scattering (Haiman & Holder 2003).

9 This is known from the most distant galaxies, quasars, that show inhomogeneous distributions of neutral hydrogen and helium in their spectra.

10 Relaxation is produced by collective gravitational effects. As a result, Lynden-Bell (1967) showed that relaxation occurs "violently", i.e., the energy of a particle is changed significantly on very short time scales.

11 A state with, on average, balanced kinetic and potential energy. See e.g. Binney & Tremaine (2008) for a derivation of the virial theorem for a gravitational potential

gravitational growth, and spherical collapse. While this theory considers only one particular characteristic volume from which the halo distribution is calculated, Bond *et al.* (1991) extended this picture by including the effects of other volumes, i.e., they incorporated accretion and mergers. Basically, the outcome of the model is a mass function that grows exponentially on the low-mass side. Above a characteristic halo mass, the number density declines rapidly, i.e., for massive halos. The exact behavior of the low-mass end depends on the shape of the initial power spectrum of the perturbation. Based on these ideas, Schechter (1976) proposed an analytic approximation for the *luminosity function* (LF) of galaxies which has the same form, but it relates the luminosity of galaxies to the number density distribution. For a sufficient large volume, such as galaxy clusters, the *Schechter function* is a good representation of the LF as illustrated in Fig. 4b, and is generally in use (Croton *et al.* 2005; Faber *et al.* 2007). In particular, the logarithmic *faint-end slope* is of interest when observational studies are compared to each other as well as to simulations (Bell *et al.* 2003; Li & White 2009).

Gravitational N-Body simulations which follow the way that gravity enhances the small initial ripples in the ΛCDM universe show that small DM halos evolve from the initial DM fluctuations (Springel *et al.* 2005b; Boylan-Kolchin *et al.* 2009). Galaxies would be build from successive merger of smaller DM (sub)halos containing the first stars. This picture is called *bottom up* or *hierarchical scenario* because galaxies form early and then fall together to form clusters and larger structures (Searle & Zinn 1978). Massive galaxies are therefore built up of smaller fragments, i.e., their progenitors, or building blocks, can be considered dwarf galaxies (Read *et al.* 2006; see also Sect. 1.3). All these halos will evolve in a sense that they grow and merge with time to form the filamentary cosmic web that we observe today (see Fig. 2, but also Colless *et al.* 2001).

Based on the inhomogeinities of the CMB (from WMAP), Sánchez *et al.* (2006) calculated how DM particles must have been distributed at recombination and how the halos became denser while they accreted baryonic matter. They then compared the obtained matter power spectrum (based on ΛCDM cosmology) with the results of the spatial distribution of galaxies from the 2dF Galaxy Survey (Colless *et al.* 2001). They found that both power spectra agree in the region where they overlap, i.e., on these scales the distribution of luminous galaxies is identical with the expected DM halo distribution as indicated in Fig. 2. This strongly supports the above described picture of galaxy formation, based on ΛCDM.

Although the great success of the ΛCDM cosmology is to explain the homogeneous and isotropic CMB and its anisotropies connecting it with the distribution of galaxies as we observe it today, it suffers from some difficulties. On the one hand, there is the so called *missing satellite problem*. As computer capabilities increased and simulations were able to mimic less massive halos, it turned out that the simulations based CDM overpredict the abundance of faint satellite galaxies both in galaxy groups[12] and Milky Way sized systems by roughly an order of magnitude (Moore *et al.* 1999; Klypin *et al.* 1999). One possible explanation for this problem is the suppression of star formation in low mass halos by supernova feedback, yielding literally "dark" halos which we can not observe (Kauffmann *et al.* 1993, see Sect. 1.4). Moreover, different environmental effects may cause the lack of substructure as indicated by Simon & Geha (2007). Recent investigations show that the missing satellite problem can be solved if DM is warm, comprising of massive particles of $\sim 1\,keV$ (Smith & Markovic 2011; Lovell *et al.* 2012)

Another difficulty arises from cosmological N-Body simulations. Navarro *et al.* (1996) found that, regardless the applied cosmology and power spectrum, DM halos settle down to an universal mass density profile (NFW profile). It is a two-power law, i.e., a power law at both largest

12 The difference between a galaxy group and a galaxy cluster is basically defined by the number of members. While a group consists of some dozens to some hundred galaxies, a cluster of galaxies has some thousand members.

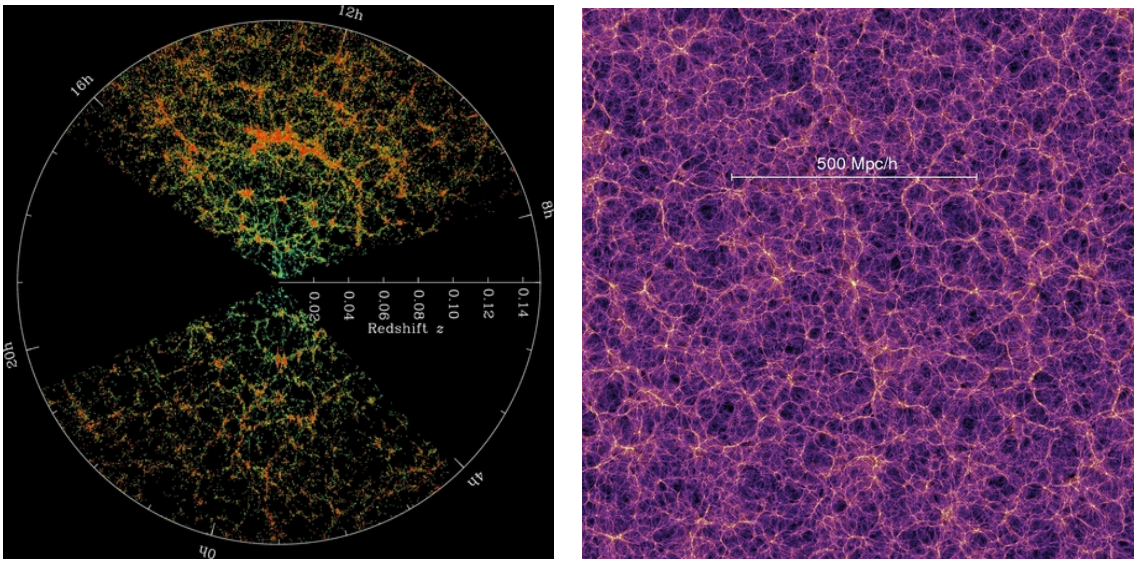

(a) Sloan Digital Sky Survey (Blanton 2008) (b) Millenium Simulation (Springel *et al.* 2005b)

Figure 2: (a) Galaxy distribution of the nearby universe as observed by SDSS. Galaxies are color-coded according to the age of their stars. The redder, more strongly clustered points show galaxies made of older stars. The outer circle is at a distance of $\sim 800\,\mathrm{Mpc}$, which is approximately the side length of the box in figure (b). The lower slice is thinner than the upper slice, so it contains fewer galaxies. (b) Dark matter density field at present time as calculated by the Millenium Simulation. Halos are color-coded by density and local dark matter velocity dispersion. The simulated universe is homogeneous and isotropic on large scale but on small scales structure becomes prominent. Due to its appearance these filaments (in interplay with the less dense voids) are called the cosmic web. The comparison of both images shows that the structures of the densest regions (filaments) in the simulations can be identified with the filaments of the oldest galaxies.

and smallest radii with a smooth transition. While the profiles are steep in the center, they are shallow near the virial radius. At smallest resolved radii, those central *cusps* have been found in both galaxies and galaxy clusters using different techniques (Hayashi *et al.* 2004; Sand *et al.* 2004). The conflict arises from the apparently non-existing cusp in low surface brightness and dwarf galaxies (McGaugh *et al.* 2003; Spekkens *et al.* 2005). Those *cored* halos may be also indicated by the non-detection of WIMP annihilation gamma-ray signals in 25 dwarf galaxies, provided a cuspy DM profile (Strigari *et al.* 2008b; Fermi-LAT Collaboration 2013). But the lack of annihilation signals can also indicate that WIMPS, i.e., CDM is not suitable for our universe. On the other side, Macciò *et al.* (2012) show that warm DM is not viable either. A possible solution to the problem is provided by other studies (Navarro *et al.* 2004; Merritt *et al.* 2005, 2006) which indicate that density profiles of DM halos have an approximate universal form that is better described by an Einasto (1965) profile. It is a single power law and has the same mathematical form as a model which is used to describe surface-brightness profiles of galaxies (Sérsic profile, see Sect. 1.3) but it is fitted to the space density, without any cusp. In either case, one has to keep in mind that both the NFW and the Einasto profiles generally try to fit a spherically symmetric model to the approximate triaxial ellipsoids of DM halos, and yield an accuracy of the order of 5% (Navarro *et al.* 2010). Both are thus good approximations for the density distribution in DM halos.

There is another point to mention regarding the DM profile in halos. In galaxies it is often assumed that their gas is in hydrostatic equilibrium[13]. This condition allows a direct determination of the galaxy's total mass because we know how much gravity is needed to prevent the

13 i.e., the systematic and turbulent hot gas velocities are subsonic

gas to escape (Mathews & Brighenti 2003). From the thermal X-ray spectrum of the hot gas temperature profiles can be gained in order to estimate the virial mass of the galaxy (stars and DM) using a NFW profile for the DM. Thus, it can be used to constrain the DM content of the galaxy (see e.g., Humphrey *et al.* 2006). The same technique can be applied to the brightest cluster galaxy (sitting in the center of a galaxy cluster) to measure the dark matter distribution of a whole galaxy cluster (Pointecouteau *et al.* 2005; Vikhlinin *et al.* 2006).

As computer technology advances, large N-Body simulations are able to produce DM structures in great detail (see Fig. 22; Springel *et al.* 2005b; Boylan-Kolchin *et al.* 2009; Klypin *et al.* 2011). They predict overdensities and underdensities, manifested as sheets, filaments and voids – observed large-scale structures[14] described by (Geller & Huchra 1989) and (Gott *et al.* 2005). However, all these simulations lack an important ingredient – baryons. They deal with DM only, because the calculations for billions of particles are time consuming, even when considering only one kind of interaction (gravitation). The physics of real galaxies is much more complicated. Here, so-called *semi-analytic models* (SAM) come into play, originally proposed by White & Frenk (1991). These incorporate, e.g., feedback from supernovae, gas cooling, star formation or the effects of galaxy mergers (see e.g., Kauffmann *et al.* 1993; Lacey & Cole 1993; Cole *et al.* 1994; Somerville & Primack 1999, but also Sect. 1.4). These processes are usually based on theoretical models but include observationally based assumptions, like the Tully-Fisher relation of spiral galaxies (see Sect. 1.3). That is, the model is tuned to fit observations in order to investigate how galaxies may have evolved. Today, these models are advanced and predict many properties of galaxies and galaxy clusters (see, e.g., Bower *et al.* 2006; de Lucia & Blaizot 2007; Guo *et al.* 2011). In particular, the galaxy catalogs of SAMs are a valuable tool to constrain the expected distribution of galaxies along the line of sight. However, these catalogs still have some short comings since certain properties of semi-analytic galaxies are not yet in perfect agreement with observations (Guo *et al.* 2011, 2013).

This thesis will make use of the concepts introduced in this section. In particular it will make use of the semi-analytic model by Guo *et al.* (2011) that is tuned to fit the low-redshift galaxy population and is based on the Millenium-II Simulation by Boylan-Kolchin *et al.* (2009). On of the goals is to figure out if the missing satellite problem still present (by means of the LF's faint-end slope), even though baryonic processes have been taken into account.

1.3 GALAXY CLASSIFICATION AND PROPERTIES

There is a variety of galaxies across the sky. The intuitive approach to classify those is to order them by morphology. Based on earlier studies, Hubble (1926) introduced a scheme that divided galaxies into diskless (ellipticals, E) and disk galaxies (spirals, S). While elliptical galaxies were subdivided according to their elongation/ellipticity (E1 through E7), spirals were differentiated by the size of the nuclear region, how tightly spiral arms are wound and the degree of condensation in the arms (Sa through Sc). Both types of galaxies merge into each other as ellipticals occur with ellipticities larger than 0.7 but without spiral structure. These galaxies usually exhibit a disk and are called lenticulars or S0. Within the spiral sequence, Hubble called the galaxies *early* through *late* regarding their structural complexity[15], but disregarding the "temporal connotation" of the adjectives. Although the connotation was originally meant to define

14 Even a filament of DM only was observed by weak gravitational lensing (Dietrich *et al.* 2012).

15 "This sequence of structural forms ... exhibits a smooth progression in nuclear luminosity, surface brightness, degree of flattening, major diameters, resolution, and complexity." (Hubble 1926)

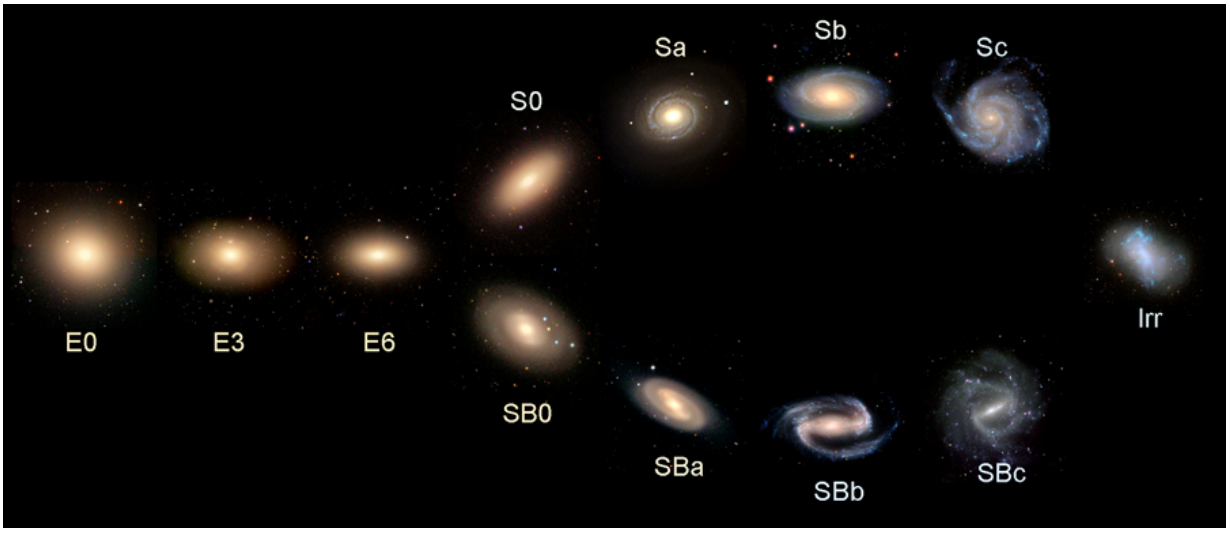

Figure 3: The Hubble Tuning Fork, a galaxy classification scheme by Hubble (1926). Spiral and elliptical galaxies merge in lenticular S0 galaxies. Since spiral galaxies can exhibit bars, they form two distinct branches. The diagram reads early-type (elliptical) galaxies through late-type (spiral) galaxies. Image taken from: http://hendrix2.uoregon.edu/~imamura/123/lecture-3/lecture-3.html

spiral galaxies, in the 1940's and 1950's astronomers began to term ellipticals as *early-type galaxies* and spirals were referred to as *late-type galaxies*, still being in use[16].

Furthermore, Hubble (1926) introduced the SB class for spiral galaxies exhibiting a bar and the irregular galaxy type (Irr) for galaxies which could not be assigned to E or S type. Hubble's classification scheme of nearby galaxies can be summarized in a diagram as illustrated in Fig. 3, usually referred to as the *Hubble Tuning Fork* or the *Hubble Sequence*. Commonly in literature, a galaxy is morphologically described by means of its *Hubble type*.

It was recognized later that Hubble's Sc class spans a wide range in the degree of resolution so that Shapley (1951) introduced another Sd class to account for the more irregular galaxies. de Vaucouleurs (1959) added the Sdm, Sm and Im type for very late-type systems that resemble the Magellanic clouds.

Almost all galaxy types listed by Hubble are of high intrinsic luminosity because they were chosen from a list of the apparently brightest galaxies on the sky. With the discovery of the fainter galaxies in the Local Group[17] (Shapley 1938) the enormous range of luminosity within the group of E galaxies was recognized so that the *dwarf elliptical* (dE) class[18,19] for the fainter ones was introduced by Baade (1944) when he found two other faint systems in the Local Group. In the context of their Virgo cluster study, Sandage & Binggeli (1984) tried to separate between dEs and Es by adopting a surface brightness rather than a total galaxy luminosity criterion. They described two new classes of dwarf galaxies. The dEs containing a disk feature are termed dS0, quite similar to E and S0 galaxies. Blue dwarf galaxies with very compact appearance were dubbed *blue compact dwarfs* (BCD). Additionally, dEs were now separated from dE,N through the existence of a nucleus – a central luminosity excess. As sensitivity

16 This thesis will use these expressions as they are defined here, including S0s to the early-types.

17 The Local Group is the galaxy group, the Milky Way is part of.

18 Kormendy *et al.* (2009) criticized that the name dwarf elliptical is confusing, because it implies that dEs are small scaled versions of giant E galaxies, which is maybe not the case. Therefore, they prefer the term *spheroidal*.

19 There is a range of galaxy brightnesses to divide between dwarf and giant galaxies. The total magnitudes reach from $M_B \simeq -18$ mag (Boselli *et al.* 2008) to $M_B \simeq -16$ mag (Ferguson & Binggeli 1994). The large range (almost an order of magnitude) in luminosity shows that the transition is smooth.

increased in the era of charge-coupled devices (CCD), new features have been revealed in dEs. Spiral arms were discovered as well as very faint disk signatures (Jerjen *et al.* 2000; Lisker *et al.* 2006). Late-type dwarf spirals, however, are generally not found but the link between *dwarf irregular* galaxies (dIrr) and spiral galaxies is discussed in Matthews & Gallagher (1997). Then, there are the diffuse *dwarf spheroidal* galaxies (dSph), structureless faint[20] dEs (Grebel 2001). In addition, new early-type dwarf galaxies have been discovered, like *tidal dwarfs*, *ultra-compact dwarf galaxies* and *ultra-faint dwarf galaxies* (Duc & Mirabel 1998; Hilker *et al.* 1999; Simon & Geha 2007).

In short, the zoo of dwarf galaxies is far from being homogeneous and its "taxonomy ... typically opens a Pandora's box" (Tolstoy *et al.* 2009, for a review). But giant galaxies are not free of confusion either. Kormendy & Bender (2012) link dwarf "spheroidals" to a whole sequence of S0 galaxies originally proposed by van den Bergh (1976). Moreover, Emsellem *et al.* (2007) ordered early-type galaxies by their kinematics rather than morphology, with slow rotators tending to be brighter and more massive galaxies. Not to mention, the complexity of late-type galaxies with their bunch of classification types. Generally spoken, the deeper the observations and the better its resolution the more different early-type systems became. It is beyond the scope of this thesis to address this topic. For simplification, we will stick to the scheme published by Sandage & Binggeli (1984) but summarize all late-type dwarf galaxies as dwarf irregulars (dIrr). In the following, properties of the main galaxy types in the nearby universe shall be discussed. Properties of dwarf galaxies are nicely summarized by Grebel (2001).

Elliptical galaxies. These smooth, featureless stellar systems cover several orders of magnitude in luminosity, including the brightest cD galaxies in the Universe, sitting in the center of galaxy clusters. These brightest cluster galaxies (BCGs) contain an elliptical core surrounded by a diffuse envelope on scales of hundreds of kpc. While BCGs have luminosities up to 100 times that of the Milky Way, normal, giant ellipticals are a few times more luminous. Ellipticals contain little or no cool interstellar gas or dust and little or no disk structure. The stars in most ellipticals are very old and have ages comparable to the age of the Universe (Thomas *et al.* 2005). Because there is no gas to generate new, young blue stars, those galaxies appear *red*, i.e., the major part of their light is emitted on longer optical wavelengths. Typically, ellipticals are overabundant in dense centers of galaxy clusters, but only few are found in the field[21].

In ellipticals, the isophotes – surfaces of constant surface-brightness – have an elliptical shape. While only the projection of a galaxy's brightness distribution is observed, indirect measurements strongly suggest that two types of shapes, triaxial and axissymmetric, exist (Binney 1978; Lisker *et al.* 2007). The brightness of E galaxies decreases smoothly with radius so that an edge is hardly to determine. In order to obtain a meaningful quantity for a galaxy's size, the effective radius R_e is defined as containing half of the galaxy's luminosity. In many galaxies, the isophotes vary with radius, but generally, a correlation between R_e and the luminosity is found (see Chap. ii). A powerful formula to describe the surface-brightness profile of elliptical galaxies is the Sérsic law (Sérsic 1963)

$$I(R) = I_e \exp\left\{-b_n\left[\left(\frac{R}{R_e}\right)^{1/n} - 1\right]\right\} \tag{1}$$

where $I(R)$ is the surface-intensity at radius R, I_e is the effective intensity at the effective radius R_e and n is the *Sérsic index*. This index describes the curvature of the profile, i.e., the concentra-

20 Grebel (2001) characterizes dSphs by $M_V \geqslant -14$ mag.

21 Commonly, astronomers refer to the field as low density regions in the Universe, in contrast to high density regions like galaxy clusters.

tion of light, and is correlated with the luminosity of the elliptical galaxy. While giant ellipticals are found to have $n \simeq 4$, defining the de Vaucouleurs or $R^{1/4}$ law (de Vaucouleurs 1948), dEs typically show Sérsic indices of between $n \simeq 1$ and $n \simeq 2$, and dSphs exhibit exponential profiles with $n \simeq 1$ or shallower (see e.g., Lieder *et al.* 2012). That is, from a relative point of view, giant ellipticals have much more light concentrated in the center than dEs, which in turn appear more diffuse. A detailed review of the Sérsic model is provided by Graham & Driver (2005).

It appears that E galaxies follow a number of relations. Faber & Jackson (1976) discovered first, that luminosity scales with velocity dispersion[22] of stars in E galaxies ($L \propto \sigma^4$). Later, it became clear that the Faber-Jackson relation is a projection of a thin plane – the *fundamental plane* –, spanned by three global observables: R_e, I_e and σ (Djorgovski & Davis 1987; Dressler *et al.* 1987). After Jorgensen *et al.* (1996) showed that the FP is not in agreement with the commonly assumed virial equilibrium (see Sect. 1.2), only one reasonable explanation remained, already realized by Faber & Jackson (1976). The ratio of mass and luminosity in E galaxies is not a constant, but varies with luminosity.

To measure the DM content of ellipticals is more complicated than in spiral galaxies since there is no ordered rotation of stars to infer from. Beside tracing their hot gas through X-Ray emission as pointed out in Sect. 1.2, a different approach has been successfully applied. Côté *et al.* (2003) used hundreds of globular clusters in the Virgo cluster to show that their radial velocities need a dark halo assuming the velocities to be random. Similarly, but based on stellar kinematics of nearby ellipticals, Cappellari *et al.* (2006) find evidence for dark matter, but its contribution to the mass inside R_e is $\leqslant 30\%$. Furthermore, their careful dynamical analysis show that the most luminous galaxies have (dynamical) *mass-to-light ratios* $M/L \sim 6$, while "normal" ellipticals show $M/L \sim 1$. On the other hand, the ultra-faint galaxies of the Milky Way have $M/L \geqslant 100$ (Strigari *et al.* 2007). That implies a minimum in M/L, commonly applied in simulations by means of the stellar-to-halo mass (e.g., Hopkins *et al.* 2013).

Spiral galaxies. This galaxy type, to which the Milky Way belongs, is composed of a disk and a bulge – a central bright extended spheroidal region of tightly packed stars. There are two types of bulges. A *classical bulge* looks like an elliptical galaxy, being red due to its composition of population II stars[23] and exhibiting a de Vaucouleurs profile. In *pseudobulges* or *disky bulges* star formation is still ongoing and they contain stars that orbit in an ordered fashion in a plane that is defined by the outer disk. However, the origin of bulges is not well understood (see Kormendy & Kennicutt 2004 for the formation of pseudobulges and Gadotti 2009 for a summary on bulges).

As already suggested by the name, the disks of these galaxies contains spiral arms, filaments of star forming regions dominated by O and B stars. Those young and luminous stars dominate the light of the galaxy, so that it appears *blue* in optical wavelengths. The disk has typically an exponential light profile and contains also a lot of dust which can extinct the light of the stars, in particular the short wavelengths. That is, such a galaxy, when observed edge-on can appear rather red as we will see in Sect. 4.2.2. Not only the dust, but also molecular gas and old stellar populations, dominating the mass of the disk, are arranged in the spiral pattern (Calzetti *et al.* 2005; Regan *et al.* 2001). The *bulge-to-disk ratio* in terms of luminosity is decreasing from Sa to

22 The velocity dispersion is the statistical dispersion of velocities about the mean velocity from a group of objects, such as a galaxy cluster.

23 Population II stars are metal poor. Thus, they are thought to have formed early, when only little metals were available.

Sd galaxies as well as their total luminosity does, whereas in Sds the knots of stars and HII regions are the brightest.

A bar – an elongated smooth structure composed of stars in the central region – is very common in spirals, about two thirds have one (Eskridge *et al.* 2000). Spiral (and irregular) galaxies are very abundant in the field (about 80%), but in dense regions their fraction drops to 10% (Dressler 1980), hinting to environmental influences on the evolution of spiral galaxies (see Sect. 1.4).

The rotation curves of spirals are easy to measure since the gas in the disk is a good tracers. One only has to account for the orientation of the galaxy and can utilize the Doppler effect. Like the Milky Way, spirals rotate considerably faster in their outer region than it is expected from Kepler's law and the light distribution. In fact, the dark matter density in spirals is derived from rotation curves (van Albada *et al.* 1985). The shape of the rotation curves in spiral galaxies is very similar to each other. In particular, in the outer regions they level out at a maximum velocity v_{max}, i.e., they become flat (Rubin *et al.* 1978). Similar to the Faber-Jackson relation in ellipticals, it exists a relation between a spiral's v_{max} and its luminosity: $L \propto v_{max}^{2.5}$ – called the *Tully-Fisher relation* (Tully & Fisher 1977). There is a significant scatter in the relation, partly due to the varying M/L ratio in spirals, resulting in different slopes quoted in literature. Derived (dynamical) M/L ratios are of the order of $1 \leqslant M/L \leqslant 10$ in the optical B-band (van Albada *et al.* 1985; Persic & Salucci 1988). The Tully-Fisher relation is the same for all spirals but it is a function of wavelength (Sakai *et al.* 2000).

Lenticular galaxies. The transition from ellipticals to spirals is smooth, so that S0 galaxies may be accidentally classified as Sa or E7 galaxy (Sandage & Bedke 1994). Like spirals, they exhibit a rotating disk and a bulge but their bulge-to-disk ratios are systematically larger than those of spirals (Dressler 1980). Like ellipticals, they lack spiral arms or extensive dust lanes. Cool gas and dust is only little abundant or absent. As a consequence of the missing gas, stars are not forming, qualifying those galaxies as early-type. Similar to ellipticals, lenticulars account for almost the half of all bright galaxies in the central regions of galaxy clusters but are very rare in the field or low density regions, respectively (Dressler 1980). Those correlations and the finding that the Tully-Fisher relation of S0s lies systematically below that of nearby spirals lead to the conclusion that S0s were "spiral galaxies that have faded since ceasing star formation" (Bedregal *et al.* 2006).

Irregular galaxies. These galaxies lack commonly any organized structure. Basically, they are the extension of the spiral sequence, becoming less luminous (e.g., Roberts 1969; Garnett 2002). The low-luminosity ones are the dIrrs. Like spirals, irregular galaxies are gas-rich. They contain a lot of dust and HII regions[24] with many star forming regions embedded (Hunter *et al.* 2006). In parts, they appear irregular because of dust extinction but also due to the young luminous stars that dominate the emission of Irrs so that they appear blue (see e.g., Lieder *et al.* 2012). It is possible that once the galaxies have used up or lost their gas reservoir, they transform into the red spheroidals (Kormendy & Bender 2012). Irregulars are very common in the local neighborhood ($\simeq$ 30%) but less present in galaxy clusters, in particular in their cores.

In the following chapters, we will make intensive use of the galaxy classification (and notation), introduced here.

24 In contrast to HI regions containing neutral hydrogen, HII regions are clouds of ionized hydrogen. They are typical sites for star formation. The radiation of the new born stars ionizes the surrounding gas.

1.4 GALAXY EVOLUTION AND ENVIRONMENTAL EFFECTS

As sketched in Sect. 1.2, after recombination gas clouds can grow and gravitational instabilities lead to the formation of disk-like protogalaxies. These galaxies will accrete gas from the surroundings due to its gravitational attraction. At high redshifts, the accretion will occur in so called *cold streams* along the filaments of the cosmic web of large-scale structure[25]. These gas flows are too dense to be shock-heated, in particular they cool faster than pressure can be developed to support a shock (Kereš *et al.* 2005; Dekel & Birnboim 2006). In cold streams stars form in clumps and merger of these clumps take place, which are essentially indistinguishable from minor mergers of gas-rich dwarfs (Dekel *et al.* 2009). However, the rotational disk configuration of a galaxy tends to be preserved while mergers of the clumps form a central spheroid. Unless, there is no other galaxy nearby, the galaxy will evolve through internal processes. When a molecular cloud has cooled down to less than 20 K, a starburst converts only a small fraction of it into stars and blows the remainder away into the *interstellar medium* (ISM). The process of blowing gas away is called *feedback*. Two types of feedback in the course of galaxy evolution are semi-analytically well studied.

Supernova feedback. Due to supernova explosions the ISM is heated up to 10^7 K. This enables gas to escape from low-mass galaxies, with speeds of some hundreds of km/s. These *galactic winds* of the first stars, have presumably led to the presence of low-surface brightness dwarf galaxies (Larson 1974; Dekel & Silk 1986). After the first star formation period until reionization, these galaxies were not able to retain their gas for subsequent star formation. This leads to the idea that if at reionization a galaxy has not had formed stars yet, it may "evolve" into a "dark-dark halo", because subsequent star formation is not possible (Dekel & Woo 2003). Moreover, (Governato *et al.* 2010) have shown that strong *outflows* from supernovae can inhibit formation of bulges, explaining the diffuse appearance of dwarf galaxies.

AGN feedback. An *active galactic nucleus* (AGN) is a compact region in the center of a galaxy that is much more luminous than normal centers of galaxies (possibly over the whole spectrum). The energy output of an AGN is believed to be driven by an accretion disk of a supermassive black hole[26] (Lynden-Bell 1969; Kormendy & Gebhardt 2001). In the nearby universe, AGNs are found to "reside almost exclusively in massive galaxies" (with stellar masses larger than $\sim 10^{10} M_\odot$) that resemble ordinary early-type galaxies (Kauffmann *et al.* 2003). These galaxies are massive enough to prevent the supernova-ejected gas from escaping so that it is trapped in the potential well of the galaxy. That has been proven by the detection of thermal X-ray emission of these hot gas spheres in early-type galaxies (e.g., Böhringer *et al.* 2000). The gas can dissipate by radiation, resulting in so-called *cooling flows* onto the center of the galaxy. The black hole at the center accretes the gas and a significant fraction of energy emerges as a collimated outflow. This outflow – called jet – heats the surrounding gas, counterbalancing the cooling flow (Omma *et al.* 2004). The remarkably similar X-ray morphologies of these systems hint that they have reached a kind of steady-state, not growing anymore (Donahue *et al.* 2006). Since the supermassive black hole in the center prevents the gas from falling onto the center, it effectively quenches star formation, making the galaxy red and passive. More interestingly, the galaxy can not create more luminosity, resulting in the exponential cut-off (see Fig. 4b) of the luminosity function at the bright end (White & Rees 1978; Benson *et al.* 2003; Springel *et al.*

25 Such a gas filament from the early universe has recently been observed for the first time (Cantalupo *et al.* 2014).

26 A supermassive black hole is at least as massive as $10^6 M_\odot$. Correlations of galaxy luminosity and velocity dispersion suggest that every massive galaxy harbors a supermassive black hole (Ferrarese & Merritt 2000; Häring & Rix 2004).

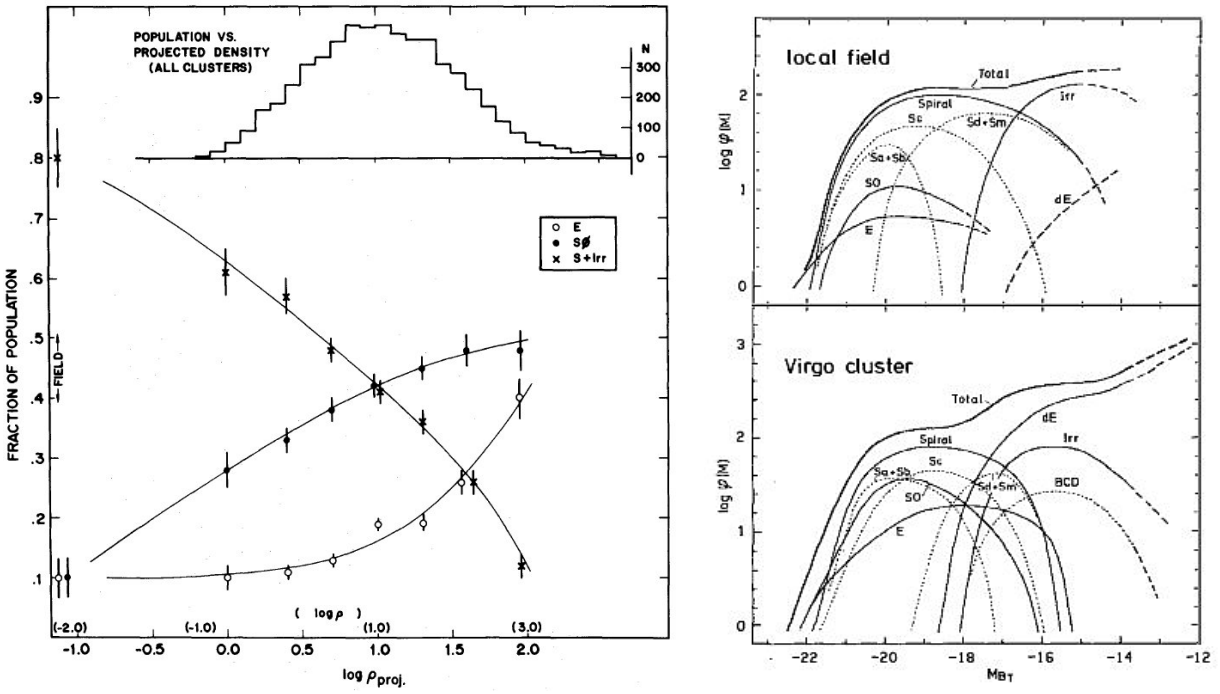

(a) Morphology-density relation, taken from Dressler (1980)

(b) Luminosity function in different environments, taken from Binggeli *et al.* (1988)

Figure 4: The morphology-density relation. (a) The fraction of galaxy-types vs. logarithmic projected density in Mpc^{-2}. In the densest regions of galaxy cluster, early-type galaxies (E, S0) dominate, while late-type galaxies (S+Irr) are the majority in the field (leftmost datapoints). (b) Another representation of the morphology-density relation by means of the luminosity function of field galaxies (top) and the Virgo cluster (bottom), the logarithmic number density $\log \varphi(M)$ (with arbitrary zeropoint) vs. total magnitude in B band (M_{B_T}). The classes dS0 and "dE or Im" are not illustrated but included in the total LF over all types. The luminosity function in the field is dominated by late-type galaxies while particularly at the faint end, the LF in the Virgo cluster is dominated by early-type galaxies. In both cases, there is an exponential cut-off at high luminosities as well as an exponential faint end. The faint-end slope in the underdense environment is shallower than in the dense environment of the cluster, i.e., there is no universal LF.

2005a; Sijacki *et al.* 2007).

As pointed out in the previous section, there are more early-type galaxies in dense regions while low-density regions are dominated by late-type galaxies (Dressler 1980), illustrated in Fig. 4a. This correlation is known as the *morphology-density relation* and suggests that external processes, triggered by the environment of a galaxy, also influence its evolution. Here, we shall introduce the main mechanisms that will have influence on this work.

Galaxy mergers (see Fig. 5, panels 4,5,10). In the context of a hierarchically emerging universe, interaction and mergers between galaxies are an essential process in galaxy formation and evolution. Stars which have been formed by such an event are unlikely to stay on circular obits, possibly forming a bulge. During a merger, the central black holes of the participants will be fed by surrounding gas that easily can fall onto the black hole, because the gravitational field is highly distorted. Thus, black hole growth is expected when galaxies merge (Hopkins *et al.* 2006).

In the early universe merger were more frequent due to the higher galaxy density. Today, galaxy-galaxy interactions become more likely in the environment of galaxy groups where gravitational attraction has a higher impact since galaxies move slowly relative to each other

(Zabludoff & Mulchaey 1998), in contrast to clusters where high internal velocities hinder galaxy encounters. There are many classification of galaxy mergers. *Major mergers* are interactions of galaxies of comparable mass, while *minor mergers* are classified as interactions between dwarf and giant galaxies. If one of the participating galaxies is a late-type galaxy, the merger is called *gas-rich* or *wet*. The gas in the disks of the galaxies will be violently shocked when two halos merge. In the overdensities of the shocking wave star formation will be ignited, i.e., the merger of gas-rich galaxies gives rise to produce a starburst that heats the galaxy (Kennicutt 1998). Also, aside from star formation, simulations show often disc components, well after the merger event (Springel & Hernquist 2005; Cox *et al.* 2006; Lotz *et al.* 2008; Hopkins *et al.* 2009). However, already in the 1970's the idea grew that red, elliptical galaxies can be produced by a merger of spiral galaxies (Toomre & Toomre 1972; Toomre 1977). But the properties of the remaining elliptical depend on mass ratio, morphological type, gas fractions and orbital parameters of the progenitors (Barnes 1988; Hernquist 1992). The brightest elliptical galaxies can only be formed from *dry mergers*, i.e., by galaxies with little or no gas (e.g, van Dokkum 2005; Bell *et al.* 2006; Hopkins *et al.* 2007). Minor mergers on the other hand, can form spheroids, merger-built (pseudo)bulges that could can evolve into the dEs we observe today (Kormendy & Kennicutt 2004; Naab *et al.* 2009)

Depending on the morphological criteria, resolution or projection, timescales for major mergers range from 0.1 Gyr to 1.9 Gyr for wet mergers, while morphological signatures of dry mergers disappear after 0.2 Gyr (Springel & Hernquist 2005; Bell *et al.* 2006; Lotz *et al.* 2008).

Another interesting finding is the imprint of galaxy mergers on the isophotes of the remnant. Hopkins *et al.* (2009) found in wet mergers the surface-brightness profile to be different from a de Vaucouleurs profile, with Sérsic indices of $n \sim 3$. Moreover, the deviation of the isophotes from perfect ellipses towards a disky structure (see Sect. 3.2) suggests that bright elliptical galaxies could have undergone wet a merger, even if no morphological merger signature remains visible (Khochfar & Burkert 2005; Cox *et al.* 2006; Kormendy *et al.* 2009). Boxy elliptical galaxies, in contrast, could be the remnants of dry mergers (Naab *et al.* 2006). Furthermore, Emsellem *et al.* (2007) found kinematically decoupled cores of kpc scale in bright elliptical galaxies. Additionally, Huang *et al.* (2013) find on the same scale subcomponents in the surface-brightness profiles of massive E galaxies. They argue in favor of the two-phase formation scenario (Oser *et al.* 2010). The inner component may be the outcome of the initial dissipational phase at high redshift (first galaxies formed by cold streams), while the outer component is added by material of dry minor mergers during the second dissipationless phase. But they admit, major mergers do not fit in this picture. Oser *et al.* (2012) additionally find that the properties of early-type galaxies are predominantly determined by frequent minor mergers because they are more likely compared to major mergers.

In the core of galaxy clusters, where galaxies have typical velocities of $\sim 2000\,\mathrm{km/s}$, galaxy mergers are unlikely to occur because the interactions are too fast for *dynamical friction*[27] and the collision will the participants not slow down enough (Binney & Tremaine 2008). Hence, encounters will have a stronger effect in the environment of galaxy groups with lower speeds. That gives rise that the cluster galaxies in the center of clusters have been "preprocessed" by mergers in groups that eventually merge to form clusters (Dubinski 1998).

In summary, galaxy mergers produce very likely elliptical galaxies. In the course of the cosmological evolution, in the current epoch, mergers will occur in dense environments like galaxy groups (and clusters), contributing an important piece to the morphology-density relation.

27 Kinetic energy of the motion of the galaxies is transferred to the motion of stars within the galaxies. This leads to a deceleration of the galaxies. The whole process is called dynamical friction and was proposed in a series of papers by Chandrasekhar (1943).

Tidal stripping and galaxy harassment (see Fig. 5, panels 6,7,9,11,12). If the encountering galaxies contain gas, it will compressed by the tidal forces, triggering star formation. Since the galaxies move with different velocities as compared to the colliding gas, these star forming regions are manifested by blue *tidal tails* (e.g., Jarrett *et al.* 2006). That material can rearrange itself and form so-called *tidal dwarf galaxies* (Duc *et al.* 2000).

Spiral galaxies in clusters will pass by many other galaxies and experience only weak encounters which will not produce tidal tails (in the above described fashion), but they are not unaffected either. As mentioned above, if the encounter between two galaxies is too fast, dynamical friction is not working properly. Crossing times are of some tens Myrs only, so that the interaction can be treated by impulse approximation. That is, the encounter results in a change of velocities of stars only, rather than a redistribution Binney & Tremaine (2008). Many of those encounters will alter the shape of the galaxy and eventually strip off the outer part the galaxy[28]. This process is called *galaxy harassment*, and due to the tidal truncation it can transform spiral and disky galaxies into dEs and dSphs, as shown by Moore *et al.* (1996, 1998). This scenario in combination with merging processes may lead to the domination of elliptical galaxies in cluster centers – explaining the morphology-density relation. Moreover, the model predicts an abundance of floating stars in the centers of galaxy clusters, unattached to any galaxy. Deep observations of the Virgo cluster find "tidal streamers" and diffuse light around the massive elliptical galaxies, confirming the harassment picture (Mihos *et al.* 2005; Ferrarese *et al.* 2012).

Ram-pressure stripping (see Fig 5, panels 1-3). In a galaxy cluster, hot gas becomes more concentrated towards the center due to the lower potential well, typically observed in the X-Ray (e.g., Böhringer *et al.* 2000; Sanderson *et al.* 2003). As outlined before, the gas may origin in either supernova or AGN outflows, or has been released by the shocks of previous mergers. Typically, galaxies move through the cluster with velocities of $\sim$ 1000km/s, and the impact of this intergalactic gas produces ram pressure, sweeping away the (cold) galactic gas (Gunn & Gott 1972). In practice, the sweep will shock the galactic gas, which gives rise to star formation, so that supernova-driven winds and ram-pressure stripping go hand in hand (Gavazzi *et al.* 1995). If the galaxy is massive enough and the inclination angle between the disk of the galaxy and the orbital plane is favorable, the expelled gas can fall back onto the galaxy (Vollmer *et al.* 2001; Roediger & Hensler 2005). Ram-pressure stripping in the group and cluster environment can be relevant at large distances from the center. Bahé *et al.* (2013) show that the depletion of hot and cold gas begins at $5r_{vir}$, quenching star formation as the galaxy falls into the dense environment. Also the hot gas halo of (early-type) galaxies can be stripped sufficiently at that distance.

Based on their model, Gunn & Gott (1972) presumed, that ram-pressure stripping "expects no spiral in central region of clusters like Coma". Dressler (1980) argues in parts against ram-pressure stripping as a complete model for the morphology-density relation because most of the S0 – which might be stripped spirals – are found outside rich clusters even though they are more prevalent in rich clusters. On the other hand, simulations show, that this mechanism "naturally accounts for the morphology of S0 galaxies" (Quilis *et al.* 2000), yielding a complete gas loss of disk galaxies (Roediger & Hensler 2005). In addition, Lin & Faber (1983) make ram-pressure stripping the primarily responsible process to turn dwarf irregulars into passive dwarf spheroidals because they will become completely gas-stripped after only one crossing

28 Within the central regions of galaxy clusters ($\sim r_{vir}$), a galaxy's DM halos will be stripped first, though not completely. The formerly extended DM halo will be truncated and the DM particles are smoothly distributed within the cluster center. This enables the stripping of the baryonic component. Due to the many encounters, the kinetic energy of the stars is increased and they can become unbound. The morphology of the galaxies involved is asymmetric and disturbed.

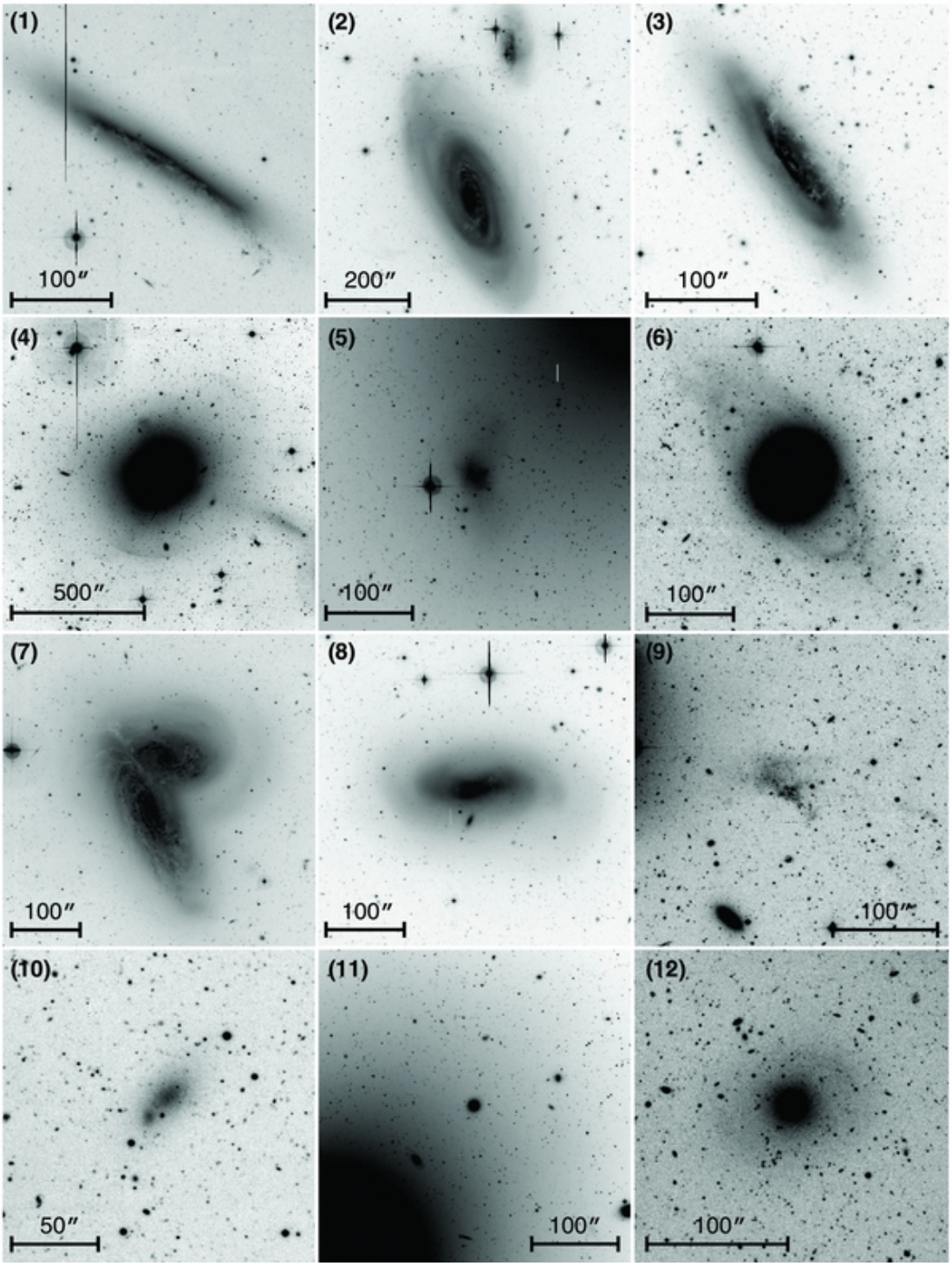

Figure 5: "Virgo cluster as a laboratory for studying the effects of interactions and environment on galaxy evolution. The different panels show likely examples of various evolutionary processes at work. (1)-(3) a ram-pressure-stripping sequence, illustrating gas stripping before, during and after its peak intensity (as inferred from HI observations). (4) a remnant of a gas-poor merger. (5) a gas-rich dwarf being accreted by M49 and an example of a "wet" accretion event. (6) an S0 galaxy with an extended star-forming ring, perhaps triggered by tidal interactions. (7) an interacting pair with tidally triggered star formation. (8) a possible post major merger Sa galaxy. (9) a candidate tidal dwarf system. (10) a possible binary dwarf system. (11) a close companion of M49 that has likely undergone severe tidal stripping. (12) a faint dwarf elliptical galaxy that shows faint spiral arms, possible evidence for the transformation by the tidal forces acting in the cluster environment. All images are in the g band; the scale is as shown in each panel (100" corresponds to ~ 8 kpc at the distance of the Virgo cluster)." Figure taken from: Ferrarese *et al.* (2012)

through the cluster (Mayer *et al.* 2006; Boselli *et al.* 2008). However, Weinmann *et al.* (2011) showed that ram-pressure stripping in the group environment is too strong for dwarf galaxies when comparing the Guo *et al.* (2011) SAM to observations. Similarly, a dynamical analysis of spiral galaxies in the Virgo cluster indicates that ram-pressure stripping is stronger when it is derived from the ICM density only (Vollmer 2009).

We have seen that many mechanisms exist to account for the morphology-density relation observed by Dressler (1980). There are intrinsic processes as well as external ones that influence the evolution of galaxies. Much progress has been achieved by incorporating those mechanisms in cosmological simulation to search for explanations of galaxy properties. The observational part of this thesis will make statements using arguments which are based on the findings sketched in this section. On the other side, the SAM we will make use of in the second part of this thesis incorporates not only those mechanisms presented here.

1.5 FOSSIL GROUPS

Section taken from Lieder et al. *(2013)*

The study of so-called *fossil groups* (FGs) began about two decades ago. Ponman *et al.* (1994) found the first of these systems: X-ray luminous galaxy groups characterized by their dominant bright central elliptical galaxy resulting in high mass-to-light ratios. The formal definition by Jones *et al.* (2003), generally adopted by the community, is the following:

1. Ensure that there is a dominant galaxy in the group by adopting an R-band magnitude gap Δm_{12} of at least two magnitudes between the two most luminous galaxies. They restrict that criterion to galaxies within half of the group's projected virial radius r_{vir} to ensure that L^* galaxies have had enough time to merge owing to dynamical friction, since the merging timescale within $0.5 r_{vir}$ for these systems is shorter than a Hubble time (Zabludoff & Mulchaey 1998).

2. Exclude "normal" elliptical galaxies that are not located in the center of the group by finding a hot gas halo that surrounds the galaxy (typical of central galaxies). This is achieved by a minimum X-ray luminosity of $L_{X,bol} = 10^{42} h_{50}^{-2}$ erg/s.

Ponman *et al.* (1994) interpreted their observations as witnessing the final stage in a group's evolution: an ancient stellar population in which most of the group's bright galaxies have merged into one luminous galaxy. They therefore termed their finding a "fossil" group. This evolutionary scenario seems a plausible one for isolated parts in our universe where galaxy groups can evolve undisturbed. Another FG formation scenario has been suggested by Mulchaey & Zabludoff (1999). Here, FGs could merely be "failed" groups in which the majority of the baryonic mass was accidentally placed in a single dark matter halo, leading to the dominant central object. Investigations of FGs do not favor this scenario since several studies have revealed that fossil brightest group galaxies (BGGs) exhibit disky isophotes (Khosroshahi *et al.* 2006). According to Bender (1988) and Khochfar & Burkert (2005), it is considered that gas-rich mergers cause this isophotal behavior. This is also supported by Aguerri *et al.* (2011) and Méndez-Abreu *et al.* (2012), who find that the Sérsic index of BGGs in FGs is significantly smaller than that in central galaxies of clusters. According to Hopkins *et al.* (2009), small Sérsic n stem from gas-rich mergers.

Investigations based on the criteria by Jones *et al.* (2003) have generally led to the conclusion that FGs formed early and have not experienced any major merger event for several Gyrs (Sanderson *et al.* 2003; Khosroshahi *et al.* 2004). According to simulations, they accreted the

majority of their mass at high redshifts (e.g., 50% at $z > 1$; D'Onghia *et al.* 2005; Dariush *et al.* 2007; Díaz-Giménez *et al.* 2008). Fossil groups would therefore constitute the top end of the hierarchical evolution of galaxies on group scales.

Some more recent studies suggest that FGs may only be a transient phase in a group's evolution (von Benda-Beckmann *et al.* 2008; Dariush *et al.* 2010; Cui *et al.* 2011). Dariush *et al.* (2010) argue that most of the early formed systems are not in a "fossil phase" at $z = 0$, but were so at some earlier point during their evolution. It is also clear that the observational criteria for FG classification are to some extent arbitrary, and slight changes to, say, Δm_{12} will change the fraction of environments classified as fossil. Milosavljević *et al.* (2006) show that there is a smooth distribution of the luminosity gap among 730 SDSS clusters, in line with the idea that the observational definition of a fossil group does not necessarily highlight a marked change in underlying formation histories. Nevertheless, it is clear that fossil groups mark an extreme environment (in the tail of a smooth distribution), which is only expected in a few percent of massive dark matter halos (Milosavljević *et al.* 2006).

Here we are interested in the properties of the faint galaxy population in such an extreme environment. Early results suggested that FGs also lacked faint satellites (Jones *et al.* 2000) that provide potentially interesting constraints on the so-called "substructure crisis/missing satellite problem" of ΛCDM (D'Onghia & Lake 2004). Recently, Mendes de Oliveira *et al.* (2009) has reanalyzed the FG used by D'Onghia & Lake (2004) and found a steeper faint end slope of -1.6 – comparable to clusters (e.g., Coma cluster: $\alpha = -1.4$, Secker *et al.* 1997). Other recent studies of FGs reveal shallower faint end slopes of $\alpha = -1.2$ when determined out to $\sim r_{vir}$ (Cypriano *et al.* 2006; Proctor *et al.* 2011; Eigenthaler & Zeilinger 2012), whereas the restriction to $0.5r_{vir}$ even reveals declining faint ends, i.e., $\alpha > -1.0$ (Mendes de Oliveira *et al.* 2006; Aguerri *et al.* 2011; Proctor *et al.* 2011).

However, none of these studies reaches magnitudes fainter than $M_R \simeq -17$ mag[29], barely scratching the dwarf regime. Therefore they cannot provide meaningful constraints on the asymptotic faint end slope of the galaxy luminosity function. To investigate this faint galaxy population of an FG, we provide here a photometric analysis of the NGC 6482 group down to $M_R \simeq -10.5$ mag – to our knowledge the deepest FG study yet.

1.6 THESIS OUTLINE

This thesis can be divided into to parts. The first part is observational, where we will study the properties of NGC 6482, in particular its satellite system. In the second part, for FG candidates is searched in the SAM of Guo *et al.* (2011) in order to study their properties and histories. The goal of this thesis is to test the hypothesis that a FG is an early formed galaxy group which has evolved without interactions of other groups, i.e., fossil groups are indeed exceptional. We also compare properties of NGC 6482 with the SAM FGs in order to draw conclusions on this FG and FGs in general in a final chapter.

29 Deeper observations of FGs exist with the HST ACS, but their much more constrained spatial coverage makes them inappropriate for the study of widely distributed dwarf galaxies.

Part II

OBSERVATIONS

2

DATA

2.1 NGC 6482

Chapter taken from Lieder et al. *(2013)*

NGC 6482 is the nearest known FG ($z = 0.0131$; Smith *et al.* 2000), so it is well suited for a ground-based study of its dwarf galaxy population. If adopting the cosmological parameters $H_0 = 70.0\ \mathrm{km\,s^{-1}\,Mpc^{-1}}$, $\Omega_M = 0.3$, and $\Omega_\Lambda = 0.7$, NGC 6482's distance is $m - M = 33.7$ mag ($d = 55.7$ Mpc), resulting in a physical scale of $0.263\ \mathrm{kpc\,arcsec^{-1}}$. We use these numbers throughout the paper.

We anticipate here that we measure $M_R = -22.7$ mag for the BGG and for the second ranked galaxy $M_R = -20.5$ mag. Together with the X-ray luminosity of $L_X = 1.0 \cdot 10^{42}\ h_{70}^{-2}\ \mathrm{erg\,s^{-1}}$ (Böhringer *et al.* 2000) NGC 6482 meets the fossil definition by Jones *et al.* (2003). Chandra observations imply a virial radius of 310 kpc, a hot gas mass fraction of $f_{gas} = 0.16$, and a total mass of $M_{200} \approx 4 \times 10^{12} M_\odot$, with an R-band mass-to-light ratio at r_{vir} of $71 \pm 15\ M_\odot/L_\odot$ (Khosroshahi *et al.* 2004). These data are consistent with the ROSAT study of Sanderson *et al.* (2003), but we note that their larger field-of-view constraints result in a slightly larger r_{vir} and in $f_{gas} \approx 0.07$, which are more consistent with its $T_X \sim 0.6$ keV.

2.2 OBSERVATIONS

On 5 June 2008, R-band images of NGC 6482 were acquired using the Suprime-Cam wide field imaging instrument at the Subaru telescope (Table 1). The Suprime-Cam camera is a mosaic of ten 2k×4k CCDs with a pixel scale of 0.202 arcsec $\mathrm{pix^{-1}}$, and it covers an area of $34' \times 27'$ per field (Miyazaki *et al.* 2002). The field-of-view corresponds to a physical scale of 624 x 458 kpc at the distance of NGC 6482, reaching the virial radius at the field edges. Eighty-five percent of the area that is enclosed by r_{vir} is covered. After a chip replacement in July 2008, B-band images were obtained on 4 August 2008. Both observations were obtained in service mode under run ID S08B-150S (PI Hilker).

In either band, two short (R: 60s, B: 120s) and four long (R: 540s, B: 1020s) exposures were acquired, all centered on NGC 6482. The average seeing in the R-band was 0.6 arcsec FWHM and 1.0 arcsec in the B-band.

2.3 DATA REDUCTION

See Appendix A for a general description of data reduction.

Suprime-Cam's reduction pipeline SDFRED was used to carry out overscan correction and flatfielding. As mentioned above, the B-band data were taken after a chip replacement. For this data set, each of the ten individual CCDs had four separate readouts, hence four different

Table 1: R−band observation time line from 5 June 2008.

Image type	Exp. time	Airmass	HST	Note
Science	60 s	1.024	2:07	
Science	60 s	1.026	2:09	
Science	540 s	1.036	2:11	(a)
Science	540 s	1.048	2:21	
Science	540 s	1.062	2:31	
Science	540 s	1.079	2:47	
Standard	5 s	1.258	2:56	(b)
Standard	5 s	1.246	2:59	(b)
Standard	5 s	1.064	4:47	
Standard	5 s	1.064	4:48	
Standard	2 s	1.063	4:50	

Notes. HST: Hawaii Standard Time, (a): expected fluxscale deviates from THELI's applied fluxscale by ~ 28%, (b) large scatter in flux measurements of standard stars.

gains. Unfortunately, accurate individual gains were not provided with the data[1]. We adjusted the four gains within each CCD relative to each other such that sky brightness differences were less than 1% after the flatfielding step. This adjustment was determined with the long exposures for which gain variations dominate the relative count difference between the four stripes per chip. The relative gain corrections were then applied to all other B-band exposures (flats, standards, and short science exposures). The knowledge of the absolute gain value for the B-band data is not necessary because absolute photometric calibration was achieved with the standard star exposures, themselves corrected with the same relative gain as the science data.

The THELI image reduction pipeline (Erben *et al.* 2005) then was used for the remaining steps of data preprocessing. The astrometric calibration from the THELI reductions was based on cross-correlation with the PPMXL catalog of point sources using the scamp software. It also corrected for geometric distortions in the outermost parts of the Suprime-Cam fields. After the THELI photometry step, which is based on SExtractor (Bertin & Arnouts 1996) and which adjusts the brightness levels of all chips and all exposures to each other, background subtraction was carried out using THELI.

After the THELI processing, instrumental magnitudes were computed from observations of standard stars taken in all four nights of the observing run, and from the photometry calibrated on the Cousins B and R magnitude system of Landolt (1992).

The average 1σ noise per pixel for the 36-minute coadded image in R-band corresponds to a surface brightness of $\mu_R = 27.2\,\mathrm{mag/arcsec^2}$, and $\mu_B = 28.4\,\mathrm{mag/arcsec^2}$ for the 68-minute composite image in the B-band. We thus have similar surface brightness sensitivities in B and R, since typical early-type galaxy colors are around $B - R \leqslant 1.5\,\mathrm{mag}$.

1 *"For all data, S_GAIN[1-4] and GAIN values at FITS header have errors greater than* 10%. *Those values are only for reference and should not be used for data analysis."* (http://smoka.nao.ac.jp/help/help_SUPnewCCD.jsp)

2.4 CALIBRATION

The R-band and B-band data were observed on different nights. Each night, standard star fields were observed at two different points in time and for a range of different airmasses. At each airmass, two exposures per field were obtained. A significant extinction coefficient was found in the B-band, while for the R-band it was consistent with zero. Thus, the atmospheric extinction term in R-band is absorbed by the zero point (Table 2).

For the night of 5/6 June 2008 when R-band data were taken, there were unfortunately some transparency variations due to the presence of clouds (Table 1), which prompted us to take special care in the photometric calibration: the standard star exposures in the R-band around 03:00 Hawaii Standard Time (HST) showed huge sensitivity variations at an average zero point fainter than the mean of the other standard star exposures. We discarded these measurements and instead adopted the zero points measured two hours later around 05:00 HST, when conditions were stable. Fortunately, the R-band science images, taken two hours earlier, were obtained at almost exactly the same airmass, so that we do not introduce a luminosity offset when not considering the atmospheric extinction term. The observations of multiple standards throughout the night therefore allowed exclusion of those standard images with a notable drop in throughput. The used calibration parameters are displayed in Table 2. Systematic uncertainties due to photometric calibration arising from this table are given by $\sigma_R = 0.04\,\mathrm{mag}$ and $\sigma_B = 0.12\,\mathrm{mag}$ (uncertainties for Schlegel extinction are not provided).

We then proceeded to check for the presence of clouds in the R-band science data taken between 02:07 and 02:56 HST. In general, THELI compensates for varying atmospheric transmission during a sequence of images that are to be coadded. Relative flux offsets are determined and logged via the `fluxscale` parameter, from comparing the same sources in the individual images. All images are then normalized to the highest transmission within the stack of images. For a correct compensation of possible cloud effects, it is necessary to have at least one cloudless exposure in the stack of images that are coadded. THELI found that the first of the four long R-band exposures (540 s) taken at HST 02:11 was indeed affected by a significant flux drop ($\sim$ 28%) with respect to the other three long exposures. This was corrected by THELI in the final coadded image via the `fluxscale` parameter. We consider this correction as robust, since the other long exposures had relative fluxes consistent with each other at the 5% percent level.

The two short R-band exposures were taken immediately before the one long exposure that was apparently affected by reduced atmospheric transmission, between 02:07 and 02:11 HST. Among themselves, these short exposures (later used only for fitting the centers of the brightest galaxies) did not show any notable relative variation in the flux. However, given their fast cadence, this does not exclude that they were affected by clouds. To test for the presence of clouds, we ran SExtractor on both the short coadded image and the long coadded image, both normalized to 1s integration time. The ratio of object fluxes between those two images shows that the short exposures had a 24% lower sky transmission than the long exposures. When we used the short time exposures for our analysis – only for the three brightest galaxies in our sample – we corrected the R-band flux by that offset factor of 1.31 (=1/(1-0.24)). For consistency reasons, we applied the same procedure to the B-band data and found that the long time flux is $\sim$ 6% less than the short time flux. This difference is within the typical variation on a clear night, suggesting that no clouds were present during these observations. To be consistent with the treatment in the R-band, we corrected all B-band longtime fluxes upward by a factor of 1.06.

Table 2: Photometric calibration parameters.

Filter	R	B
ZP [mag]	27.37 ± 0.02	27.07 ± 0.06
κ [mag]	—	-0.124 ± 0.046
X	1.056 ± 0.018	2.006 ± 0.318
CT	-0.001 ± 0.019	0.147 ± 0.033
A [mag]	$0.22 \ldots 0.31$	$0.35 \ldots 0.50$

Notes. ZP: zero point; κ: atmospheric extinction coefficient; X: mean airmass of exposures contributing to a coadded image; CT: color term; A: Galactic extinction by Schlegel *et al.* (1998)

3

METHODS

In the following we describe how parameters are extracted from the imaging data in a reproducible way. We search automatically for low-surface brightness objects using the source extraction software `SExtractor`. The isophotal parameters of galaxies, in particular the boxiness, are determined via the `IRAF` tool `ellipse`.

3.1 SEXTRACTOR

Source Extractor – `SExtractor` – is a software that uses automated techniques to analyze astronomical images (Bertin & Arnouts 1996) in order to find objects they contain. This is done in five steps.

Background estimation. First, `SExtractor` runs through a grid that covers the whole frame and determines the local background, i.e., the background in each mesh. This is achieved by clipping the number counts histogram iteratively until it converges around its median at 3σ. In case of a crowded field, a clipped mode is chosen. The resulting background map is a bilinear interpolation between the meshes of the grid that have an area `BACK_SIZE`. "The choice of the mesh size is an important step. Too small, the background estimation is affected by the presence of objects and random noise. Too large, it can not reproduce the small scale variations of the background" (Bertin & Arnouts 1996). Before the interpolation is done, the background values can be smoothed using the median filter `BACK_FILTERSIZE`. Effectively, this smooths deviations in the background map that arise from bright or extended objects. The computed background can also be used to calculate magnitudes of objects. The `BACKPHOTO_TYPE` parameter sets how the background around an object is determined. `GLOBAL` means, that the background value is taken from the background map.

Detection by thresholding. `DETECT_THRESH` is the threshold applied to detect objects. In order to account for low-surface brightness objects at least a certain number of adjacent pixels, specified by `DETECT_MINAREA` must have values above the threshold. We will specify the detection threshold with respect to the RMS of local background within a mesh.

Deblending merged objects. The detection method mentioned above needs to separate neighbors that have been extracted as a single source. A typical example for the issue is a pair of galaxies whose projection puts them close to each other. Any extracted object is re-thresholded in exponentially spaced levels between `DETECT_THRESH` and the maximum count in the object. The number of those levels is specified by `DEBLEND_NTHRESH`. The so obtained light distribution within the object is stored in a tree structure. Every branch, i.e., when pixels above a threshold level are found, is considered a different object provided that (1) the number count in the branch is above a certain fraction of the total number count of the composite object, and (2) at least one other branch above the same level and above this fraction exists. The fraction of the

flux is specified by the contrast parameter `DEBLEND_MINCONT`. Fig. 6 tries to illustrate the method.

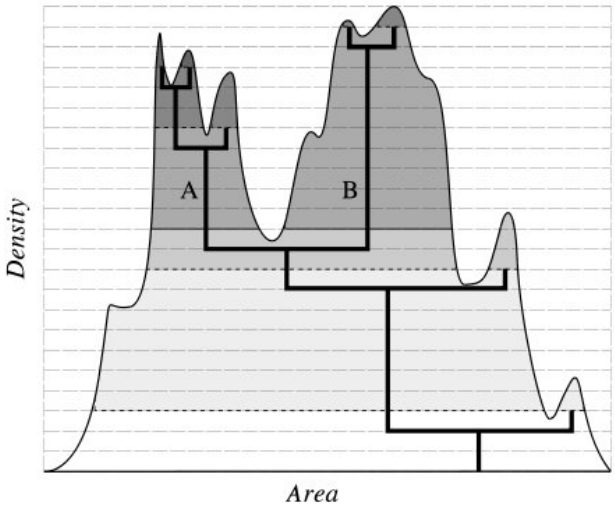

Figure 6: "A schematic diagram of the method used to deblend a composite object. The area profile of the object (smooth curve) can be described in a tree-structured way (thick lines). The decision to regard or not a branch as a distinct object is determined according to its relative integrated intensity (tinted area). In that case above, the original object shall split into two components A and B. Remaining pixels are assigned to their most credible "progenitors" afterwards." Figure taken from SExtractor manual, p21.

Filtering. This procedure checks if detections would have been made when their neighbors were not there. It calculates a Moffat light profile for the neighbor. Then the contribution from the wings of this profile is subtracted. Effectively, this procedure rejects spurious objects and was basically applied when `SExtractor` was used.

Photometry. The precise photometry of galaxies will be obtained by an isophotal analysis as demonstrated in the following section. However, for the detection of galaxies in the image data we will rely on their location in the surface brightness-luminosity diagram. It would not be reasonable to carry out the isophotal analysis for ~ 60000 objects contained in the field of view. We will use `SExtractor`'s photometry for a first guess. The peak surface brightness provided by `SExtractor` is given by the surface brightness of the pixels with the highest number count. Its flux is converted to surface brightness by the input of the pixel scale and the zero point (see Sect. 2.4). The total luminosity of an object is determined by the flux of all pixels the object is considered to be composed of, subtracted by the background estimated above and applying the zero point.

3.2 ELLIPSE FITTING

The light profiles of galaxies can be very complicated. They may consist of different structures like disk and bulge, light concentration might change as well as the position angle and ellipticity of isophotes. In order to measure the radial light profiles we use the `STSDAS isophote` package contained in `IRAF`. The main task is `ellipse` that fits a set of elliptical isophotes over an image in order to generate surface brightness profiles of the object which it contains. The algorithm uses an iterative method following Jedrzejewski (1987).

Each isophote is fitted along a predefined semi-major axis a, starting from an initial guess defined by center coordinates, ellipticity ϵ and position angle θ. The image is then sampled along an elliptical path, producing a 1-dimensional intensity distribution that depends only on the position angle. The intensity variations along the ellipse are fitted by a harmonic function

$$I(\theta) = I_0 + \sum_{n=1}^{4} \left(a_n \cos n\theta + b_n \sin n\theta \right). \tag{2}$$

Each of the harmonic amplitudes[1] $(a_1, b_1, ..., a_4, b_4)$ contains information about the deviation of the isophote from perfect ellipticity, i.e., the galaxy isophotes are not necessarily elliptical. Each amplitude of the series divided by the semi-major axis a and the intensity gradient of the light profile is then related to a specific ellipse geometric parameter.

$n = 1$: deviations with $360°$ period, i.e. "egg-shaped" distortions

$n = 2$: deviations with $180°$ period, i.e. "flattened" distortions

$n = 3$: deviations with $120°$ period, i.e. "triangular" distortions, not observed in galaxies

$n = 4$: deviations with $90°$ period, i.e. "boxy" distortions

The parameter a_4/a describes the *boxiness* of the isophotal shape, i.e., how boxy ($a_4 < 0$) or disky ($a_4 > 0$) an isophote appears (see Fig. 7). The sine coefficient b_4 corresponds to warped distortions. For pure boxy or pure disky isophotes, b_4 is close to 0. As mentioned in Sect. 1.4, this parameter is of particular interest since those fourth order deviations of isophotal shapes are signatures that are related to galaxy mergers (Bender 1988; Khochfar & Burkert 2005).

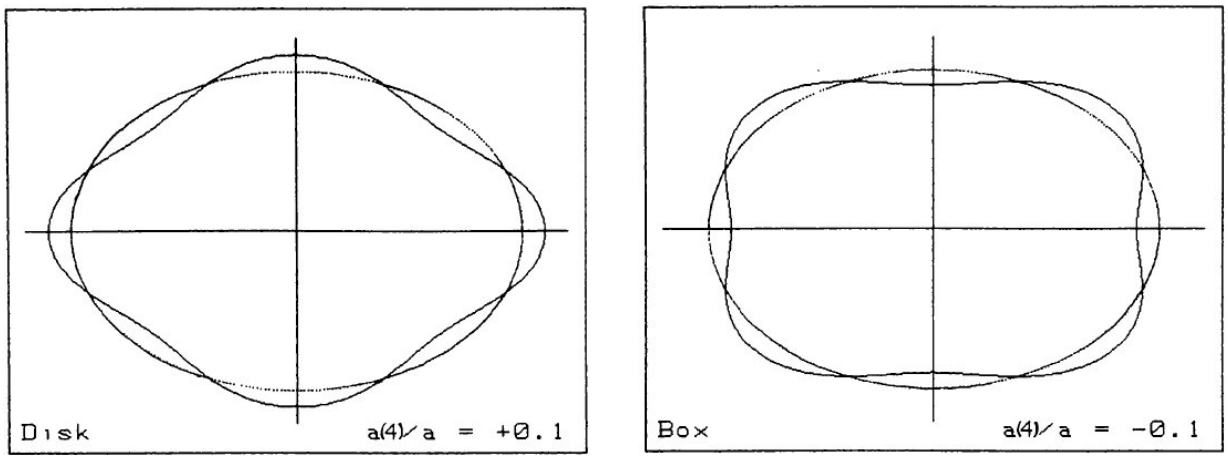

Figure 7: Illustration of isophotes with disky shape ($a_4/a = +0.1$, left panel) and boxy shape ($a_4/a = -0.1$, right panel) as compared to perfect ellipses. Figure taken from Bender *et al.* (1988).

`ellipse` offers to mask pixels that shall not be considered during the fitting process. The reason for the mask are obvious foreground stars or artifacts that distort the isophotes of the object of interest. For spatially small galaxies those masks were created manually using `ellipse`'s interaction mode. In the case of galaxies with spatially large extend with many small "companions", however, `SExtractor` was used.

There are many parameters to be set to fit the isophotes. The method applied to obtain the light profile is the following:

1. The initial fit was performed with variable ellipticity, position angle and position center of the measured light profile in order to get a first guess for those parameters. The starting point for the fit was basically near the effective radius of a galaxy.

2. After the first guess for the center coordinates, they were fixed at the position where the S/N was smallest and/or the position did not change significantly over a large range of the fit.

1 The `ellipse` task uses A_n coefficients of the sine and B_n of the cosine terms, in contrast to the general notation in literature we have used here.

3. Subsequently, the same method was applied to ellipticity and position angle. In some cases there was an isophote twist observed such that position angle was allowed to vary. Similarly, in some cases better results were obtained by applying variable ellipticity.

4. We checked the obtained isophotal fit with the `isopall` task in order to find a guess for the isophotal parameters. After that, a model of the light profile was created using the `bmodel` task and subtracted from the original image. The model was finally fine-tuned (by fixing model parameters with the best guesses) in order to get a residual image that contains the least signatures.

Basically, `ellipse` provides an output table that contains all parameters of an isophote as a function of the semi-major axis. These tables will be used to analyze the surface-brightness profiles (see Sect. 4.3), and also to derive accurate galaxy magnitudes from the cumulated intensity of the isophotes.

4

SAMPLE SELECTION AND PHOTOMETRIC PROCEDURES

Chapter taken from Lieder et al. *(2013)*

4.1 SEXTRACTOR AND MORPHOLOGICAL CLASSIFICATION

SExtractor (Bertin & Arnouts 1996) was used for detecting dwarf galaxy candidates in the field of view, followed by visual inspection. To optimize SExtractor's parameters, we simulated seeing convolved dwarf galaxies with exponential surface brightness (SB) profiles and circular morphology (ellipticity=0) and added them to the R-band Subaru field. We put only 50 artificial galaxies on randomly chosen fields of 1 arcmin^2 to not saturate the already crowded field with objects. That process was repeated 100 times. Later in this section, we also use these simulations for completeness determination.

Dwarf galaxies are found to be relatively homogeneous in terms of their photometric scaling relations (Misgeld & Hilker 2011) among different environments. As input for our simulations, we used the μ-mag relation found by Misgeld *et al.* (2009) for dwarfs in the Centaurus cluster[1] with a simulated scatter in μ of $\pm$ 0.96 mag around the fiducial relation. This scatter corresponds to the 2 σ width of the relation found by Misgeld *et al.* (2009). The goal of this exercise is to determine the location of typical dwarf galaxies in SExtractor's `MU_MAX-MAG_BEST` space, in order to establish a distinction from the crowd of small faint objects whose apparent sizes are close to the resolution limit of our data (Fig. 8). The parameter space occupied by the simulated dwarf galaxies is clearly offset from the bulk of faint sources, which allows defining a fiducial separation line as indicated in Fig. 8. All objects below the green line in that plot are considered as possible members of the NGC 6482 group. A small minority of simulated dwarf galaxies have recovered SExtractor parameters above that line, because they are superposed on another object – mostly a brighter foreground star.

1 $\mu_{V,0} = 0.57 \cdot M_V + 30.90$ and converted to R-band by adopting $V - R = 0.6$ mag

Table 3: Optimized SExtractor parameters for dwarf galaxy detection.

parameter	value
`DETECT_MINAREA`	16
`DETECT_THRESH`	2.0σ
`DEBLEND_NTHRESH`	16
`DEBLEND_MINCONT`	0.0001
`BACK_SIZE`	12
`BACK_FILTERSIZE`	11
`BACKPHOTO_TYPE`	GLOBAL

Notes. This parameter set is sensitive to faint extended objects but many more unresolved objects are found. Photometric output parameters are reliable in general, but individual outliers of up to 0.5 mag between input and recovered magnitude can occur due to the rather extreme setting of background determination.

Overall, the analysis of SExtractor's findings showed that even with extreme settings, only up to $80-85\%$ of the simulated galaxies for the brightest galaxy bin are discovered (see Fig. 9). This is due to a crowding completeness limit imposed by the high foreground star density towards NGC 6482 owing to its low galactic ($l = 48$, $b = 23$) latitude (see, e.g., Fig. 10). In the halo of bright stars, an automated detection algorithm like SExtractor tends to "overlook" individual sources. In addition to the crowding incompleteness, the usual surface-brightness incompleteness begins at $M_R \sim -13$ mag. We used an analytical expression to describe the surface brightness incompleteness, normalized to the crowding incompleteness level. This function is shown in Fig. 9. It reaches a 50% completeness at $M_R \approx -10.5$ mag and was used to correct the luminosity function (LF) for incompleteness.

The SExtractor detection parameters were varied (see Fig. 9 and Table 3) in order to find the optimal set in terms of recovered simulated galaxies with respect to all detections classified as galaxy – given in Fig. 8. We stress that for the actual photometry of dwarf galaxy candidates, individual aperture photometry was performed. The automatic magnitudes measurements by SExtractor are only used for the preselection of probable dwarf galaxy candidates.

The optimal SExtractor parameter set for dwarf galaxy detection is displayed in Table 3, and yielded a total of 621 galaxies below the green line, out of a total of 61120 detections in the field of view. Those 621 objects were a preselection and were subsequently inspected visually by two of the authors (SL and SM) in an independent manner in order to reject artifacts (see Fig. 11). The majority of sources were indeed readily identified artifacts in the halos of bright stars, see e.g., the lefthand panel of Fig. 11. Another goal of the visual inspection was to reject obvious background galaxies, such as low surface-brightness spiral galaxies, interacting low surface-brightness galaxies (merging events), or small, very faint galaxies that appear too compact (compare right center panel and right bottom panel of Fig. 10). In particular, the last distinction has an impact on the number counts at the faint end of our sample. It is well known that faint dwarf galaxies (at $M_R \geqslant -12$ mag) are diffuse, while their effective radius does not change

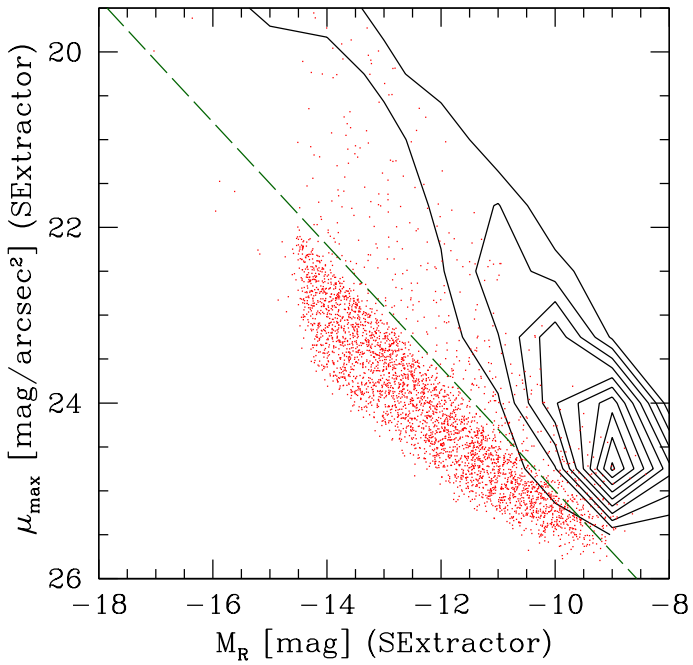

Figure 8: SExtractor `MAG_BEST` and peak surface brightness for all non-saturated objects detected in the long exposure of the Subaru NGC 6482 field of view, including simulated dwarf galaxies with apparent sizes corresponding to the distance of NGC 6482. The SExtractor object detection parameters are given in Table 3. Black contours: all detected objects. Red dots: discovered simulated dwarf galaxies. Green dashed line: separation line adopted between galaxies and unresolved objects at the faint end ($\mu_{peak} = 30 + 0.7 \times M_R$).

significantly with luminosity (see Misgeld & Hilker 2011). As a result, we implicitly assume for our visual inspection that the faint dwarf galaxies should exhibit such a diffuse appearance.

Of the 621 SExtractor detections, 83 remained as visually confirmed candidate dwarfs. Twelve other sources were rejected because either a spike of a nearby foreground star covered the object's center, a structure was visible after the subtraction of the modeled galaxy (see Sect. 4.2.1), or there was no counterpart found in B-band, or only a very weak one (~ 1σ above sky). Furthermore, two obvious dwarf galaxies (with $M_R \sim -11.5$ mag and -10.7 mag) not detected by SExtractor and all bright galaxies (six galaxies brighter than $M_R = -18$ mag and a diffuse dE with $M_R \sim -15.6$ mag) were included in the sample since SExtractor was tuned to find faint galaxies with $M_R > -14$ mag. Overall, 80 galaxies in the absolute magnitude range -8.8 mag to -22.7 mag at NGC 6482's distance were selected for detailed photometric analysis.

The morphological classification we adopted during visual inspection follows the extended Hubble scheme by Sandage & Binggeli (1984). In the dwarf regime, we simplify it by labeling early-type dwarf galaxies generally as "dE" and irregular dwarf galaxies as "dIrr". Examples of our classification are shown in Fig. 12. The morphological classification type of each group galaxy is provided in Table 6.

4.2 COLOR-MAGNITUDE DIAGRAM

The morphologically preselected sample was cleaned of further probable nonmembers via color selection criteria. In the following section 4.2.1, we describe the photometric procedures applied for the color measurement and in 4.2.2 discuss the selection of the fiducial sample based on the distribution in color-magnitude space.

4.2.1 *Photometric procedure for magnitude and colour measurement*

To correct for the light blurring due to the PSF, we degraded the R-band images to the worse seeing of the B-band images (1.0 arcseconds) using `IRAF` task `psfmatch`. By doing this, we expected to measure the flux within the same physical isophotes. Since the observed field is very

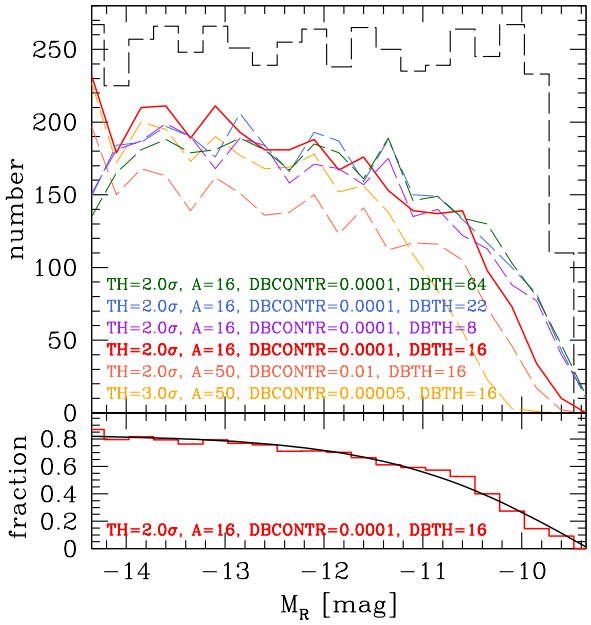

Figure 9: Determination of optimal SExtractor parameters. Upper panel: selection of tested SExtractor parameter sets. Colored curves show SExtractor detection number counts for different setups (`TH`: detection threshold; `A`: minimum area of pixels above threshold; `DBTH`: number of deblending subthreshold; `DBCONTR`: deblending contrast). The black, dashed histogram indicates the number of simulated galaxies in each magnitude bin. The red solid line represents our final choice, since it provides an optimal balance between the fraction of recovered objects and the detection of spurious ones. Lower panel: the red, solid histogram shows the fraction of recovered simulated galaxies using the optimal parameter set. The black solid line is a fit to the red histogram (i.e., our completeness function). Owing to crowding incompleteness (high foreground star density), the recovery completeness saturates at 80% for the brightest sources.

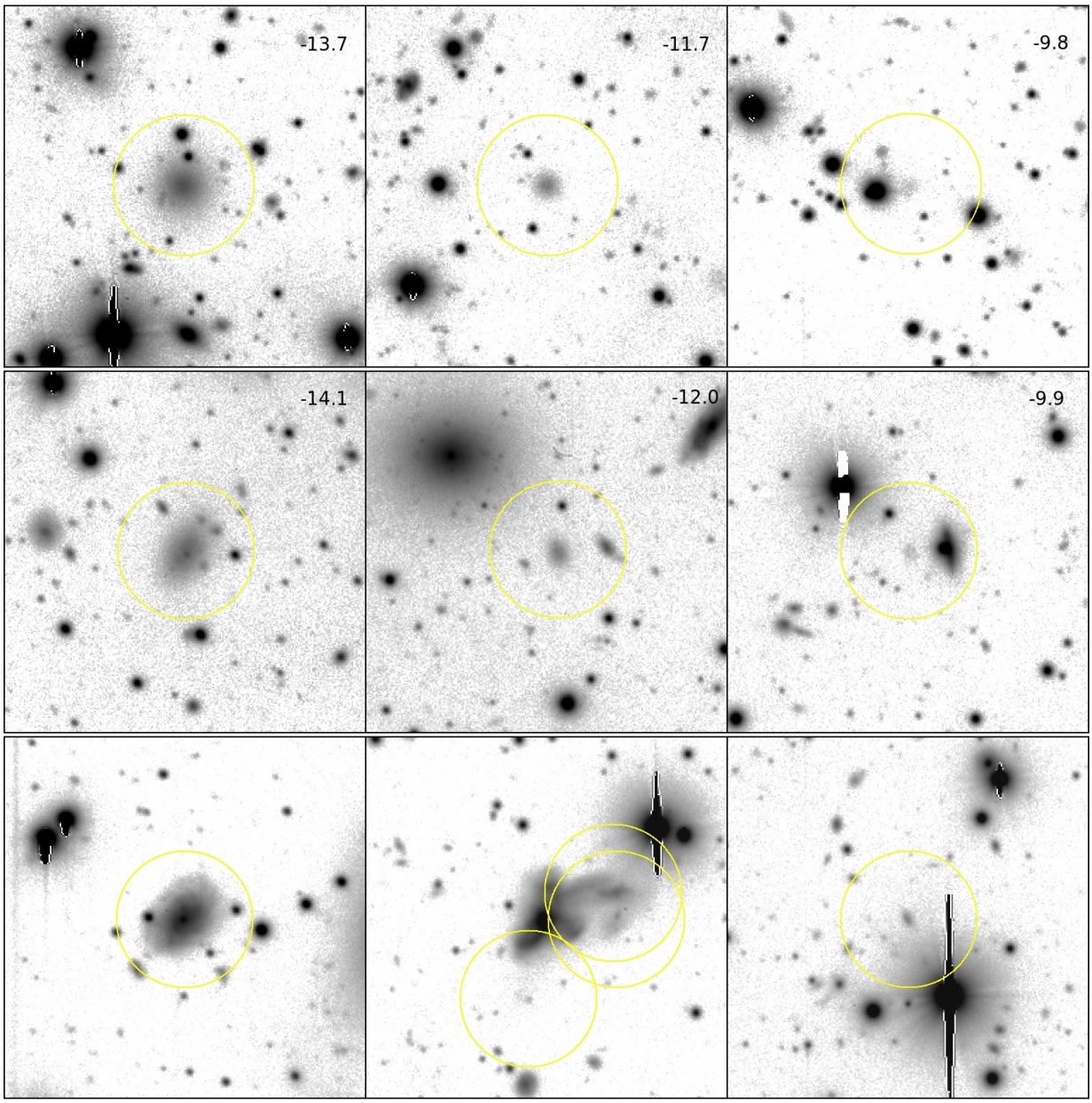

Figure 10: Illustration of example SExtractor detections. In each case the yellow circle has a diameter of 20 arcsec and is centered on the object in question. Numbers in the upper right corner denote absolute R-band magnitudes. Upper panel: simulated galaxies placed into deep science images. Middle panel: objects accepted as possible members after visual inspection. Lower panel: rejected objects because of compact appearance or visible structure typical of background grand-designed spirals or mergers.

crowded, the light of a very bright foreground star's reflection halo partially contaminates the light of a selected dwarf galaxy in many cases (see, e.g., left image of Fig. 11). In those cases the star was modeled in both passbands (using `ellipse`) and subtracted from the image in order to obtain more reliable values for the galaxy's luminosity. All galaxies were photometrically analyzed using the `ellipse` task (Jedrzejewski 1987) that is included in the `STSDAS` package of `IRAF`. All `ellipse` fits were performed with fixed parameters for center coordinates and position angle but variable ellipticity. In some cases, like the central galaxy NGC 6482 itself, optimal results were obtained when the position angle was allowed to vary. Because the seeing of the R-band images was better, we did a first `ellipse` run for the undegraded R-band images. Those

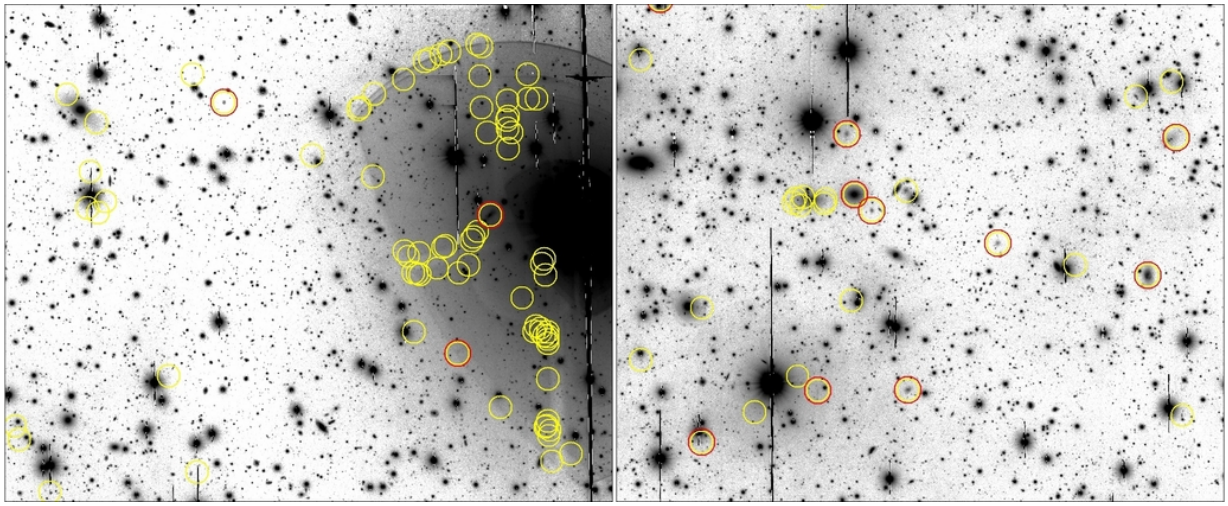

Figure 11: Illustration of preselected SExtractor detections considered as possible members (red circles) and artifacts/background sources (yellow circles). Left: many objects are rejected since they are detected in the refraction halo of a foreground star and in the shadows along instrument suspension. Right: a field not affected by artifacts where detections close to spikes of foreground stars were rejected. Only a few objects remain and are considered as possible group members (red circles).

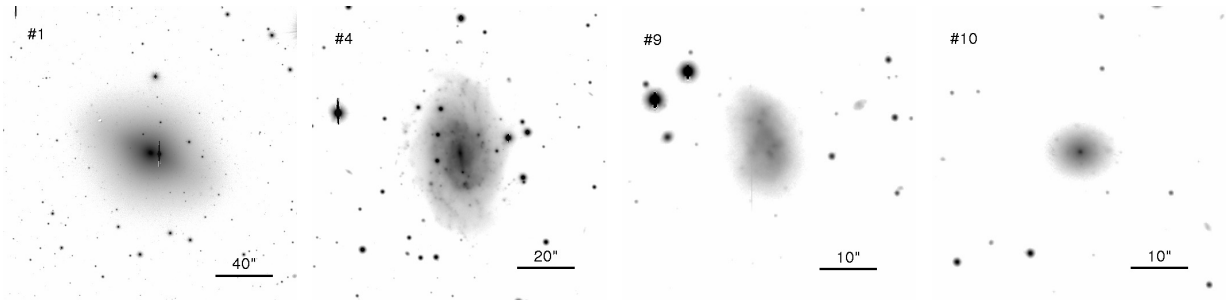

(a) E (b) SBc (c) dIrr (d) dE,N

Figure 12: Examples of morphological classification (provided in subcaption).

were used for the surface brightness analysis in Sect. 4.3. Another `ellipse` run was performed to fit the degraded R-band images. We then applied the obtained isophote table to the B-band image of the same object to measure the flux within the same physical isophotes. Obvious faint foreground stars and background galaxies were masked, and `ellipse` fits were performed far beyond the galaxy's edge to see whether the signal reaches the amplitude of the background noise. Using that level, an individual background adjustment was done for every galaxy. The result of this background estimation is shown in the three panels of Fig. 13. The intensity levels out at zero and associated error bars become as high as the signal; i.e., the signal is dominated by background noise (note the logarithmic scale of the intensity – right axis).

The `ellipse` output tables were used to determine all astronomical quantities that are presented in this study. The truncation radius of a galaxy was defined to be the last isophote at which the intensity is still higher than its error. The radial profiles of the cases shown in Fig. 13 are displayed out to that truncation radius. The flux enclosed by that ellipse is used as (measured) total flux f. Using that flux the apparent magnitude of an object is calculated. Finally, the apparent magnitude of an object was corrected for galactic extinction by applying the foreground extinction map of Schlegel *et al.* (1998). In Table 2 quantities determined for the

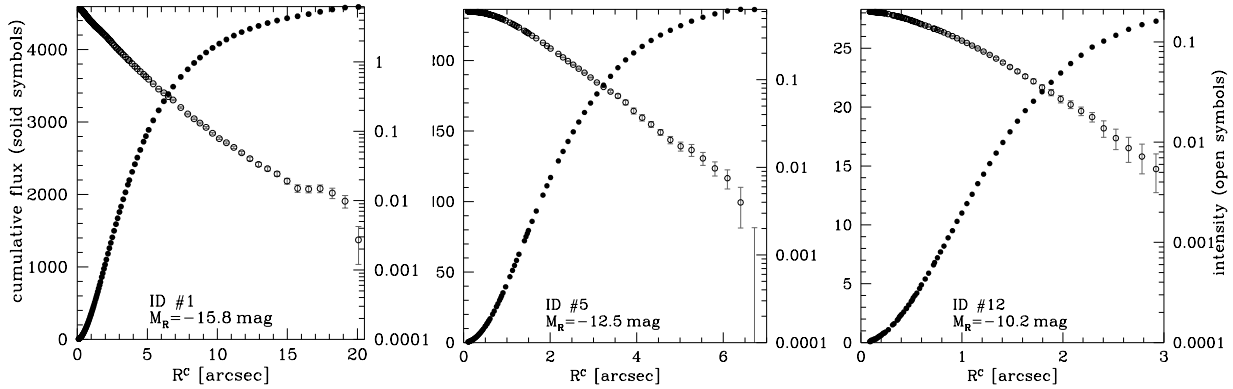

Figure 13: Intensity profiles (open symbols, right y-axis) and cumulative flux (solid symbols, left y-axis) of three arbitrarily chosen galaxies in the sample. Shown are all data points used for determining the total flux.

photometric calibration are listed. The photometrical uncertainties of the dwarf spheroidals (dSph) are dominated by sky noise.

The half-light radius r_{50} is determined as the radius enclosing 50% of the measured total flux f. We determine the mean $B-R$ color of each object using the flux within r_{50} as determined in R-band. Within r_{50} the signal-to-noise ratio is higher than for the total flux. In light of the crowded field and the transparency variations (see Sect. 2.4) in some cases a variable sky background can occur, making r_{50} more reliable for our color estimation, especially for very low surface-brightness targets for which total fluxes are difficult to determine.

4.2.2 *Fiducial sample definition via color-magnitude selection*

The colors of all objects with $B-R < 1.75$ mag and brighter than $M_R = -10.5$ mag are shown in the color-magnitude diagram (CMD) in Fig. 14. We consider redder galaxies to be background contamination[2]. Galaxies fainter than this limiting magnitude have very large $B-R$ color errors and are in the luminosity regime where the detection completeness is below 50%. The colors represent the integrated value within the half-light radius r_{50}. Only the color of the BGG, whose inner arcsec is saturated in R-band, is represented by its value at r_{50}. The $B-R$ value of the disrupted galaxy (at $M_R \approx -17.7$ mag) comes from SExtractor analysis. It is clearly visible in the plot that three disky galaxies fall almost exactly on the red sequence (RS hereafter). These are the S0 host of the disrupted galaxy, an S(lens)o and a dusty edge-on spiral – the bright blue square in Fig. 14. See ID 3, 6, and 2 in Table 6. The sample also contains two blue, almost face-on spirals and three dIrrs denoted by filled blue squares. The four brightest galaxies are spectroscopically confirmed group members (and indirectly the disrupted galaxy, see Sect. 5.5). Nicely visible in the CMD is the two-magnitude gap in R-band between the BGG and the second-ranked galaxy – one of the fossil criteria. Also noticeable is that the second brightest early-type galaxy has $M_R = -17.7$ mag – five magnitudes fainter than the BGG, already entering the dwarf galaxy regime.

To improve on the purely morphological constraints of group membership described in the previous section, we color-restrict our sample to galaxies that lie within 3σ of the red sequence (RS), whose location we determine with a least square fit to the data points shown in Fig. 14.

2 A 12 Gyr-old stellar population with super-solar metallicity ([Fe/H] $= +0.2$ dex) – typical of luminous early-type galaxies – has a $B-R$ color of ~ 1.75 mag (Worthey 1994).

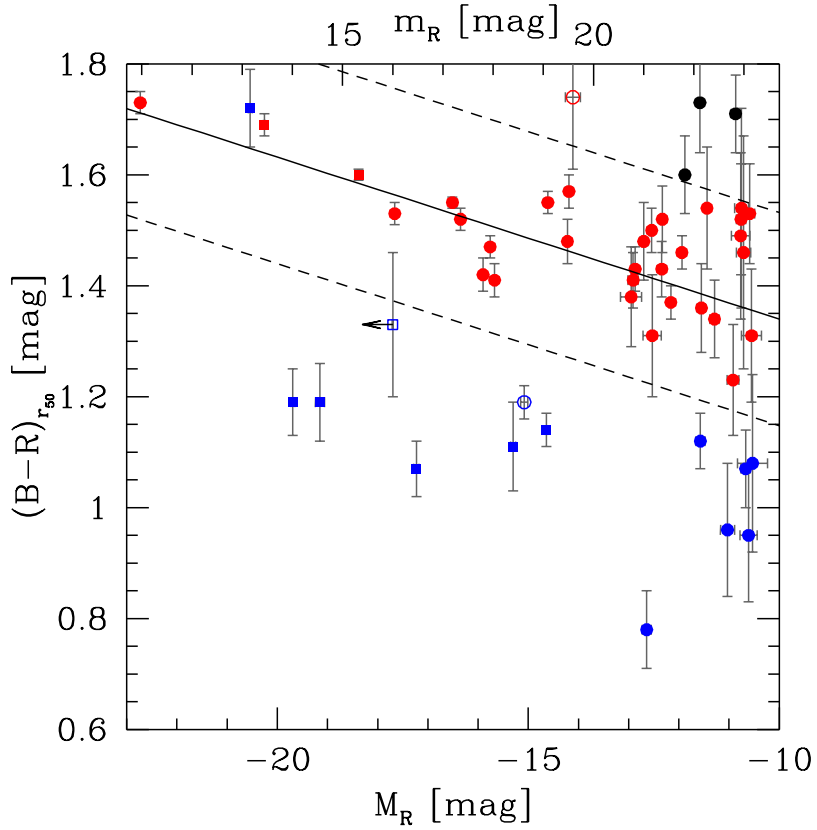

Figure 14: Color-magnitude diagram of all objects brighter than $M_R = -10.5$ mag (our 50% completeness limit) and bluer than $B - R = 1.75$ mag. $B - R$ colors represent the integrated value within the half-light radius determined in R-band, except for the BGG –where the color is determined *at* r_{50}–, and the disrupted galaxy (see Sect. 5.5). Red data points denote red sequence galaxies that we consider to be group members (circles: elliptical galaxies, squares: S0 galaxies), blue data points for blue cloud galaxies (circles: blue dSphs, squares: spirals and irregulars), respectively. Black data points are galaxies considered to be background galaxies. The open blue square denotes the disrupted galaxy of Sect. 5.5. Open circles (one blue, one red) represent galaxies with uncertain photometry because the galaxy is superposed on a brighter object (BGG or refraction halo of a star) that could not be fully modeled. Because of their morphology, those galaxies are included in the sample. The solid black line is a best fit for our red sequence CMR for galaxies brighter than $M_R = -14$ mag (see text). The dashed lines illustrate the 3σ level of confidence, which is used to reject background galaxies from the sample on the red side.

To not be affected by the larger scatter of faint galaxies we fit the RS only to galaxies brighter than $M_R = -14.0$ mag, and exclude the obvious blue sequence objects, as well as three photometrically uncertain galaxies.

We obtain the following least-square fit for the color-magnitude relation (CMR) of the RS in the NGC 6482 group

$$B - R = (-0.029 \pm 0.008) \cdot M_R + (1.05 \pm 0.13) \tag{3}$$

with an RMS of 0.06 mag. The index r_{50} given to the color legend $(B - R)$ on the y-axis indicates that the values are the average within the half-light radius. The CMR fits the relation defined by the brightest early-type galaxies in our sample well, down to $M_R \sim -14$ mag, and is also consistent with the color distribution of the fainter galaxies – even though these exhibit a larger scatter. In the following, every object within the 3σ RMS of the fit and brighter than $M_R = -10.5$ mag is considered to be an RS member of the group. We furthermore include two galaxies in this fiducial sample with uncertain photometry that formally places them redward

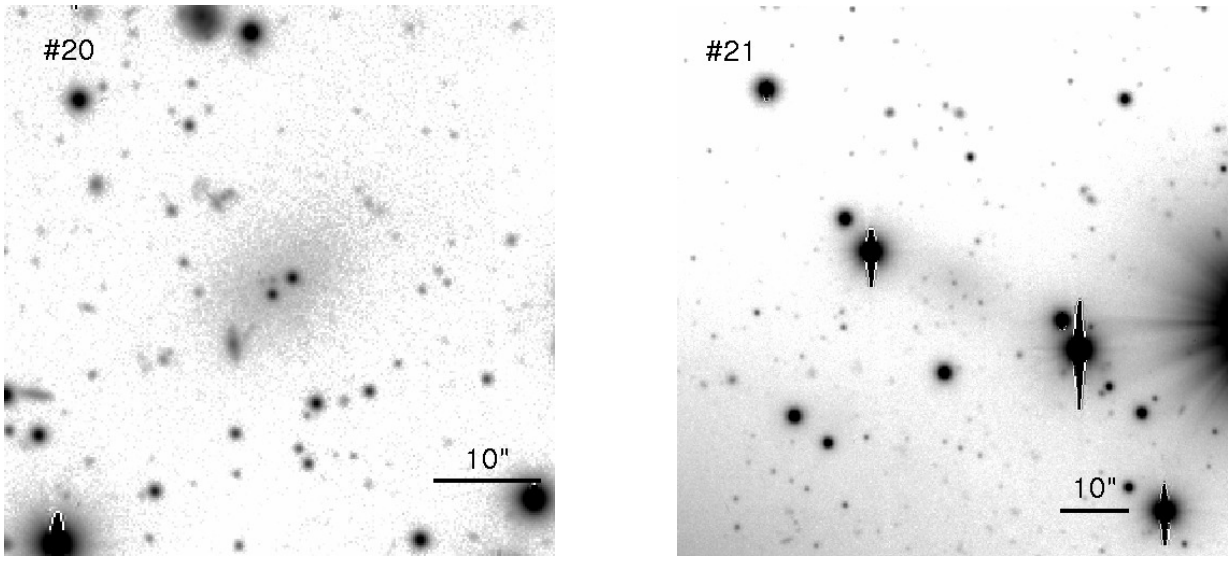

(a) dE(,N?) (b) dE,N

Figure 15: Galaxies with uncertain photometry due to BGG's halo and several stars in close proximity. We believe both galaxies are part of the group. In the righthand figure, we could not account for additional brightness gradients from the BGG and a very bright foreground star.

of the above 3σ range, but they morphologically resemble diffuse dwarf galaxies at the group's distance[3] (see also Fig. 15). Galaxies belonging to the blue cloud are labeled with blue datapoints. After selection around the red sequence, twelve out of 80 galaxies were considered to be background galaxies on the basis of their extreme red colors. Three of those are visible as black datapoints in the CMD. When only considering galaxies brighter than the 50% completeness level at $M_R = -10.5$ mag, 22 further galaxies are disregarded. Finally, including the two probable members with uncertain photometry mentioned above, this yields a fiducial sample of 48 probable group member galaxies (see Table 6).

4.3 SURFACE BRIGHTNESS PROFILES MEASUREMENTS

Surface brightness (SB) profiles of all investigated galaxies were analyzed using the analytic expression suggested by Sersic (1968). In our case we fitted single Sérsic profiles to the R-band SB obtained from the undegraded images (see Sect. 4.2.1), that is,

$$\mu(R^c) = \mu_e + 1.0857 \cdot b_n \left[\left(\frac{R^c}{r_e} \right)^{1/n} - 1 \right], \tag{4}$$

where μ_e is the SB of the isophote at the effective radius r_e. The constant b_n is defined in terms of the parameter n that describes the shape of the light profile. As shown by Caon *et al.* (1993), a convenient approximation relating b_n to the shape parameter n is $b_n = 1.9992n - 0.3271$ for $1 \leqslant n \leqslant 10$, which we applied in our calculations. The c in the variable R^c denotes that we performed the Sérsic fits with respect to the circularized radius $R^c = a\sqrt{1-\epsilon}$, where a is the major axis of the isophote with its ellipticity ϵ. We note that a multiple Sérsic fit would be more appropriate in the case of the S(lens)0 galaxy in our sample (ID 6 in Table 6) (see Kormendy &

3 These galaxies are listed in Table 6 with IDs 20 ($M_R = 14.2$ mag, $B-R = 2.48^{+0.12}_{-1.13}$ mag) and 22 ($M_R = 14.1$ mag, $B-R = 1.74 \pm 0.13$ mag

Bender 2012 and Janz *et al.* 2012). Thus, the errors of a single Sérsic fit are rather large for this galaxy. For consistency with the rest of the sample, we stick to a single fit as reference. We note at this point the importance of a reliable background estimation for the SB fits to dwarf galaxies. Caon *et al.* (2005) show that incorrect sky background estimates lead to significant differences in the Sérsic fitting parameters. We are confident that the individual curve-of-growth method described above gives a robust background estimate for each galaxy.

The Sérsic fits were performed with different fitting ranges. The standard fit excluded the inner two arcseconds (i.e., one arcsecond of R^c), which is about three times the seeing, and was performed until the intensity reaches $\mu_R = 26.5\,\mathrm{mag/arcsec^2}$. For some very faint SB profiles, the fit did not converge so that either only the inner arcsecond was excluded or the limiting SB was set to $\mu_R = 25.0\,\mathrm{mag/arcsec^2}$. Nonetheless, we tried to perform the fit with all of the three settings to get robust error estimates that are provided in Table 6. For nucleated galaxies, only the main body of the galaxy was fitted, excluding the central luminosity spike. Total luminosities were not computed from those fits, but from information of the total galaxy flux given by the `ellipse` outputs.

The results of these measurement are used to analyze the photometric scaling relations of dwarf galaxies in the fossil group NGC 6482, and to identify galaxies in our sample that exhibit centrally concentrated light profiles – typical of intrisically luminous galaxies – resulting in high Sérsic n (more than 2). In particular for galaxies with faint total magnitudes, this would indicate that they are background galaxies following Lieder *et al.* (2012).

5

RESULTS

Chapter taken from Lieder et al. (2013)

That galaxies are brighter in the R-band than in the B-band (~ 1.5 mag) roughly compensates for the missing depth in the R-band (~ 1.2 mag). Since the seeing is better in the R-band, we present all results related to the according R-passband quantities.

5.1 SPATIAL DISTRIBUTION

In Fig. 16 we present a $B - R$ color-coded, luminosity-scaled spatial distribution of all galaxies within the field of view that are considered group members. There is another spectroscopically confirmed group member outside the field of view with an apparent B-band magnitude of $m_B = 15.5$ mag (Zwicky *et al.* 1963) – comparable to the other spirals in this study.

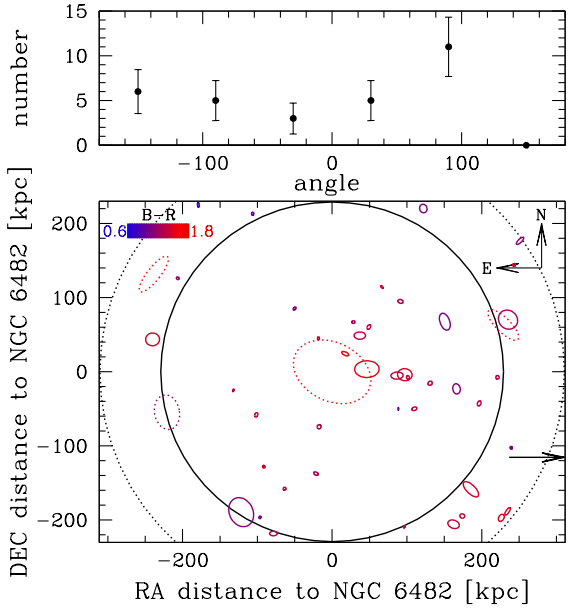

Figure 16: Lower panel: Spatial distribution of all galaxies considered group members (blue and red sequence, see Sect. 4.2.2). Spectroscopically confirmed group members are denoted by dotted shapes. All objects are color-coded with respect to their $B - R$ color, and the size of each galaxy is scaled to its luminosity by roughly $L^{0.03}$. Ellipticity and position angle are represented by its value at the half-light radius. The solid circle represents the area that is completely covered by our field of view ($r = 229$ kpc). The size of the dotted circle corresponds to the virial radius ($r_{vir} = 310$ kpc). The arrow in the southwest corner indicates that another spectroscopically confirmed cluster member lies outside the field of view. Upper panel: Angular distribution of all galaxies shown in the lower panel within the solid circle. The 0 deg position is north in the lower panel and the angle grows clockwise. The errors in this plot are Poissonian.

The investigation of the angular distribution of the group galaxies (only within the fully covered circle of 229 kpc) shows a preferred location of galaxies towards the west (90 deg position; see upper panel of Fig. 16). There are five galaxies in the far southwest end whose projections look very clustered. Those five galaxies may constitute an intruding subgroup.

Another constraint on the group membership of the mentioned galaxies arises from Fig. 17. There we plot the cumulative radial distribution of galaxies of certain magnitude intervals with respect to their distance from the BGG, to test whether they are clustered towards the BGG. From this plot it is evident that the bright galaxies ($M_R < -15$ mag) are concentrated around the BGG as compared to an uniform distribution of galaxies. This also holds for all galaxies we suppose to be group members.

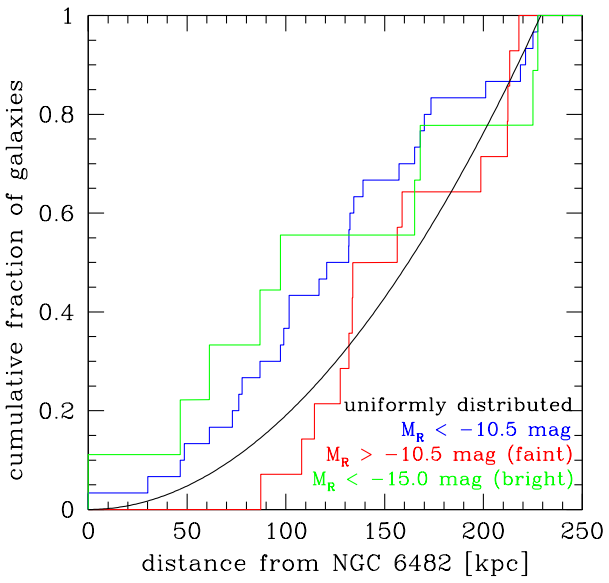

Figure 17: Radial distribution of investigated galaxies represented by their cumulative fraction with respect to their distance to the BGG. Only galaxies within the solid circle in Fig. 16 (largest completely covered annulus) are taken into account as long as they obey the membership constraints of Sect. 4.2.2. Green: bright galaxies ($M_R < -15$ mag). Red: faint galaxies ($M_R > -10.5$ mag). Light blue: all galaxies brighter than $M_R = -10.5$ mag. The black solid line represents a uniform distribution as would be the case for background galaxies.

5.2 PHOTOMETRIC SCALING RELATIONS

In Fig. 18 we present the most relevant photometric scaling relations of the galaxies presented in the CMD and the additional probable member with uncertain photometry at $B - R = 2.48$, ID 20 in Table 6, including effective SB μ_e at the effective radius r_e, effective radius, Sérsic index n, and total luminosity. The top panel in particular shows the correlation between effective SB and effective radius, also known as the Kormendy relation (Kormendy 1977). We stress here that all quantities except the total magnitude are values that arise from single Sérsic fits to the light profiles of the undegraded images (see Sect. 4.2.1) down to $\mu_R = 26.5\,\mathrm{mag/arcsec^2}$. We disregard central bright components like nuclei; i.e., only the main body of the galaxy is considered. Galaxies whose properties constitute strong outliers in these plots are typically candidates for background galaxies. There is one source that is an outlier in three of the four plots: this is the S0 galaxy (MRK 0895), the host of the disrupted galaxy (see Sect. 5.5), a spectroscopically confirmed cluster member. It has a comparatively high surface brightness and small size compared to the main body of group member galaxies that might be related to the edge-on view, which is simply an effect of its high inclination (see Fig. 21). We note that this galaxy is well fit by a single Sérsic profile (as seen in the right panel of Fig. 21). That the grand design spiral galaxies tend to deviate from the photometric scaling relations given by the early types is also visible in these plots. The spirals tend to have larger half-light radii and fainter effective SBs as expected from the early-type relations, resulting in lower concentration parameter n. This is expected since our Sérsic fits consider the disks alone. Two other outliers represent the probable members with uncertain photometry. These are the galaxies displayed in Fig. 15. For the galaxy with two foreground stars in the center, the low SB can be due to difficult masking that took most of its light.

Clear trends are visible in all relations in the sense that brighter galaxies are larger (r_e) and have brighter SB at the half-light radius and more centrally concentrated light profiles (Sérsic n). There is no faint galaxy with high Sérsic n that would qualify it as background galaxy. This is a consequence of our applied $\mu - mag$ selection criterion (see Sect. 4.1), which initially rejects faint galaxies with high central light concentration. Another point is worth mentioning. We do not see any galaxy within the interval $-14 < M_R < -13$ mag. A similar dip in the

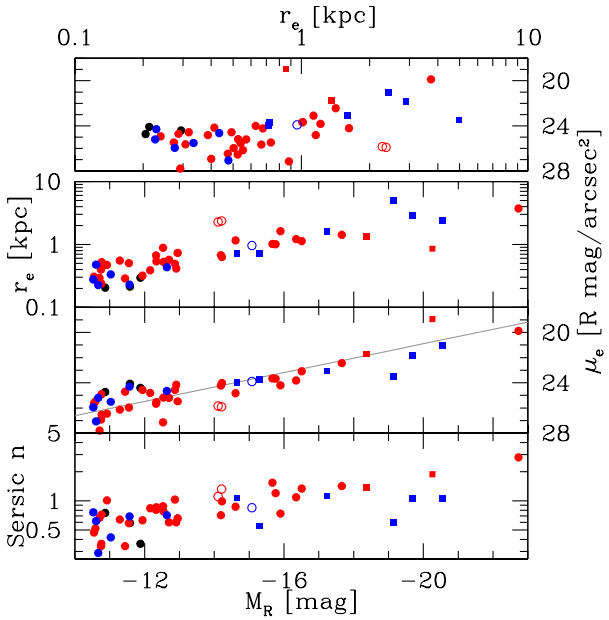

Figure 18: Photometric scaling relations of all investigated galaxies. Except for the total magnitude (curve-of-growth), all quantities arise from single Sérsic fits. In the case of spiral galaxies, the fit was performed to the disk; for dE,N only the main body was fitted. Symbols as in Fig. 14. While r_e is the effective radius, μ_e represents the effective SB (at r_e). The gray line in the $\mu_e - M_R$-plot gives the relation of Misgeld *et al.* (2009). The disrupted galaxy is not shown in this plot (no light profile available).

galaxy luminosity function around this magnitude was reported by Hilker *et al.* (2003) for the Fornax cluster. We, however, refrain from addressing the statistical significance of the gap and its origin owing to the low number statistics at these low luminosities.

5.3 LUMINOSITY FUNCTION

In Fig. 19 we show our completeness uncorrected galaxy luminosity function (1 mag bin width, steps of 1 mag). The sample used for the LF are the 48 galaxies considered as likely members, see Sect. 5.2. For a better visualization of the LF we use a binning-independent sampling of the completeness-corrected LF, performed by an Epanečnikov kernel (Epanečnikov 1969) with a bin width of 1.0 mag – displayed with red colors in Fig. 19.

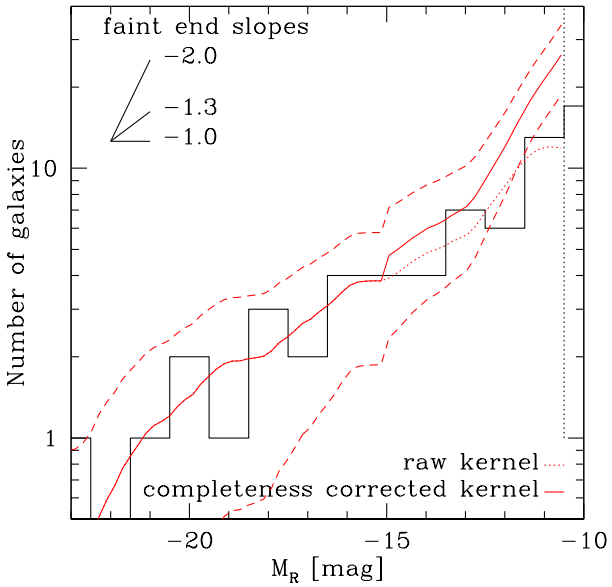

Figure 19: R-band luminosity function of member considered galaxies (see Fig. 14). The black histogram represents the observed data (bin width: 1 mag). The red dotted line is a binning-independent representation of the counts (Epanečnikov kernel of 1 mag bin width), while the red solid line is its completeness-corrected (see Sect. 4.1) counterpart with the 1σ uncertainty limits (dashed). The vertical dotted line is our 50% completeness limit at $M_R = -10.5$ mag. For comparison, some faint end slopes are illustrated in the top left corner of the plot. The best fit slope to our data is $\alpha \sim -1.3$, see text.

Because of the missing L^* galaxies in a FG, the bright end of the LF looks different from normal cluster LFs. Thus, a Schechter fit to the LF will only be poorly constrained at the bright end. Nevertheless, it is meaningful for the faint end. We performed a fit to the galaxy number count distribution (assuming Poissonian errors), including completeness correction for galaxies fainter than $M_R = -15$. The fitting interval was chosen to end with $M_R = -10.5$ mag (our 50% photometrical completeness limit). We fit the number count distribution of all galaxies in our imaging survey, noting that this only 84% of r_{vir} is covered by our dataset. The faint end slope of an error weighted Schechter function fit reveals $\alpha = -1.32 \pm 0.05$. A similar fit to the luminosity function within the circular region fully covered by our data ($0.74\, r_{vir}$, see Fig. 16), yields a marginally steeper slope $\alpha = -1.49 \pm 0.13$.

There is a hint of an upturn in the LF fainter than $M_R = -12$ mag, but completeness correction starts to play an important role in this magnitude range, such that we do not discuss it in more detail.

5.4 THE BRIGHTEST GROUP GALAXY NGC 6482

The radial SB profile of the BGG (see Fig. 20) is well described by a single Sérsic fit as the deviation of the photometric data to the fit (second panel) within the inner 100 arcsec remains at values smaller than $\Delta\mu = \pm 0.1$ mag/arcsec^2. We fit the light profile with respect to the circularized radius and exclude the inner 3 arcseconds (the inner 2 arcseconds are obviously affected by saturation) from the fit. Its Sérsic $n = 2.82 \pm 0.03$ – the light concentration parameter – is rather small for such a giant elliptical galaxy, given that a Sérsic $n = 4$ represents the typical de Vaucouleurs profile. In particular it is smaller than reported by Alamo-Martínez *et al.* (2012) who find values of ~ 3.9 in g- and z-band. However, smaller values of n for fossil group central galaxies were already reported by the FOGO collaboration (Aguerri *et al.* 2011; Méndez-Abreu *et al.* 2012), who obtain a mean Sérsic index of $n \sim 3$ for a sample of 21 FGs.

The inner isophotes ($10'' \leqslant R^c \leqslant 50''$) of NGC 6482 exhibit a moderately large ellipticity ($\epsilon \sim 0.3$), and turn into almost spherical isophotes in the outskirts ($R^c > 70''$). The elevated overall ellipticity is accompanied by a disky shape in the inner galaxy part (lower panel in

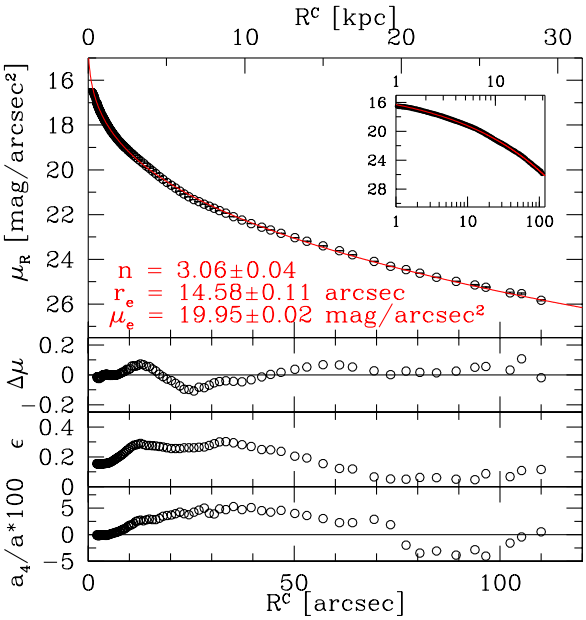

Figure 20: Radial profiles of the BGG NGC 6482. Top panel: SB profile, including a plot of logarithmic radial scale in the inset. In both cases the red line represents the single Sérsic fit, the fitting results are provided too. The second panel displays the deviation of the data from the Sérsic fit. The third panel shows the ellipticity with respect to radial distance and the bottom panel illustrates the a_4/a parameter that describes the deviation of the isophote from a perfect ellipse.

Fig. 20). This is seen from the a_4/a parameter, for which positive values denote disky isophotes (Bender 1988).

5.5 A DISRUPTED GALAXY AROUND MRK 895

In one particular case we observe a galaxy being disrupted by the confirmed group member galaxy MRK 895. This is an edge-on S0 galaxy as shown in Fig. 21. For the disrupted galaxy we can only provide SExtractor-based photometry. We tuned SExtractor to detect the whole debris. The obtained flux represents only a lower limit because we have masked point sources, as well as the hosting S0 galaxy. This fact is denoted by the arrow on this galaxy in the color-magnitude diagram (Fig. 14).

We masked the tidal debris for the `ellipse` investigation of the S0 galaxy in the outer regions, but did not mask it where the debris crosses the bright isophotes along the disk of the galaxy. Thus, the isophotes might be affected by light from the tidal debris. But this effect should not be significant for the total brightness of the S0 galaxy since the galaxy itself is very bright (see light profile in the right panel of Fig. 21).

The projected diameter of the debris is ~ 35 kpc. We investigated the $B-R$ colors of both the debris and the overdensity close to the northwest corner of MRK 0895. While the overdensity shows $B-R \sim 1.4$ mag, the rest of the debris shows $B-R$ colors of ~ 1.2 mag. The S0 galaxy itself has $B-R \sim 1.69$ mag as shown in Fig. 14 (the third brightest galaxy is the host). As a result, the debris is on average 0.3 mag bluer than its host. The disrupted galaxy is obviously not on the red sequence. The progenitor could have been a relatively luminous late-type and/or metal-poor system, since the flux of the whole debris adds to $M_R = -17.7$ mag.

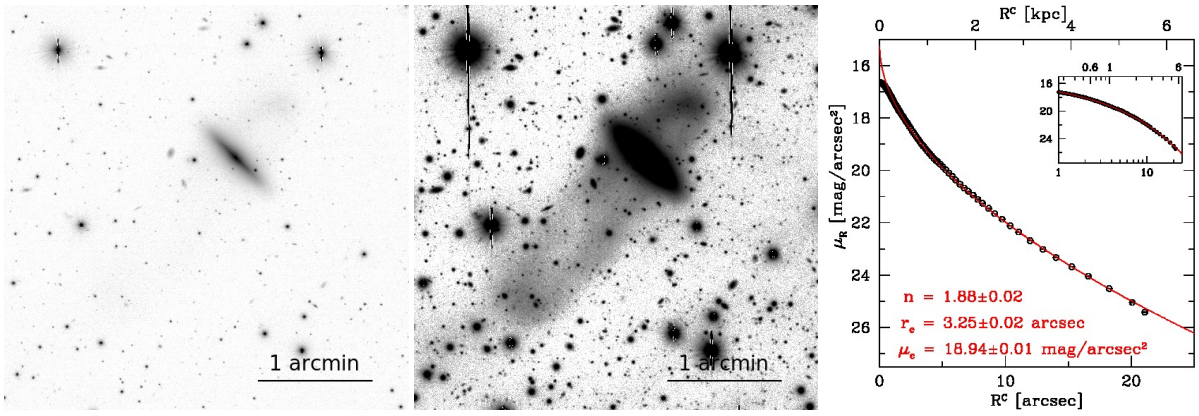

Figure 21: Detection of a galaxy being disrupted. Left: S0 galaxy MRK 895 by which the dwarf galaxy is being disrupted (north up, east left). Center: Image with different contrast settings to illustrate the tidal debris. Right: Light profile of the S0 galaxy. The red line visualizes the best Sérsic model to the data.

6

DISCUSSION AND CONCLUSIONS

Chapter taken from Lieder et al. *(2013)*

6.1 BRIGHTEST GROUP GALAXY

We find $B-R=1.73$ for the BGG NGC 6482, a color typical of metal-rich old stellar populations. Such a red color was also found for NGC 6482 by Alamo-Martínez *et al.* (2012) ($g-z=1.85$ at r_{50}). Another finding of our study is the relatively low Sérsic index of $n\sim2.82$ for NGC 6482, in agreement with the studies of the FOGO group, who find Sérsic indices around $n\sim3$ for FGs (Aguerri *et al.* 2011; Méndez-Abreu *et al.* 2012). They argue based on Hopkins *et al.* (2009) and Kormendy *et al.* (2009) that low Sérsic indices for giant ellipticals ($n\sim2.5$) are tracers for dissipational mergers. Bender *et al.* (1988) and Khochfar & Burkert (2005) find that disky isophotes of giant elliptical galaxies are the result of wet, gas-rich mergers, i.e., mergers with participation of spiral or irregular galaxies. We clearly see disky isophotes in the BGG ($a_4/a\sim0.05$) and Alamo-Martínez *et al.* (2012) identify a dust lane in their HST images of NGC 6482 – favoring the merger scenario of our FG as originally claimed by Ponman *et al.* (1994). But that does not necessarily disfavor the "failed group" scenario of Mulchaey & Zabludoff (1999). Dekel *et al.* (2009) suggested that inflows of cold streams might have been the major formation scenario in the early Universe. A rotational disk would have stayed intact while giant star-forming clumps merged into the center to form a massive spheroid. These star-forming clumps – one could call them galaxies – could leave an imprint on the BGG's morphology, such as disky isophotes or dust lanes. Oser *et al.* (2010) show in simulations that the majority of stars of an intermediate mass central galaxy (like our NGC 6482) have been formed ex-situ in clumps, thus they have been accreted. In this sense, a massive dark matter halo accompanied by cold gas streams would reflect the "failed group" scenario but should also show merger signatures. A difference in both formation scenarios would then become washed-out.

6.2 PHOTOMETRIC SCALING RELATIONS

We adopt the μ-mag relation of Misgeld *et al.* (2009) to simulate galaxies in order to discover dwarf galaxies in the NGC 6482 group. These relations agree well with the sample properties of the recovered dwarfs as seen in Fig. 18. Disregarding disky galaxies (i.e., spirals and Sos), most galaxies in the sample follow the same photometric scaling relations, indicating that they truly belong to the NGC 6482 group. However, at the faint end of the distribution background contamination should play an important role. We accounted for that by applying a certain color range for group members, following the CMR of the bright galaxies.
In general, the photometric scaling relations are very similar to those found in galaxy clusters. This includes the distribution in CM space (see Fig. 14) where both the red and the blue sequence are distinctly defined. Our best fit of the CMR to the RS has a slope of -0.029 ± 0.008, comparable to similar slope determinations in $B-R/R$ in some galaxy clusters(-0.045 ± 0.028

for Coma; Adami *et al.* 2006; (-0.055 ± 0.009 for Perseus; Conselice *et al.* 2002), possibly somewhat to the shallow side.

6.3 LUMINOSITY FUNCTION

Little is known about the faint satellite systems of FGs. The deepest observational study of a FG in the literature reaches $M_g = -16$ mag (Mendes de Oliveira *et al.* 2006) – that is four magnitudes fainter than the group's characteristic magnitude ($M^* + 4$ mag). Therefore no solid constraints on the dwarf galaxy regime can be drawn from these studies. Particularly the faint end slope of the LF has been poorly constrained up to now by other FG studies, and varies strongly from -0.6 to -1.6 (Cypriano *et al.* 2006; Mendes de Oliveira *et al.* 2006, 2009; Proctor *et al.* 2011; Eigenthaler & Zeilinger 2012).

Our study is, to our knowledge, the first one to deeply probe into the dwarf galaxy regime of a fossil group, extending the available literature studies by 6-7 mag in total luminosity. Our investigation reveals dwarf galaxies as faint as $M_R = -10.5$ mag. We find a faint end slope of $\alpha = -1.32 \pm 0.05$, fully within the range of values typically found in cluster environments (Table 4), such as Coma or more unevolved clusters like Virgo and Hercules. The faint end slope of a composite LF, averaged over 60 nearby galaxy clusters, reveals a similar value of $\alpha = -1.28$ (de Propris *et al.* 2003). Previous studies have suggested that indeed the faint end slope of the LF is independent of environment: Trentham & Tully (2002) show such an almost invariable faint end slope in their study of five different environments with varying galaxy density and morphological content. They find a composite faint end slope of $\alpha = -1.19$ for their entire sample. The result of our study, the first deep one in a fossil group, is consistent with the average slope found in a range of environments, and lends further credence to the notion that the faint end slope of the galaxy luminosity function depends only very little on environment.

Another useful parameter for describing the LF shape is the dwarf-to-giant ratio (Phillipps *et al.* 1998; Sánchez-Janssen *et al.* 2008). We compared our data with the study of Trentham & Tully (2002), adopting their definition of the d/g ratio as $d/g = N(-17 < M_R < -11)/N(M_R < -17)$. By taking the completeness correction into account, we obtain $d/g = 4.1 \pm 0.6$. The error acounts for color and magnitude uncertainties that could propagate into our group membership determination. The dwarf-to-giant ratio we find is consistent with the average $d/g = 3.2$ (rms 1.2) reported in Trentham & Tully (2002), and in particular matches the values they find for virialized systems like NGC 1407 and the Virgo cluster.

We do not find any galaxy in the magnitude range of $-14 < M_R < -13$ mag, best seen in Fig. 18. While this interesting feature of NGC 6482 might be due to the low number counts (Fig. 19), we note that a similar dip has been found by Hilker *et al.* (2003) in the Fornax cluster. As already noted by these authors, this magnitude range is the transition from dE to dSph.

Another two properties of dwarf galaxies are the fraction of early- to late-types and the fraction of nucleated dEs. Trentham & Tully (2002) find evidence that dynamically more evolved systems have a higher fraction of dE as compared to dIrr (see also Mahdavi *et al.* 2005). The percentage of dwarfs in the range $-17 < M_R < -11$ mag classified dE as opposed to dIrr is 89^{+1}_{-3} percent, comparable to the fraction Trentham & Tully (2002) that find in the central 200 kpc of Virgo cluster. The errorbars arise from photometric errors. Among the dEs, 38% are nucleated within the same magnitude range. This is comparable to the 40% of a combined nucleation rate of four groups in the Trentham & Tully (2002) sample but only half the nucleation they find for the Virgo cluster (70%).

We conclude that the NGC 6482 fossil group shows photometric properties consistent with those of regular galaxy clusters and groups, including a normal abundance of faint satellites.

Table 4: Luminosity function faint end slopes in literature.

group/cluster	α	band	reference
Virgo	-1.30	B	Sandage *et al.* (1985)
Coma	-1.41	R	Secker *et al.* (1997)
Hydra I	-1.13	V	Misgeld *et al.* (2008)
Centaurus	-1.14	V	Misgeld *et al.* (2009)
Hercules	-1.29	V	Sánchez-Janssen *et al.* (2005)
Fornax	-1.1	V	Hilker *et al.* (2003)
Perseus	-1.26	B	Penny & Conselice (2008)
diff. env.†	-1.19	R	Trentham & Tully (2002)
2dF	-1.28	b_J	de Propris *et al.* (2003)
NGC 6482	-1.32	R	this study

Notes. Faint end slopes α were derived by a single Schechter function fit.
† Composite LF (linear fit) of five different environments with varying galaxy density.

The potential *missing satellite problem* in this fossil group is thus on a similar scale to those in other environments.

Part III

SIMULATIONS

7

DATA

7.1 THE MILLENNIUM-II SIMULATION

The Millennium-II Simulation (MS-II) (Boylan-Kolchin *et al.* 2009) is a dark matter N-body simulation that incorporates ΛCDM cosmology. It is based on the Millennium Simulation (MS) (Springel *et al.* 2005b) as data structure and particle number ($\sim 10^{10}$) are the same. Both simulations were carried out in a periodic cube, i.e., a particle that escapes at one side will enter it through the opposite side. As compared to the MS, MS-II has the advantage of a five times better spatial resolution and thus a 125 times better mass resolution. The box size is $100\,h^{-1}\mathrm{Mpc}$, somewhat smaller but approximately the scale of the acoustic peak from BAO (Eisenstein *et al.* 2005; Beutler *et al.* 2011). At redshift zero, and accounting for the adopted cosmological parameters[1] in MS-II, this scale corresponds to a side length of 137 Mpc. A DM particle has a attributed mass of $6.9 \times 10^6 h^{-1} M_\odot$. The resolution limit of a halo is 20 particles which corresponds to a lower mass limit of $1.38 \times 10^8 h^{-1} M_\odot$. With this mass resolution, halos similar to those hosting the Local Group dSphs are resolved (Mateo 1998; Strigari *et al.* 2008a). Fig. 22 illustrates the variety of structure that arises from MS-II, from the large-scale cosmic web down to the smallest satellites embedded in larger DM halos.

The simulation data is preprocessed "on-the-fly" in order to identify DM halos. This is achieved by the friend-of-friends (FOF) algorithm, a technique originally invented to search for overdensities in spectroscopic galaxy surveys, later modified to look for structures in simulated galaxy data sets (Huchra & Geller 1982; Davis *et al.* 1985). The FOF approach is straightforward. It looks for particle pairs that are closer than a given cut-off separation. In the MS-II this linking length is chosen to be 20% of the mean particle separation. If at least 20 particles could be linked that way, it was considered a halo and retained for later analysis. At $z = 0$, in the full MS-II about 60% of all DM particles belong to $\sim 10^7$ FOF groups. Those FOF halos are teemed with substructure, as illustrated in the lower-left panel of Fig. 22 which shows the largest FOF group in the simulation.

In a post-processing step, it was searched for that substructure within FOF groups using the `SUBFIND` algorithm that identifies "substructure candidates as regions bounded by an isodensity surface that traverses a saddle point of the density field" (Springel *et al.* 2001). All self-bound substructures containing at least 20 particles were stored as *subhalos*. The most massive subhalo within a FOF group is called the main (sub)halo of the group, and usually contains most of its mass. Each subhalo found in a given output was then linked to *one* descendant subhalo in the following output. The so constructed *merger trees* thus mimic structure growth by merging of subhalos, and not by merging of halos. Sometimes a subhalo is not identified by `SUBFIND` when passing through the center of the FOF halo (Boylan-Kolchin *et al.* 2009), but found again in the subsequent output. However, those cases are very rare.

1 $\Omega_m = 0.25$, $\Omega_b = 0.045$, $\Omega_\Lambda = 0.75$, and $H_0 = 73\,\mathrm{km\,s^{-1}Mpc^{-1}}$

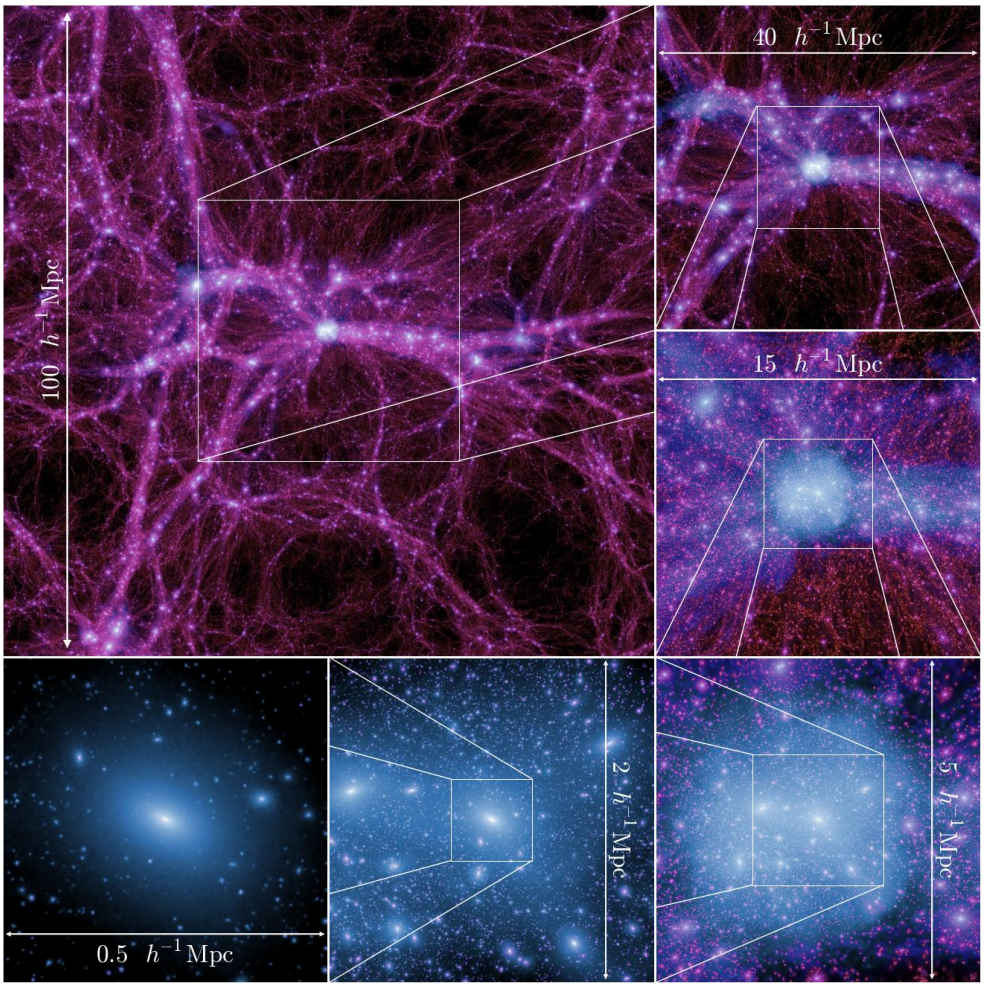

Figure 22: A sequential zoom through the Millennium-II simulation. The upper-left panel is a $15h^{-1}$Mpc thick slice of the full $100h^{-1}$Mpc simulation (in comoving coordinates). The sequence is centered on the most massive halo of the simulation ($8.2 \times 10^{14}h^{-1}M_{\odot}$) – similar to the Coma cluster (Colless & Dunn 1996). The cosmic web is clearly seen and even on the smallest scale $0.5h^{-1}$Mpc a rich variety of substructure is visible. Figure taken from Boylan-Kolchin *et al.* (2009), their Fig. 1.

Beside the total mass of all FOF group members M_{FOF}, MS-II provides three more definitions to determine a mass within a spherical region. The center of a FOF halo is in every case defined as the position of its main subhalo. We will stick to the definition of the virial mass M_{vir} given in Sect. 1.2, i.e., the mass within the largest sphere with the mentioned center and a mean overdensity that exceeds 200 times the critical value. The radius of this sphere is the virial radius R_{vir}. Both are linked to each other by

$$R_{vir} = \left[\frac{G}{100}\frac{M_{vir}}{H^2(z)}\right]^{1/3} \tag{5}$$

whereas G is the gravitational constant and $H(z)$ is the redshift dependent Hubble constant. Hence, the virial mass contains all masses of particles within the sphere, if SUBFIND consideres them to belong to the group or not (see above). However, Guo *et al.* (2011) mention that the virial radius usually lies entirely within the boundary of the FOF group, i.e., the virial mass always takes masses into account that are physically FOF group members. The reader is re-

ferred to Springel *et al.* (2005b) and Boylan-Kolchin *et al.* (2009) for a detailed description of the simulations.

Outputs are saved in 68 epochs, so-called *snapshots*. 65 of those snapshots are spaced according to

$$\log_{10}(1+z_N) = \frac{N(N+35)}{4200} \qquad (0 \leqslant N \leqslant 64) \tag{6}$$

and three snapshots at high redshift $z = 40$, 80 and 127. The latter corresponds to a lookback time of $\sim 13.6\,\mathrm{Gyr}$. Table 7 shows that the snapshots are not equally spaced in time.

7.2 THE SEMI-ANALYTIC MODEL OF GUO *et al.* (2011)

We will use the semi-analytic model provided by Guo *et al.* (2011) (G11 hereafter) to investigate properties of FGs in general but also to compare the results of our observations to predictions of simulations/SAMs. The model uses the MS-II and bases on the SAM by de Lucia & Blaizot (2007) (DLB07), which successfully described the homogeneity of local BCGs properties and it has drawn a link between those and high redshift galaxies. The DLB07 model utilized the MS with its lower mass resolution. Guo *et al.* updated and extended the DLB07 model, and applied it additionally to the MS-II in order to put constraints also on the dwarf galaxy population. Their galaxy formation model incorporates following baryonic processes.

Reionization is included by a model that describes how the baryon fraction in a halo depends on mass and redshift (Gnedin 2000). A universal baryon fraction of 17% is adopted, based on the first year WMAP results (Spergel *et al.* 2003). It is shown that reionization has no major impact on galaxy formation, except, maybe for the faintest satellite systems.

Cooling happens as diffuse gas joins a halo. At early times and in low mass halos, the material is essentially available in free-fall time by cooling. In massive galaxies ($\geqslant 10^{12} M_\odot$) a shock front occurs in the outer regions of the galaxy, creating a hot atmosphere of infalling (and shocked) gas. This gas is then accreted by cooling flows. The gas accretion rate on a halo for both regimes is estimated by models of Springel *et al.* (2001) and de Lucia *et al.* (2004). This makes condensation on the center smooth in time and not instantaneously. The important difference to DLB07 is that satellite galaxies are allowed to have gas halos which can be removed gradually (see below).

The *disk* of a galaxy is distinguished between gas disk and stellar disk. Both are allowed to grow in mass and angular momentum. While the gas disk grows by gas accretion or minor mergers, the angular momentum of the stellar disk can only be changed by star formation, transferring mass from the gas disk to the stellar disk. Both the gas and the stellar disk are assumed to be thin, to have exponential density profiles, and to have maximum circular velocities of the surrounding DM halo. The derived stellar light concentrations and sizes of both discs in this simple model are fairly in agreement with observations (Guo *et al.* 2011).

Star formation is assumed to happen from cold gas according to an empirical relation which links star forming regions of star forming galaxies to high surface mass density regions contained in the cold gas disk (Kennicutt 1998). The process is efficient if a certain threshold for local instability in the rotationally supported disk is exceeded. The G11 model assumes that a few percent of cold gas is turned into star each rotation period of the disk. This model is basically similar to the one imposed by DLB07 but the revised cooling treatment leads to a

smoother evolution of the star formation rate, i.e., star formation histories are generally less "bursty".

Supernova (SN) feedback is adjusted to observed stellar mass functions such that the efficiency of gas reheating and ejection increases when galaxies become more massive. This is done in order to account for the observed suppression of star formation in low-mass galaxies. The ejected hot gas can be retained in an ejecta reservoir and fall back on the galaxy by cooling, which is a substantial difference to the DLB07 model.

Satellite galaxies are divided into "satellites" and "orphans". While satellites or type 1 galaxies have a dominant DM component, in orphan galaxies (type 2) the DM halo is not existent anymore, i.e., below the resolution limit. All galaxies are born as type 0 galaxies, become type 1 as they fall into a group or cluster and turn into type 2 when they get merged onto the cluster center. Basically, the central galaxies of groups/clusters associated with the main subhalo of a FOF group are in every case type 0 galaxies, but not vice versa. When a "normal" type 0 galaxy becomes member of a FOF group its label is switched to type 1.

Tidal and ram-pressure stripping is enabled when a satellite galaxy (type 1) enters the virial radius of the main halo of the central galaxy (type 0). Only within the virial radius thus a satellite galaxy can become gas stripped. In the model, hot and ejected gas is continuously stripped equally at each time-step. This is not a realistic setting, since ram-pressure stripping can already occur at earlier stages of the infall (Bahé *et al.* 2013) and ram-pressure depends on the density of the intracluster medium (ICM) which increases inwards. Additionally, the cold gas component is (unrealistically) not affected by ram-pressure stripping. Only material that is located outside a stripping radius[2] remains in the subhalo.

The improvement to DLB07 manifests in the on average later gas loss of satellite galaxies which is incremental rather than abrupt. When they enter a FOF group one thus expects that they continue star formation for longer time as compared to DLB07. However, Guo *et al.* (2011) show that the so achieved morphology-density relation is still too strong as compared to observations, i.e., real satellite galaxies retain their gas longer in dense environments, resulting in a larger fraction of star forming galaxies in clusters. They argue, this is a result of the enhanced SN feedback which was imposed to match the observed stellar mass function.

Disruption of the stellar component can only occur after the DM halo of the satellite has been stripped completely, i.e., the satellite (type 1) has become an orphan (type 2). This galaxy orbits within the potential of the main DM halo. As soon as the DM density of the main halo exceeds the baryon density of the remaining (stellar and cold gas) halo, the orphan galaxy is disrupted instantaneously. That is, disruption does not occur continuously. In particular, the cold gas is added instantaneously to the hot gas atmosphere of the central galaxy, not being able to form stars anymore. Furthermore, Guo *et al.* (2011) mention that dynamical friction on the satellites is not accounted for properly since it only considers the DM particles. Often, the DM subhalo is less massive than the stellar component, falsifying the expected decay of the galaxy.

Mergers in the model can occur both between centrals and satellites and among satellites. As soon as the DM mass drops below the baryonic mass of the galaxy, the merger countdown is triggered. Merging bases on dynamical friction and the merging time for a satellite is estimated by the formula given by Binney & Tremaine (2008), taking into account both DM and baryonic

2 The stripping radius of a satellite galaxy is a value that takes tidal forces as well as ram-pressure stripping into account. It essentially becomes smaller with decreasing distances to the main subhalo.

mass. Orbits of type 2 galaxies decay linearly with time as it is expected from a satellite that spirals to the center of a larger host. During a major merger (baryonic masses of galaxies differ by less than a factor of three) the discs of the participating galaxies are destroyed and an ellipsoid is created. In the case of a minor merger, in turn, the disk of the larger galaxy remains intact. In both cases a starburst is triggered, following Somerville *et al.* (2001). That is, a fraction of the cold gas contained in both galaxies is converted into stars. These are added to the disk of the remnant in the case of a minor merger. A major merger, on the other side, expels (almost all of) the remaining cold gas from the remnant by the strong SN feedback.

Bulge formation is achieved in Guo's model by either a merger or secular evolution of a disk. While a major merger ends up in an ellipsoid, a minor merger remnant forms a bulge that consists of all stars from the minor progenitor. The other possibility to transfer mass from the disk to the (possibly already existing) bulge is to apply a criterion for disk instability (Efstathiou *et al.* 1982) which was slightly modified. It is shown in the paper that disk instability is the major contributor to bulge formation for intermediate-mass galaxies, while mergers dominate the other mass regimes. However, the comparison with SDSS data reveals that the agreement with observed stellar mass concentrations "is fair, at best" (Guo *et al.* 2011). In particular the light of low-mass galaxies is too strong dominated by the disk. This is explained by the possible dissipation of gas during mergers, not taken into account.

Black hole growth and AGN feedback occur in two modes, following (Croton *et al.* 2006): "quasar" mode and "radio" mode. Quasar mode applies to black hole growth owing to gas-rich mergers, and is adjusted in order to match the observed relation between black hole mass and bulge mass. Feedback is not modeled explicitly but incorporated in the starburst that follows the accretion onto the black hole. Radio mode growth is related to hot gas accretion onto the central black hole of galaxies which deposits energy in relativistic jets which in return heat the hot gas atmosphere. This AGN feedback is able to disrupt type 2 galaxies, and, moreover, can also operate in low-mass satellite galaxies since they are also associated with hot gas. Essentially, the quasar mode dominates black hole growth in any case.

Metal enrichment by supernovae happens as both heavy elements and a fraction of the star's mass are deposited instantaneously in the cold gas component of a galaxy. Metals are then carried into the hot gas atmosphere by SN winds. This atmosphere can then be stripped subsequently, which enhances metals in the inter cluster medium. The model is adopted from de Lucia *et al.* (2004).

Stellar population synthesis by the models of Bruzual & Charlot (2003) adopting a Chabrier initial mass function is employed in order to compute the photometric properties of the model galaxies – like stellar masses and realistic magnitudes. *Dust extinction* is kept redshift dependent in order to account for observations.

In their paper, Guo *et al.* (2011) focus on evaluating improvements as compared to DLB07 and differences between MS-II and MS. We are interested in comparing our photometrically obtained results to the Guo model. There are two particular photometric properties that shall be mentioned here. First, the LF at redshift 0 deviates at both ends when comparing it to the SDSS data of the nearby universe. This is displayed in Fig. 23. The abundance of dwarf galaxies is underpredicted by the model, independent of the observed band. G11 speculate that either assigned mass-to-light ratios are too large for dwarfs, or the observational data overcorrects for

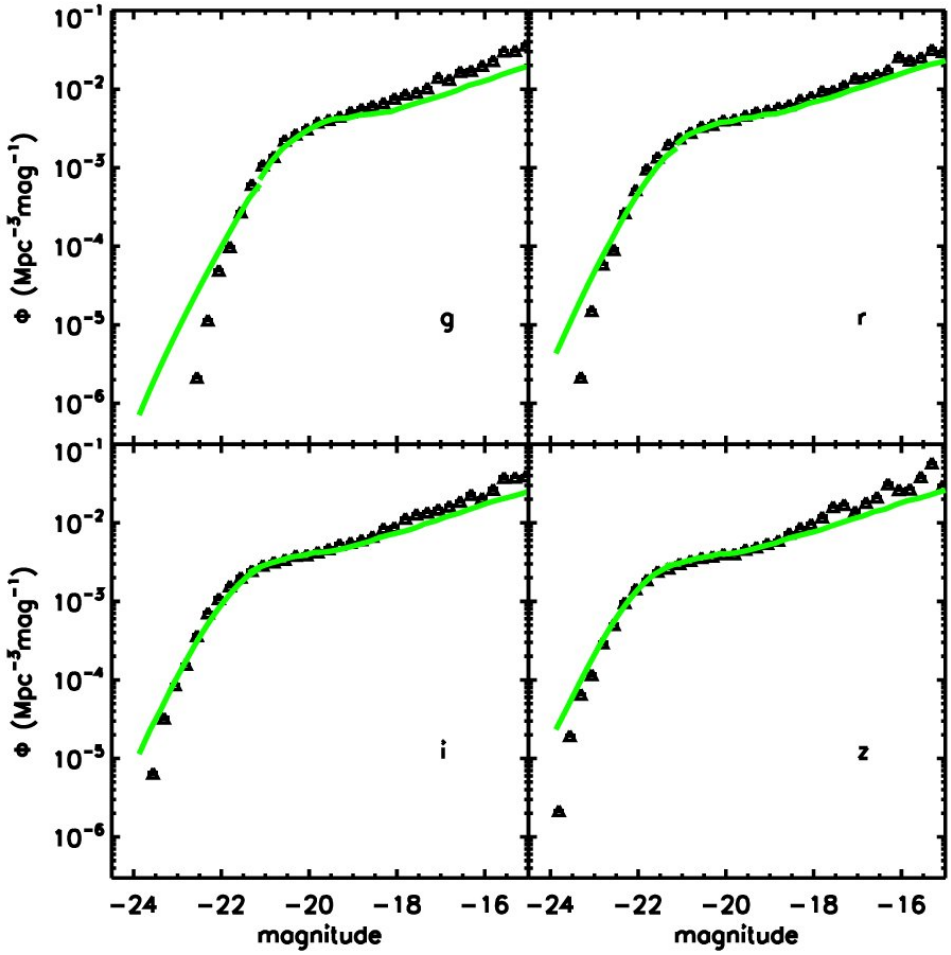

Figure 23: Galaxy luminosity functions in the SDSS compared to Guo's SAM. Black data points are SDSS low-redshift data from Blanton *et al.* (2005). The green line is the prediction by the Guo model. While data with absolute magnitudes fainter than −20 results from MS-II alone, the bright end is results from MS+MS-II in order to cancel out cosmic variance. While the model underpredicts the abundance of faint galaxies, the number of bright galaxies is overpredicted as compared to the nearby galaxy sample. Figure taken from Guo *et al.* (2011), their Fig. 8.

incompleteness at the faint end, or cosmic variance[3] influences the observational data. Possibly, all of the reasons are applicable. Similarly, there are too many bright galaxies at present time predicted by the model, in particular in the g band. This might be indicating that the applied dust model fails to predict sufficient extinction.

The other point concerns the colors of galaxies. As illustrated in Fig. 24, low-mass galaxies are too red in the G11 model, while luminous galaxies are too blue in turn. For the latter difference, the paper makes K-corrections[4] and the uncertain photometry of the observational sample responsible. For lower masses it is mentioned only that the dwarfs are finishing star formation too early which makes them passive and red. This picture is supported by the finding of an "overly high redshift of the peak of the star formation history" (Guo *et al.* 2011), i.e.,

3 Cosmic variance is the uncertainty in observational estimates for the volume density of galaxies. It arises from the limitation of the volume, even in large surveys, which do not cover large-scale density fluctuations (see Somerville *et al.* 2004).

4 The flux of an astronomical source within a given band(width) varies with redshift owing to the shift of its spectrum. The K correction accounts for this flux difference when comparing the flux of two objects at different to each other (see Hogg *et al.* 2002).

dwarf galaxies form too early in the model. Another particular hint is provided by Weinmann *et al.* (2011) who find that the red fraction of dwarf galaxies in model clusters is too high. They show that this is owing to environmental effects. Ram-pressure-stripping is too strong in the G11 model and tidal disruption may be insufficient so that too many red dwarfs survive. However, Fig. 24 also tells us that the majority of galaxies in the intermediate mass range $9.5 \leqslant \log M_* \leqslant 11.0$ are "in reasonable agreement with observations". It is mentioned by Guo *et al.* (2011) that the reddest galaxies are dominated by passive galaxies containing a disc, in particular at intermediate mass.

For the sake of completeness, it shall be mentioned that Guo *et al.* (2013) updated MS and MS-II by scaling structure growth in a ΛCDM universe to the cosmological parameters consistent with seven-year WMAP results (Komatsu *et al.* 2011) and applied their SAM to those scaled versions. In particular the matter density Ω_m and σ_8, the RMS density fluctuation amplitude of a top-hat sphere of $8h^{-1}$Mpc radius, have changed significantly since the first-year WMAP results originally adopted in both simulations. It was already realized by Guo *et al.* (2011) that clustering at scales below ~ 1 Mpc is overpredicted, suggesting that the implemented σ_8 value was too high. However, the effects of the change in both parameters cancel out, i.e., the predictions with updated cosmology are very similar to those of the original model.

We will stick to the Guo *et al.* (2011) model in this work. Although some critical points were raised in the above text, it is a state-of-the-art SAM that incorporates many aspects of galaxy formation and evolution and its comparison to observations is generally in reasonable agreement.

7.3 SELECTION OF CLUSTERS AND GROUPS

We aim to investigate not only fossil groups but also their link to "normal" galaxy groups, if there is. On the other hand, we are interested in comparing our observationally obtained results of NGC 6482 to FGs in the Guo SAM. Prior to the investigation of FGs we additionally aim to compare our results to those of the FG studies in the framework of the Millennium Gas Simulation by Dariush *et al.* (2010). They investigated only "FGs" more massive[5] than $\sim 2 \times 10^{13} h^{-1} M_\odot$, hence "fossil clusters" (see their Fig. 1). Therefore, we select galaxy groups from the Guo catalog with virial masses[6] larger than $10^{12} h^{-1} M_\odot$. That is, we pick the 3542 most massive galaxy groups and clusters from the $\sim 10^7$ FOF groups in the MS-II.

5 Note, that we will use the cosmological parameters specified in the MS-II, in particular the dimensionless Hubble parameter $h = 0.73$

6 The virial mass provided by the Guo tables is taken from MS-II and therefore takes only dark matter into account.

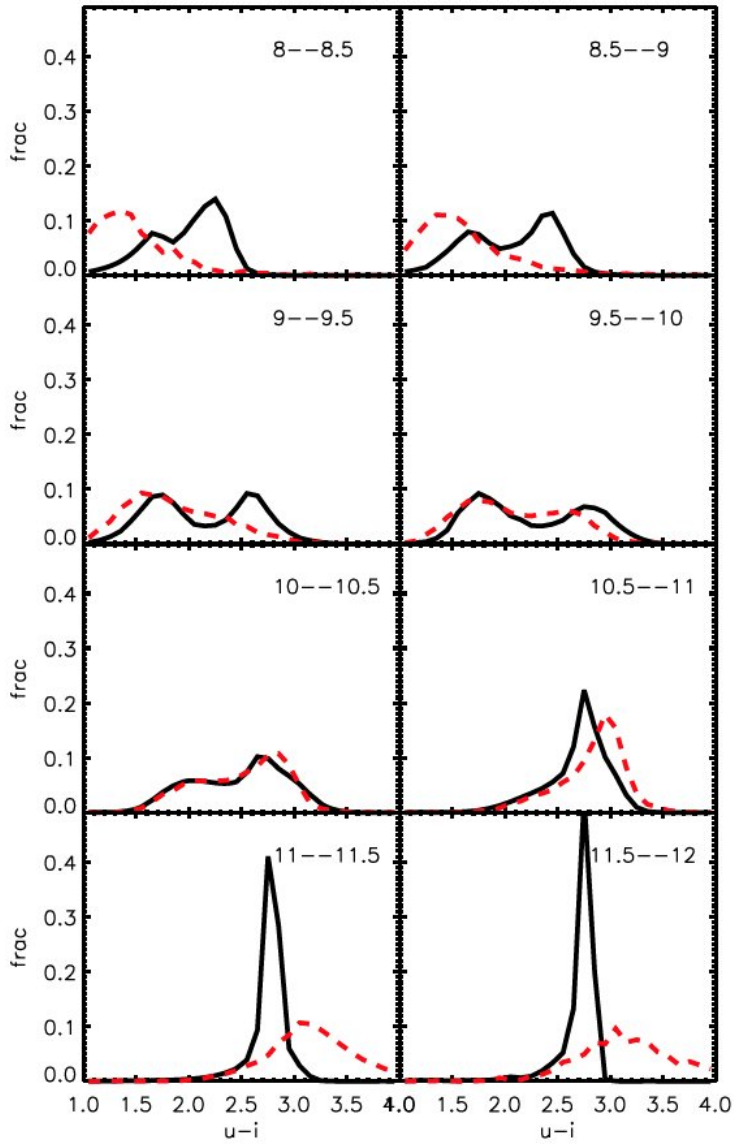

Figure 24: "u − i color distributions as a function of stellar mass. Solid black curves show distributions predicted by Guo's model, applied to the MS (above $\log M_* = 10.0$) and MS-II (at lower masses), while dashed red curves are distributions compiled from SDSS/DR7. The range in $\log M_*/M_\odot$ is indicated at the top right-hand side." Clearly, the model overpredicts red low-mass galaxies but underpredicts red high-luminosity systems. Figure taken from Guo *et al.* (2011), their Fig. 12.

8

DEFINITION AND LITERATURE EVALUATION OF FOSSIL SYSTEMS

8.1 THE X-RAY LUMINOSITY CRITERION

We recall the definition of a fossil group from Sect. 1.5. There has to be a central elliptical galaxy that dominates the group by a magnitude gap to the second ranked galaxy of two or higher. It has to be associated with a hot gas halo that exceeds a certain X-ray luminosity L_X. The latter turns out to be a problem in the G11 tables since no L_X is provided in the publicly available data. On the other hand, the definition by Jones *et al.* (2003) also provides a clue to solve it. The only reason to apply the X-ray luminosity criterion was to ensure that we deal with the central galaxy in the group. The G11 tables provide a parameter `type` which is the galaxy type mentioned in Sect.7.2. A type zero galaxy is supposed to be the central galaxy in the FOF group because it contains the most bound DM particle. In reality, this is similar to, e.g., the Virgo cluster, where the central galaxy M87 is associated with the largest DM halo traced by the hot gas in the X-ray (Böhringer *et al.* 1994). Hence, we translate the X-ray luminosity criterion of the fossil definition into: a galaxy being identified as a type zero.

Another approach to obtain an X-ray luminosity is provided by Stanek *et al.* (2010). They make use of the Millennium Gas Simulations[1], a resimulation of the MS with gas particles. For the (more realistic) PH simulation which includes preheating and cooling of gas along with shock heating, they provide a relation between the virial DM halo mass and the bolometric X-ray luminosity L_{bol} of the associated hot gas component at $z = 0$.

$$\langle \ln L_{bol} \rangle = -1.653 + 1.868 \times \ln M_{vir} \tag{7}$$

whereas M_{vir} is given in units of $10^{14} h^{-1} M_\odot$ and L_{bol} in units of $10^{44} erg\, s^{-1}$. Dariush *et al.* (2010) (D10 hereafter) investigate fossil cluster properties utilizing the SAMs of Croton *et al.* (2006) and Bower *et al.* (2006), based on X-ray luminosities originating from the above mentioned PH simulation. In their Fig. 1 they provide a visualization of Eq. 7 including its scatter (see Fig. 25). There are three points to make about this plot.

1. Above $\log(M_{vir}/h^{-1}M_\odot) \sim 13.5$ all clusters fulfill the X-ray luminosity FG criterion.
2. When using Eq. 7, the virial mass of a cluster, which scratches the X-ray luminosity limit of $0.25 \times 10^{42} h^{-2} erg\, s^{-1}$, is $\log(M_{vir}/h^{-1}M_\odot) \sim 13.2$. Of course, the scatter around the relation introduces an uncertainty to the mass.
3. Most important, clusters below $\log(M_{vir}/h^{-1}M_\odot) \sim 13.2$ do not accumulate enough hot gas to exceed the FG X-ray luminosity. In other words, NGC 6482 should not exist as a group with FG X-ray luminosity. But we have to admit, there are not many halos with masses lower than that.

1 The Millennium Gas Simulations should be treated with care because there is no publication available describing it, even unrefereed.

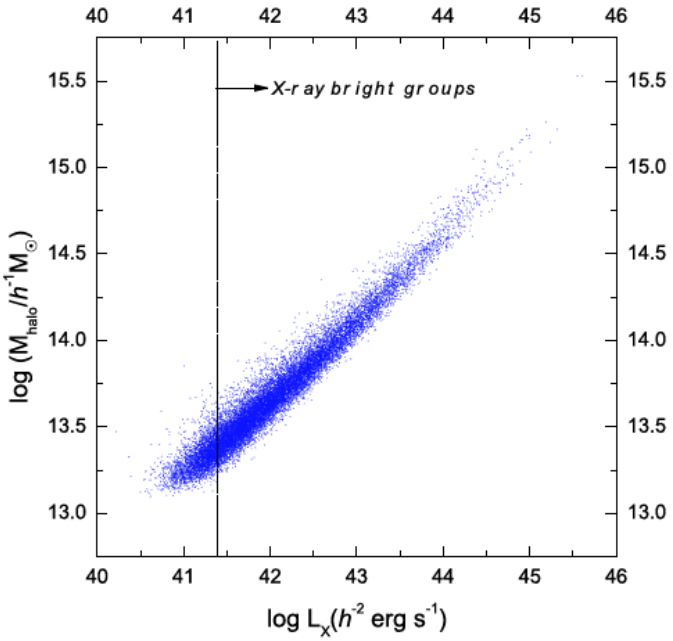

Figure 25: "The relation between the mass of group haloes (within R_{200}) at $z = 0$ from the Millennium DM simulation, and the bolometric X-ray luminosity of the corresponding haloes in the Millennium gas simulation. All groups have $M(R_{200}) \geqslant 10^{13} h^{-1} M_\odot$ at $z \sim 1.0$. The vertical dashed-line corresponds to the X-ray luminosity threshold $L_{X,bol} = 0.25 \times 10^{42} h^{-2} \mathrm{erg\,s^{-1}}$ generally adopted to define fossil groups. Of the 17866 groups matched in the two catalogues, 14628 groups lie above this threshold." Figure taken from Dariush *et al.* (2010), their Fig. 1.

This thesis' focus is on the mass regime of NGC 6482, i.e., on FGs with masses lower than $10^{13} M_\odot$, which are not considered in the analysis of D10. We will avoid the L_X criterion for FGs because we know, when a galaxy resides in the center of a cluster and is not accidentally a bright galaxy in its outskirts. However, we will discuss the results of D10 in the context of our study. Knowing that fossil clusters can occur at masses $\log(M_{vir}/h^{-1} M_\odot) \geqslant 13.2 \approx 2.2 \times 10^{13} M_\odot$, we talk about galaxy clusters in the following when this mass is exceeded. It is roughly a tenth of the Virgo cluster virial mass and half as massive as the Fornax cluster (McLaughlin 1999; Drinkwater *et al.* 2001; Urban *et al.* 2011). Using this definition, we find 180 clusters in the MS-II at $z = 0$.

8.2 THE MAGNITUDE GAP

The most distinct property of fossil groups is the large magnitude gap between the first and second ranked galaxy. In this section this gap is investigated to get an insight to fossil groups and to figure out how these can be distinguished from "normal" groups. We will specify the magnitude gap Δm_{12} as the difference in r band luminosity between the central galaxy of a FOF group and the brightest group member within half the virial radius given in the G11 tables. Of course, Δm_{12} is the gap between the first and second ranked galaxy. For fossil groups it is indeed larger than 2. Generally, a galaxy brighter than the central one may reside within $0.5\, r_{vir}$ though. This is the case, for instance, if two groups encounter or a nearby giant galaxy has a significant star burst. In conclusion, values $\Delta m_{12} < 0$ may occur.

In Fig. 26 we visualize the magnitude gap at present time as a function of the assembled mass fraction at $z = 1$ to the value at $z = 0$. This study has been performed by D10 for the SAM of Bower *et al.* (2006) (see Fig. 26a), and we compare it to the G11 model in Fig. 26b. The basic finding in the cluster regime of the MS is that the most massive clusters form late. They have assembled only about 20% of their final mass at $z = 1$ (bluish data points). Less massive clusters (reddish data points) tend to assemble earlier but, generally, the majority of all clusters assemble their masses late if we define "late" as "assembling more than half of their masses during the last 7.7 Gyrs". The plot also tells us that low-mass clusters are more likely to form

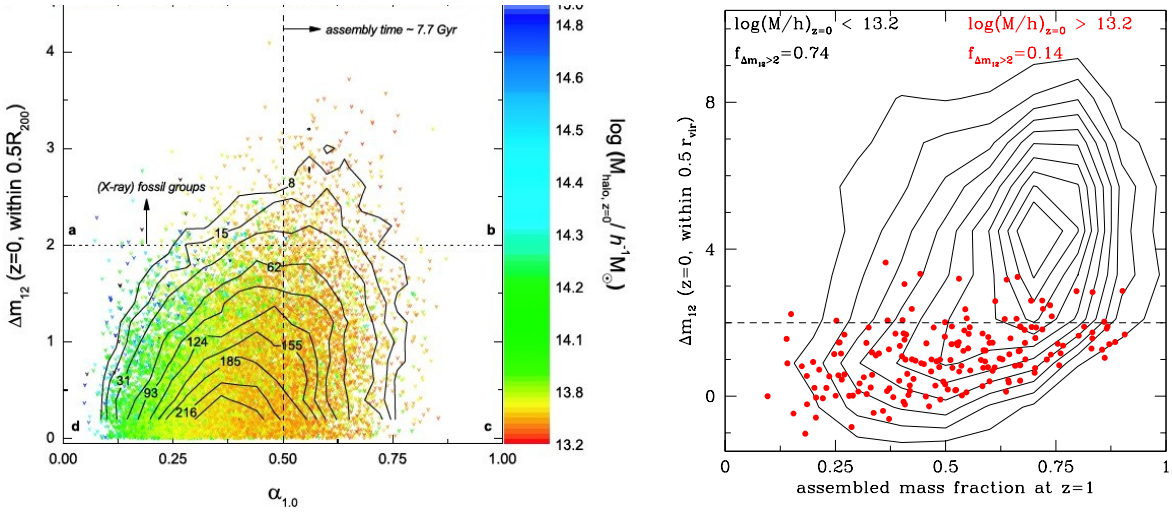

(a) Dariush *et al.* (2010) (b) this work

Figure 26: Magnitude gap m_{12} between the first and second ranked galaxy within $0.5\,r_{vir}$ at $z = 0$ versus the ratio of the virial mass at $z = 1$ to the mass at $z = 0$. (a) X-Ray bright clusters (fulfilling the L_X criterion for FGs) from the Millennium Gas Simulations. Basically, all data points belong to clusters with masses $\log(M_{vir}/h^{-1}M_\odot) > 13.2$. Cluster masses are color coded from low-mass to high-mass, red through blue, respectively. The horizontal dotted line marks the transition between fossil and non-fossil clusters. Clusters have typically $\Delta m_{12} < 2$ and the major fraction of clusters assemble the majority of their mass after $z = 1$ (vertical dashed line), with low-mass clusters tending to assemble their mass earlier. (b) Similar plot based on the G11 model, except color coding. Black contours (determined in squares of 0.1×1.2 in levels in factors of 15) illustrate the distribution of the low-mass regime – basically groups, while red data points belong the 180 clusters. The cluster distribution is comparable to that of D10, although negative magnitude gaps occur. Low mass systems show significantly higher Δm_{12} and typically assembled 70% of their mass before $z = 1$. Using the Δm_{12} criterion, an overwhelming majority of low mass systems in the G11 SAM is fossil, also by means of the assembly time. Note the different scalings for Δm_{12} in (a) and (b).

$\Delta m_{12} > 2$ as compared to the most massive clusters in the study of D10. However, it is clearly seen in Fig. 26a that the overwhelming majority of clusters is non-fossil.

The same analysis in the G11 model is presented in Fig. 26b. There is general agreement with the investigation of D10. The majority of clusters (red data points) have $\Delta m_{12} < 2$, 14% could be labeled (optical) "fossil" when the magnitude gap criterion is applied. The median assembled mass fraction is ~ 0.6, in qualitative congruence with the low-mass systems of Fig. 26a (70% of our clusters have masses $\log(M_{vir}/h^{-1}M_\odot) < 13.6$). The low-mass halo sample (black contours) continues the trend when compared to the high-mass sample in the following sense: the lower the mass of a system the earlier it has formed the majority of its final mass and the higher its magnitude gap. 74% of all low-mass systems ($\log(M_{vir}/h^{-1}M_\odot) < 13.2$) are optically "fossil" with magnitude gaps up to $\Delta m_{12} \sim 10$. The extreme behavior is not surprising as the fraction of solely optically determined fossils is known to increase with decreasing mass (see Cui *et al.* 2011 and references therein). Most notably, low-mass systems seem to prefer to have assembled $\sim 70\%$ of their final mass at $z = 1$ as it visible from the increasing density of the contours. However, it is also evident from Fig. 26b that basically the whole parameter space is available to low-mass systems.

But there are also differences between both plots. By our definition of Δm_{12} we allow negative values. This is apparently not the case in the analysis of D10. They mention that their Δm_{12} is the gap between the first and the second ranked galaxy in the system, i.e., the central galaxy has not necessarily been taken into account. However, only 5% of low-mass systems have a

negative magnitude gap and 10% of the clusters. We could have treated the magnitude gap accordingly by flipping all negative values but it illustrates another difference between both plots. The low-end of our Δm_{12} distribution correlates with the fraction of assembled mass at $z = 1$. It seems a consequence of the above mentioned trend that earlier assembled systems have on average higher magnitude gaps.

The trend is even stronger for low-mass systems. The above mentioned flipping of negative magnitude gaps can wash out this trend at least for systems that have assembled more than $\sim 60\%$ of their masses before $z = 1$. In fact, this behavior could indicate an evolution process, which argues in favor of FGs such as fossil means "majority of mass early assembled". Other explanations are plausible as well, e.g., that this regime is dominated by field galaxies which have only few (and much fainter) companions. Furthermore, we have to keep in mind that this plot is "constructed" as it considers only galaxies that reside within half the virial radius. The plot does not provide an information about the general magnitude gap in groups. In the outskirts, another bright galaxy may reside but not within half r_{vir}. However, the correlation among groups found in Fig. 26b is not obvious in Fig. 26a.

Another point worth mentioning is that some systems loose mass since $z = 1$, particularly in the low-mass regime. These systems are not shown in Fig. 26b and would be located at assembled mass fractions > 1. However, they are so sparse that no contour does appear. On the other hand, without exception, clusters in the G11 model gain masses if comparing the $z = 0$ snapshot with that one at $z = 1$, in qualitative agreement with Fig. 26a.

In Fig. 27, the sample is divided in four virial mass ranges (vertical lines) in order to investigate the mass dependence of the parameters of Fig. 26a. The plots contain a fossil sample (red data points) and a non-fossil sample (back data points), with the transition $\Delta m_{12} = 2$. Because the distributions are not Gaussian (it is rather a tail of a Gaussian distribution), only the inner two quartiles of each distribution is displayed by lines. The intersection of these lines denote the location of the median of a distribution. It is evident in the figure that the masses of fossil systems are on average smaller than those of non-fossils as red data points are offset from black data points to the left, except, in the most massive bin.

The bottom panel illustrates the magnitude gap distribution (Δm_{12}). Low-mass fossils have significant higher magnitude gaps in comparison to high-mass fossils. Non-fossils do not show any trend in this plot, their median is ~ 1 within every mass bin. The top panel shows the assembled mass fraction at $z = 1$ as compared to $z = 0$, the same parameter as in Fig. 26. It is obvious in the plot that fossils have assembled a higher fraction ($\sim 70\%$) of their final mass at $z = 1$ as compared to non-fossils ($\sim 50\%$). There is a weak mass dependence in fossil systems but the assembled fraction of the most massive non-fossils drops significantly ($\sim 35\%$). This is in agreement with the study of D10. In Fig. 26a the most massive systems (bluish) have smaller assembled fractions.

In the density panel of Fig. 27 we compute[2] the local average mass density of the systems at $z = 0$ when including all masses[3] within a sphere of $5h^{-1}$Mpc radius. For supercluster volumes this radius has been found to be a constant in the MS (see Einasto *et al.* 2007, and Liivamägi *et al.* 2012 for a different approach to the diameter). The plot shows the expected mass dependence. The more massive a system the denser its environment. Interestingly, there

2 The estimation has to be done with caution because those huge volumes can overlap with the bounding surface of the periodic MS-II cube. Therefore, a simple query within a sphere delivers wrong numbers. One fourth of all systems is affected by this issue when estimating the mass density.

3 We think that mass density is a better tracer for environment since gravitation accelerates all systems, increasing velocities and therefore increasing the probability for encounters.

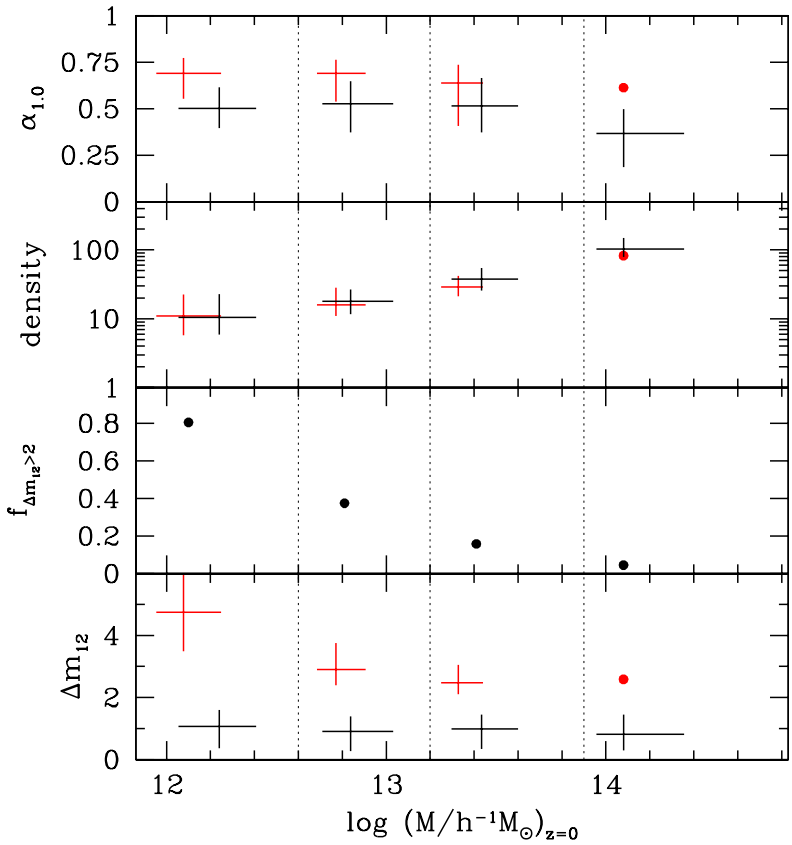

Figure 27: Mass dependence of fossil ($\Delta m_{12} > 2$, red data points) and non-fossil systems ($\Delta m_{12} < 2$, black data points). The samples were subdivided in four mass ranges as indicated by the vertical dotted lines. Shown are the inner two quartiles of each distribution. The center of the crosses denotes the location of the medians. Panels in top to bottom order. (1) Fraction of final assembled mass at $z = 1$ (see Fig. 26). (2) Local density within a sphere of radius $5h^{-1}$Mpc, normalized to the lowest density found among all groups and clusters. (3) Fraction of fossils within the mass bin. (4) Magnitude gap distribution. The most massive mass range contains only one fossil system, displayed by the red dot.

is no or very small difference between fossils and non-fossil. From a statistical perspective both types reside in similar environments.

The remaining $f_{\Delta m_{12}} > 2$ panel represents the fraction of fossil system within each mass bin. It shows that the fraction of (by the magnitude gap) identified fossils increases continuously with decreasing virial mass as already suspected from Fig. 26a. This is in agreement with both observational and semi-analytical studies which consistently claimed the mass dependence of the optical fossil fraction (Milosavljević *et al.* 2006; D'Onghia *et al.* 2007; van den Bosch *et al.* 2007; Yang *et al.* 2008; Dariush *et al.* 2010). On the other hand, there is inconsistency about the actual value of the fraction (10 ~ 60% for masses ~ $10^{13}M_\odot$.). We find even 80% in the lowest mass bin to be "optical" fossils. Using the GIMIC simulations (utilizing the MS), Cui *et al.* (2011) have shown that it is necessary to invoke the X-ray luminosity to shrink the optical fossil fraction from 70% to a X-ray matched fraction of ~ 10%. X-ray data is not available for the G11 SAM. Therefore, we will use a different approach to account for the hot gas emission as outlined in the following section.

8.3 FINDING ELLIPTICAL GALAXIES

In this section we want to investigate the properties of the central group/cluster galaxies in order to find fossil groups in our sample. This addresses photometric properties but also star formation and merger histories. Beside the identification of systems which should be X-ray bright, the aim is to find central galaxies to be identified with ellipticals. The latter is the third and obvious selection criterion of FGs.

8.3.1 *Ellipticals as passive galaxies*

Elliptical galaxies are known to be non-star forming. Hence their light is dominated by old stars, which let an elliptical appear red. We recall from the previous chapter that in the G11 model star formation is driven by either disk instabilities or merger events. Galaxies become passive/non-star forming if the merger event is strong enough to expel the cold gas from the disk to the hot gas reservoir.

Photometric properties. A first approach is to investigate the dependence between star formation and color, illustrated in Fig. 28 where star formation rate (SFR) versus $u-r$ color of central galaxies is plotted. Red data points represent central galaxies of clusters and black contours belong to central galaxies of groups with masses lower than $\log(M_{vir}/h^{-1}M_{\odot}) = 13.2$. There are 26 clusters in the SAM exhibiting the FG magnitude gap larger than 2 mag within half the virial radius. Those clusters are divided into "candidate" and "true" FGs and marked with green and blue crosses, respectively. A true fossil is a massive cluster one expects to have a sufficient bright FG X-Ray luminosity as outlined in Sect. 8.1.

As expected from the stellar population model, group centrals occupy two regions in the plot. There are red and passive galaxies but there is also a significant number of blue and star-forming centrals, if we consider the notations "blue" as $u-r < 2$ mag and "star-forming" as $SFR \geqslant 1\, M_{\odot}yr^{-1}$. The latter is the commonly referred to the SFR of normal spiral galaxies (Lee *et al.* 2009).

The identification of active galaxies being blue holds not for cluster centrals. Star-forming central galaxies of clusters remain red, although the scatter increases towards more bluish colors. In particular, it turns out that even central galaxies of fossil clusters can be star forming. This behavior can be explained by their lower specific SFR (per unit stellar mass, SSFR hereafter) as displayed in Fig 29. Star forming central galaxies of clusters have on average a factor of ten higher stellar masses as compared to those of the groups. The same amount of new born stars contributes a smaller fraction to the total light in the case of cluster centrals, i.e., the light remains dominated by older, red stars so that their SSFR is small compared to actively star-forming spiral galaxies. Again, typical values for normal spiral galaxies are $SSFR \geqslant 10^{-11}yr^{-1}$ (Lee *et al.* 2009), denoted by the horizontal dotted line. Fig. 29 shows that the two classes of central galaxies (star forming and passive) in groups remain intact. On the other side, even the central galaxies of fossil clusters can be actively star forming in the SAM of G11 although they are red. However, we are interested in ellipticals which are known to be passive galaxies. Fig. 29 therefore suggests that $SSFR \leqslant 10^{-11}yr^{-1}$ is also reasonable in the G11 model in order to distinguish passive from star forming galaxies.

Another interesting point regards the luminosities of fossil cluster centrals. They are generally brighter than $M_r = -22$ mag. This is in agreement with the observational studies of Zarattini *et al.* (2014) and Santos *et al.* (2007) who find only 1 out of 25 (1 of 34, respectively) fossil clusters whose central galaxy is fainter than that. We use this finding in the following as

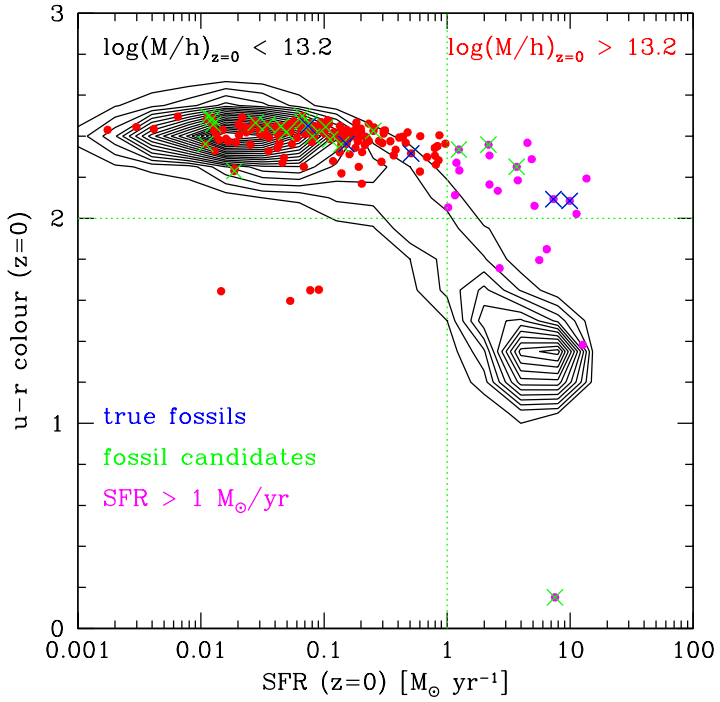

Figure 28: $u-r$ over SFR of central galaxies in the SAM of G11. Shown are only galaxies with SFR > 0 at $z = 0$. Red dots represent the central galaxies of clusters ($\log(M_{vir}/h^{-1}M_\odot) \geqslant 13.2$). Purple data points belong to those clusters with SFR $\geqslant 1\,M_\odot$/yr. Blue crosses represent clusters which fulfill $\Delta m_{12} > 2$ and have masses $\log(M_{vir}/h^{-1}M_\odot) \geqslant 13.5$, i.e., they would certainly be bright enough in the X-ray to qualify them as FG according to D10 (see Sect. 8.1). Similarly, green crosses are the less massive clusters which fulfill the magnitude gap of fossil groups. Black contours belong to the data from groups with masses $\log(M_{vir}/h^{-1}M_\odot) < 13.2$. The green dashed lines represent the divisions between blue and red, and star forming and passive, respectively. In groups, blue central galaxies are star forming. In contrast, star forming cluster centrals are significantly redder, likewise the fossil clusters.

constraint for centrals galaxies of fossil groups.

Star formation histories. What are typical SFRs of elliptical galaxies in the G11 model? Since elliptical galaxies are formed by mergers, we compare the star formation history (SFH) of central galaxies to their merger history in order to figure out what level of SFR can be expected for an elliptical galaxy.

For the last 7.6 Gyr ($z = 1$) this analysis is shown for 16 examples from group mass scale through cluster scale in Fig. 30 for a "fossil sample" with $\Delta m_{12} > 2$ and in Fig. 31 for a "control sample" which obeys $|\Delta m_{12}| < 0.5$. In each subfigure (of similar mass) the histories of two central galaxies are plotted. Denoted in blue is a galaxy that has SFR > 1 at $z = 0$, while black lines/symbols belong to a galaxy with SFR < 1 at $z = 0$. The top panel of each subfigure shows the SFH of the central galaxy (by means of SSFR) and the bottom panel illustrates its merger history.

A merger event was considered to take place one snapshot after the `mergeon` flag of an infalling galaxy was set to either 2 (merging galaxy is type 2) or 3 (merging galaxy is type 1), and its descendant was the central cluster/group galaxy. According to G11 we define major mergers (baryonic[4] mass ratio larger than 1:3) and minor mergers (mass ratio between 1:3 and 1:10). We also consider mergers that have not been significant (masses differ by more than a factor of 10). These three regimes are separated by horizontal dotted lines in bottom panel of each subfigure.

Both figures show clearly that mergers trigger star formation, as described in Guo *et al.* (2011). The SSFR peak remains for one snapshot only (roughly 0.3 Gyr) and can reach a level similar to that of spiral galaxies (dotted line) regardless of the type of merger. Even a non-significant merger in the most massive groups can trigger a spiral-like SSFR.

4 We take only stellar mass and cold gas mass into account to determine the merger mass ratio as we have found only those masses are relevant to destroy a disk in agreement with the G11 definition of a major merger. The hot gas halo attached to a galaxy is apparently neglected in this calculation, although Guo *et al.* (2011) write: "Major mergers are those between galaxies with *baryonic* masses differing by less than a factor of 3."

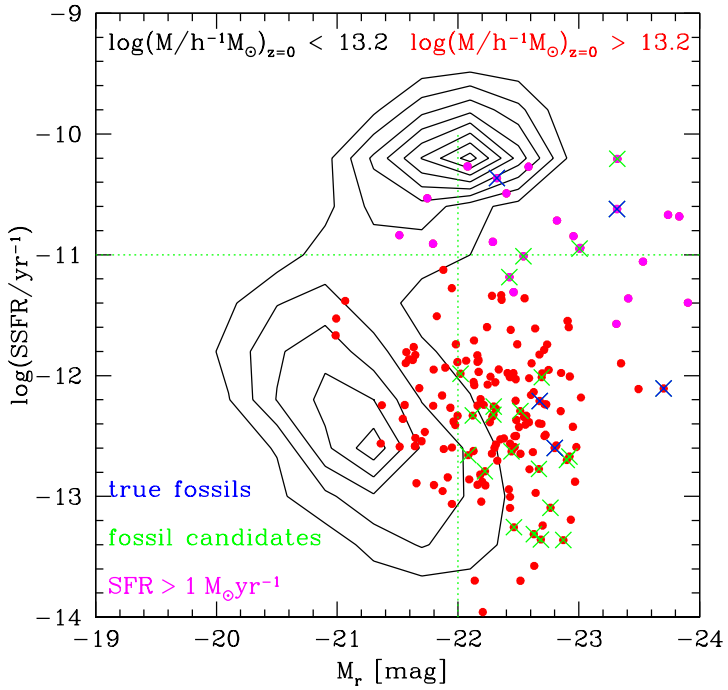

Figure 29: SSFR versus M_r of central galaxies with SSFR > 0. Labels as in Fig. 28. Black contours on a grid of 0.4×0.4 mag with contour level 20. Within the cluster sample, FGs and possible FGs occupy only total magnitudes brighter than $M_r \leqslant -22$ mag and are most likely passive with SSFR $\leqslant 10^{-11}$, emphasized by the green dashed lines.

The low mass groups in the top left panels of figures show that it is possible to have a SSFR $> 10^{-11}\mathrm{yr}^{-1}$ without a merger event. We note that roughly half of all groups with $\Delta m_{12} > 2$ containing a bright central galaxy ($M_r < -22$ mag) have such high SSFRs. When (presumably) the first merger occurs the SFR of such a system is quenched as evident in the top left panel of Fig. 30 (black line). The time scale of this quenching process, however, seems to depend on the mass ratio of the merger.

The prescription of G11 converts a certain percentage of cold gas in the disk of a galaxy into stars each snapshot. This fairly constant (high) SSFR in the low mass centrals, which have not been disturbed by a merger, belongs to star formation by disk instability. As soon as a merger occurs, a fraction of the cold gas is converted into stars and the remaining cold gas is either completely expelled (major merger) or a part of it remains in the surviving disc (minor/non-significant merger) (Guo *et al.* 2011).

There are two points to make about these these figures. First, there is no difference between the fossil sample and the control sample. The star formation history (SFH) is similar with respect to merger events. Likewise, the frequency of mergers does not differ significantly either, when comparing systems of equal mass. Second, SSFR $> 10^{-11}$ most likely seems to indicate an ongoing merger event in clusters. At the group mass scale, SSFR $> 10^{-11}$ in the central galaxy can also mean, that it has never experienced a merger. Thus, defining fossil groups by only the magnitude criterion and "not having experienced a merger since $z = 1$" introduces a bias because the majority of these "fossils" are star forming. In the G11 model it seems that these star forming central galaxies are comparable to field galaxies or groups like the Local Group[5]. We will return to this topic in Sect. 9.2.

However, a general SSFR level for passive galaxies is not easy to define from the small number of investigated galaxies in Figs. 30 and 31. We therefore investigate the merger history of central galaxies of central galaxies in the group mass regime since $z = 1$, which is presented

5 The Local Group fits indeed the adopted mass range as it has a total mass of $M_{tot} \sim 1.3 \times 10^{12} M_\odot$ (Karachentsev & Kashibadze 2006).

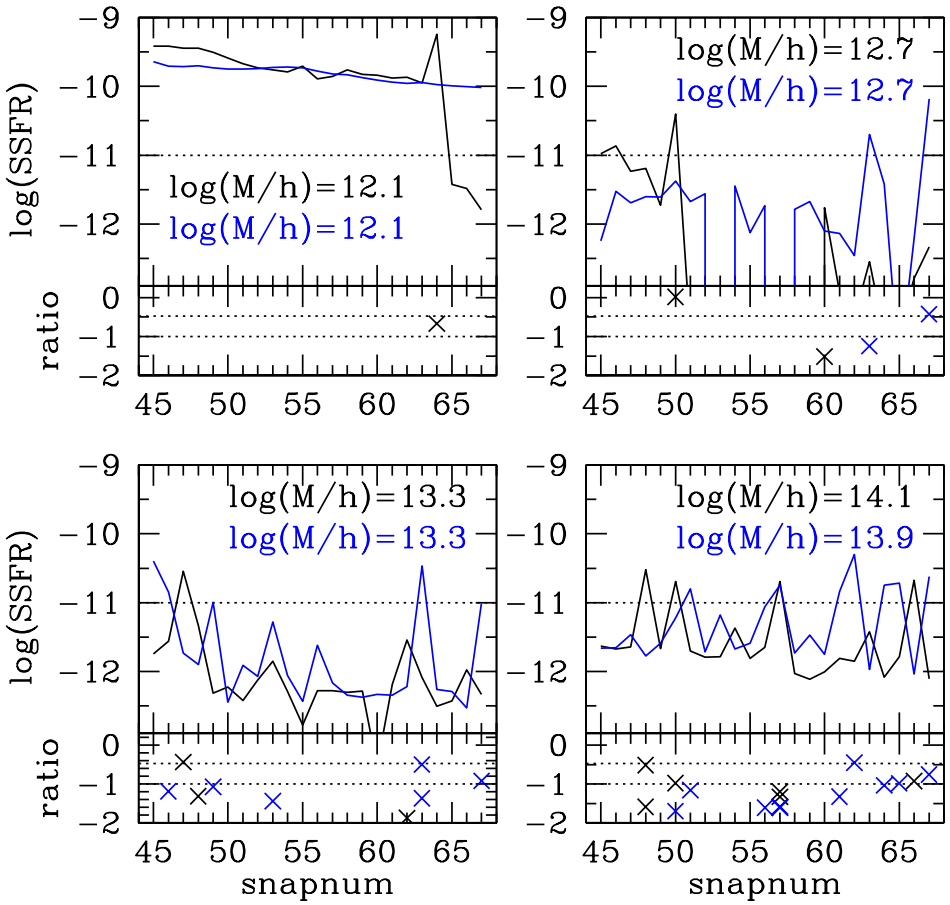

Figure 30: The effect of mergers on the SSFR in central galaxies of groups/cluster with $\Delta m_{12} > 2$. Subfigures correspond to virial masses as indicated, equally spaced in log space. The top panel in each subfigure shows the SFH of a central galaxy. Snapnum is the snapshot number (see Tab. 7), SSFR in units of yr^{-1}. SSFR $> 10^{-11}$ is typical for spiral galaxies and indicated by the dotted line. The bottom panel of a subfigure shows baryonic mass ratio of the merging galaxies in logscale. The space between both dotted lines in this plot denotes the ratio range of minor mergers. Above 1:3 (~ -0.5 in logspace) a merger event is a major merger. Below 1:10 ($= -1$ in logspace) a merger event is "not significant". Blue data points and lines belong to a central galaxy with SFR > 1 at $z = 0$, a central galaxy with SFR < 1 at $z = 0$ is indicated in black. Clearly, SFR peaks in central galaxies are related to mergers.

in Fig. 32 for systems with $\Delta m_{12} > 2$ mag. Plotted is the SSFR at present time ($z = 0$) with respect to the lookback time since the last merger involving the central galaxy has happened. Central galaxies whose last merger event was a major merger belong to red data points, minor mergers are represented by green data points, and if the last merger was non-significant it is denoted by blue data points.

If a merger is ongoing (at $z = 0$) Fig. 32 shows clearly that the SSFR is basically comparable to that of spiral galaxies (above the dashed line). It is also evident in the plot that major mergers quench star formation to a level lower than $SSFR = 10^{12} yr^{-1}$. On the other side, non-significant mergers do not affect the SSFR of central galaxies. These galaxies have generally SSFR on the same level, which is similar to spiral galaxies. This suggests that these galaxies have not experienced any other significant merger event in the past. Minor mergers, in turn, inhibit star formation significantly to a level of $-12 \leqslant \log(SSFR/yr^{-1}) \leqslant -11$, unless the merger took not

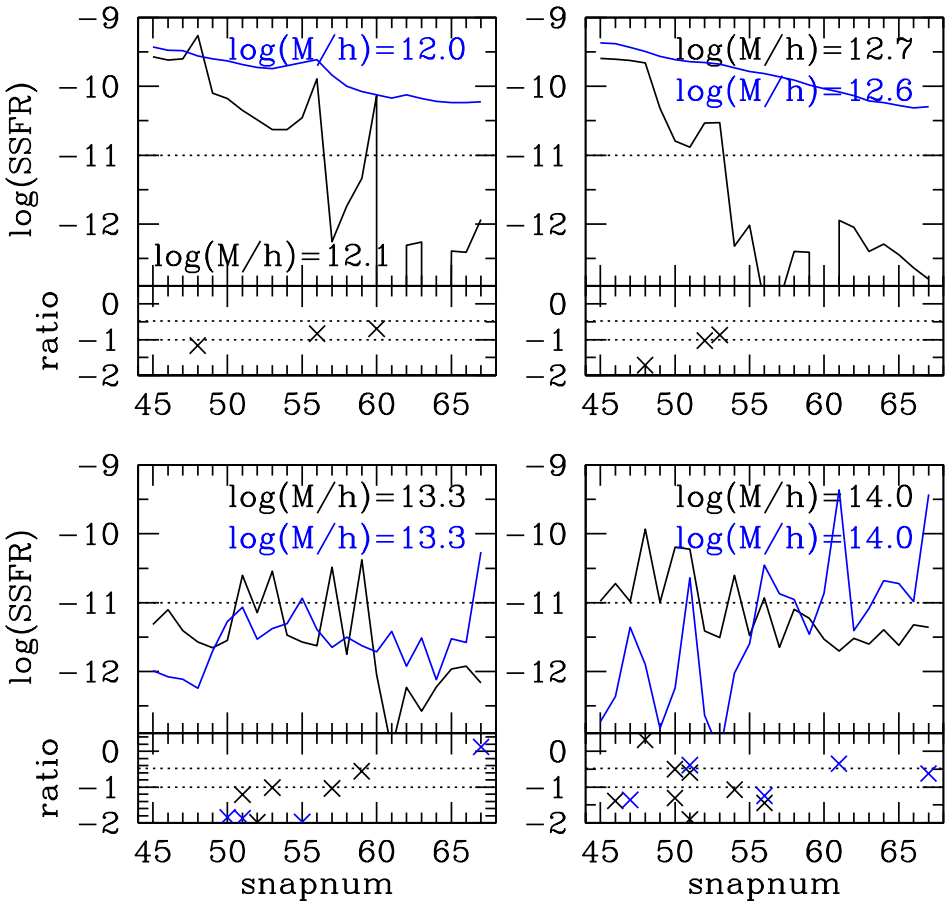

Figure 31: Same as Fig. 30 but for groups/clusters with $\Delta m_{12} < 0.5$ (control sample).

place during the last 1 Gyr. This suggests that minor mergers inhibit star formation on larger time scales.

Unless there is no ongoing merger event, the SSFR certainly drops below $10^{-11}\mathrm{yr}^{-1}$ if a minor or major merger took place in past. However, Figs. 30 and 31 suggests that central galaxies in the cluster regime tend to have $-12 \leqslant \log(\mathrm{SSFR}/\mathrm{yr}^{-1}) \leqslant -11$. This is also supported by Harrison *et al.* (2012) who find BCGs of fossil clusters to have SSFR up to $10^{-11}\mathrm{yr}^{-1}$. In the group mass regime of Fig. 32 a level is not clearly seen either. We thus can not constrain the SSFR of passive galaxies further and remain with condition that elliptical galaxies must have $\mathrm{SSFR} < 10^{11}\mathrm{yr}^{-1}$, which basically means that the central galaxy has undergone a merger in the past.

8.3.2 *Ellipticals as bulge-dominated systems*

The other approach to obtain elliptical galaxies is to search for galaxies whose disk has been destroyed. In the G11 model, this is achieved by major mergers, i.e., mergers with baryonic mass ratios larger than 1:3. G11 calculate the bulge-to-total (B/T) stellar mass ratios of the galaxies and adopt $\mathrm{B/T} > 0.7$ to be ellipticals. In Fig. 33 the distribution of the B/T ratios of 3681 central galaxies of most massive groups/clusters is illustrated. It is surprisingly not a smooth distribution. Basically, no central galaxy with $0.5 \leqslant \mathrm{B/T} \leqslant 0.9$ is found, in contrast

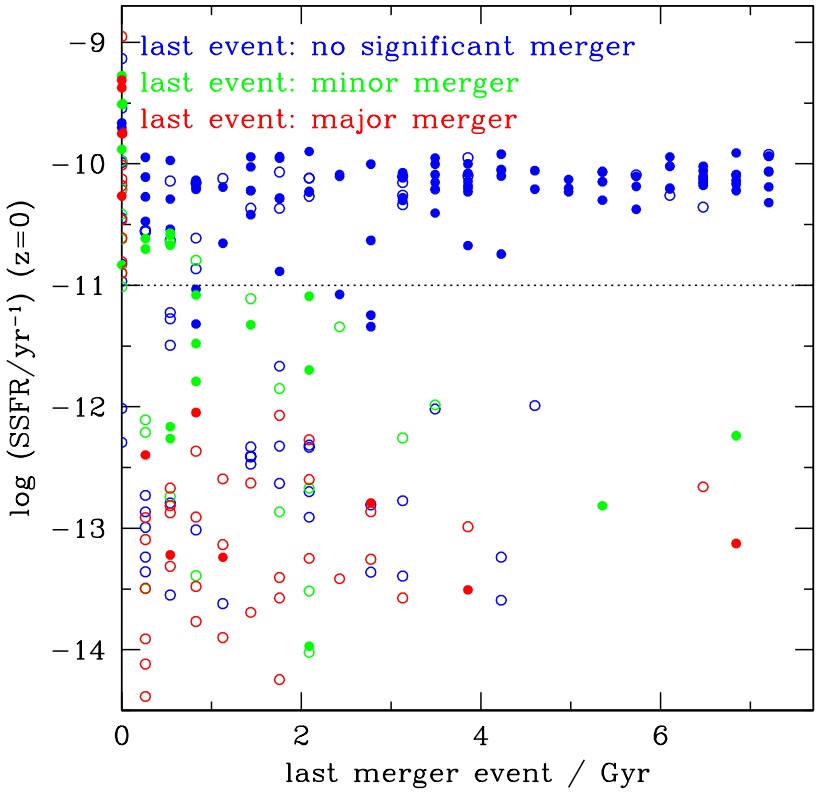

Figure 32: Specific star formation rate at $z = 0$ vs. lookback time of the last merger involving the central galaxy. Plotted are only groups with $10^{12} \leqslant M_{vir}/h^{-1}M_{\odot} \leqslant 10^{13}$, $\Delta m_{12} > 2$ mag and SFR $> 0\,M_{\odot}yr^{-1}$, which have had at least one merger event with a galaxy brighter than $M_r = -16$ mag since $z = 1$. While major mergers are those between galaxies with stellar and cold gas mass differing by less than a factor of 3, a non-significant merger is characterized by mass ratios smaller than 1:10. Minor mergers have mass ratios between those limits. Red, green and blue data points represent merger events as indicated in the diagram. Solid symbols denote central galaxies that have experienced only one merger during the last ~ 7.7 Gyrs, while open symbols show galaxies with more than one recorded merger since $z = 1$. If a central galaxy experiences a major merger, the SSFR at $z = 0$ is below $10^{-12}yr-1$ unless the merger is not ongoing. Minor mergers quench star formation although less strong. On the other side, if there was only one non-significant merger in the past since $z = 1$ star formation is not quenched, i.e., the SSFR is generally higher than $10^{-11}yr^{-1}$. The horizontal line denotes the approximate limit of SSFR in spiral galaxies (Lee *et al.* 2009).

to observations. We therefore refrain from adopting B/T values and focus on the definition of passive galaxies as ellipticals, outlined in the previous section.

8.4 FOSSIL GROUPS AS RELAXED SYSTEMS

Fossil groups are considered to be relaxed as they are dominated by an elliptical galaxy, which was once formed by a major merger, but obviously not in interaction with another galaxy anymore. The timescales for obvious strong visual features of mergers range from ~ 0.2 Gyrs for dry mergers (Bell *et al.* 2003) up to ~ 0.8 Gyrs for major mergers of gas-rich disk galaxies (Lotz *et al.* 2008; Bridge *et al.* 2010). In order to account for this morphological criterion, we consider groups as potential fossil candidates only if their last merger event (major, minor or non-significant) happened at least 1 Gyr in the past.

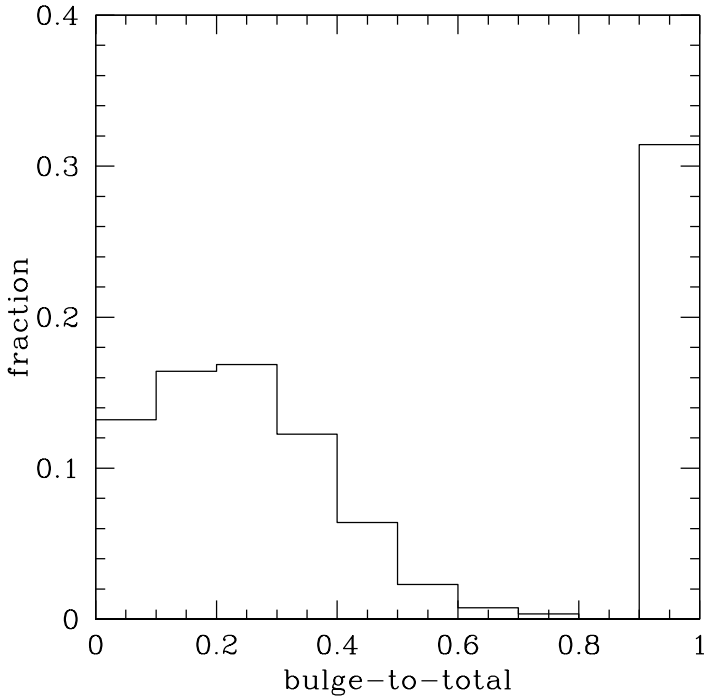

Figure 33: Bulge-to-total ratios of all central galaxies of groups/clusters with virial masses larger than $M_{vir} = 10^{12} M_{\odot}$. The G11 model provides a bimodality as bulge-dominated galaxies are clearly distinct from disk-dominated galaxies.

8.5 SUMMARY OF SELECTION CRITERIA

Here we summarize the criteria which have been applied to the central galaxies of clusters and groups contained in the SAM of Guo *et al.* (2011) at $z = 0$ to obtain fossil groups and clusters.

1. $M_r < -22$ mag because no fossil cluster was found with central galaxies fainter than that. In addition X-ray luminosity scales with optical luminosity. Optically bright (elliptical) galaxies are accompanied by a bright X-ray halo (Cox *et al.* 2006; Harrison *et al.* 2012; Girardi *et al.* 2014).

2. $\Delta m_{12} > 2$ within $0.5\, r_{vir}$, the magnitude gap criterion for fossil groups.

3. SSFR $\leqslant 10^{-11} yr^{-1}$ to account for a passive (elliptical) galaxies and to reject spiral-like galaxies.

4. The last merger involving the central group/cluster galaxy happened at least 1 Gyr in the past to account for relaxed systems and to avoid visual merger features, which could still be visible in the observed counterparts.

The selection criteria and the resulting samples are summarized in Tab. 5.

Table 5: Rejections due to selection criteria for different samples.

Criterion	Clusters		Groups		
	180		3154		
	fossil	control	fossil	field	control
magnitude gap	26	44	2415		175
luminosity	26		455		
star formation	20	41	100	355	150
relaxed systems	12	29	59	298	141

Notes. Selection criteria originate in findings of Figs. 29 and 32. The group mass range is $10^{12} \leqslant M_{vir}/M_{\odot} \leqslant 10^{13}$ and clusters have masses $\log(M_{vir}/h^{-1}M_{\odot}) \geqslant 13.2$. Within $0.5r_{vir}$, a magnitude gap of $\Delta m_{12} \geqslant 2$ mag is adopted for fossil and field groups, $|\Delta m_{12}| \leqslant 0.5$ mag for control samples. A luminosity cut-off is not imposed on the control samples but for fossils it is $M_r < -22$ mag. $\log(SSFR/yr^{-1}) < -11$ is adopted for fossil and control groups, while $\log(SSFR/yr^{-1}) > -11$ is the condition for field groups. Relaxed systems are mimicked by the adoption that the last merger involving the central galaxy happened at least 1 Gyr in the past.

9

HISTORY AND PROPERTIES OF FOSSIL SYSTEMS

In this chapter we want to analyze fossil systems and compare these to non-fossil groups which are referred to as control sample. In literature control samples often have $\Delta m_{12} < 0.5$ mag (e.g., Dariush *et al.* 2010; Díaz-Giménez *et al.* 2011). Owing to our definition of Δm_{12} in Sect. 8.2, negative values are allowed as well. Thus, we will define a control group/cluster as $-0.5 \leqslant \Delta m_{12} \leqslant 0.5$ mag. Except the luminosity constraint which is put on the fossils, the control samples have been selected in a similar manner (see Tab. 5). We have already made use of this notation in Sect. 8.3.1.

9.1 FOSSIL CLUSTERS

In the previous chapter some constraints were imposed on the centrals galaxies in order get a tighter sample of ellipticals. In this section we aim at examining global properties for the cluster mass regime, i.e., $\log(M_{vir}/h^{-1}M_{\odot}) \geqslant 13.2$. Four parameters are investigated for a fossil and a control sample, as they were defined in the previous chapter (see Tab. 5). In Fig. 34 the analysis of the mass distribution, local densities, the distribution of the central's luminosities and the B/T ratios are presented. In each panel the fossil sample is displayed in red and the control sample in black. Both the control and the fossil sample contain systems of which we believe an undisturbed elliptical resides in the center.

It has to be stressed at this point that we are facing low number statistics in the cluster regime (see Tab. 5) as the fossil sample contains only 12 clusters and the control sample consists of 29 clusters. The findings presented here must be seen in this light.

9.1.1 *Properties*

The mass distributions in the top left panel of Fig. 34 shows the employed cut-off at the low-mass end. A first difference between both samples is revealed. While the fossil sample has a narrow (low-)mass range, the control sample contains clusters which are on average more massive. In the top right panel of Fig. 34 the average local mass density is computed as already done in Sect. 8.2. The different mass distributions do also manifest in different density distributions. The distributions look similar but shifted to each other. Fossils tend to reside in lower density regions. The median overdensity of the fossil sample is ~ 23, while the value is roughly a factor of 1.5 larger for the control clusters.

The bottom panels of Fig. 34 illustrates properties of the central galaxies. Control centrals are fainter than their fossil counterparts, being on average ~ 0.3 mag brighter. Note, that the fossils BCGs are generally brighter than $M_r = -22$ mag (see Fig. 29) and no artificial cut-off is introduced in this plot. The B/T ratios of both fossil and control cluster centrals converge to 1 which indicates that the majority of those galaxies have experienced a major merger (or

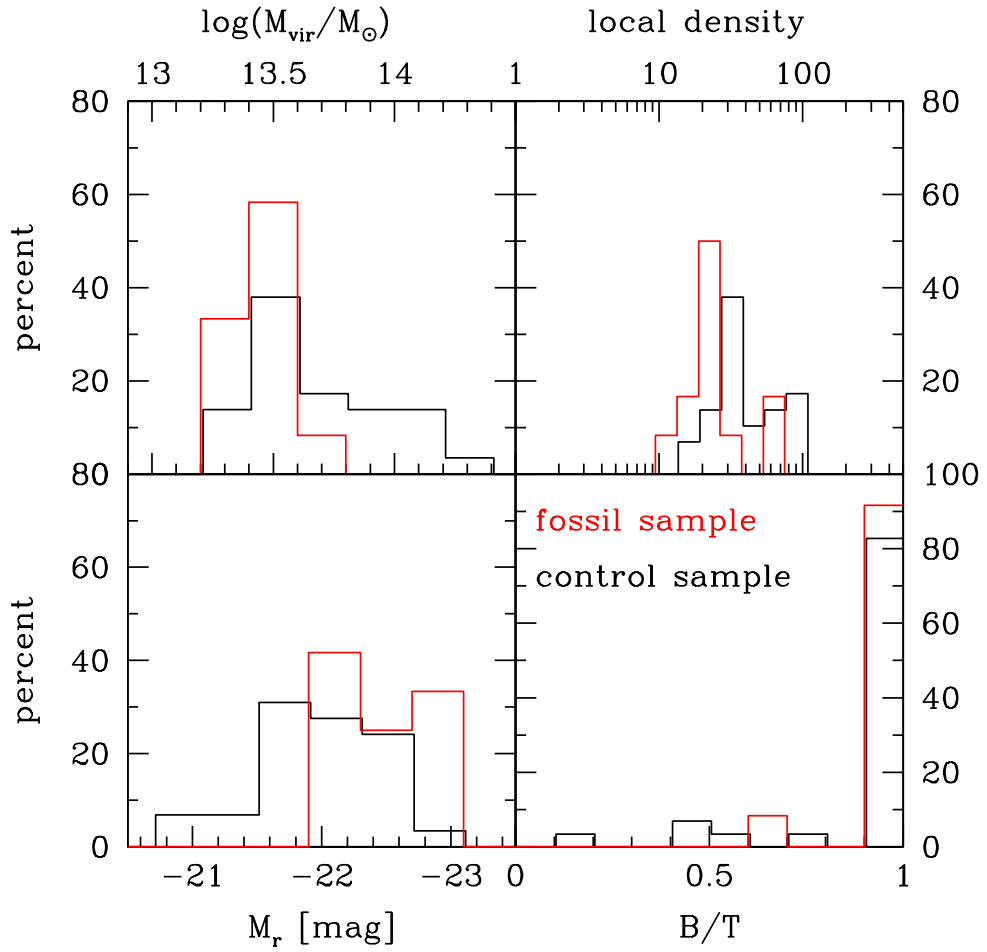

Figure 34: Properties of clusters with masses $\log(M_{vir}/h) \geqslant 13.2$ at $z = 0$. Top left panel: mass distribution of the virial masses. Top right panel: distribution of the local environment as mass density within a surrounding sphere of $5h^{-1}$Mpc radius (see text). Bottom left panel: r band luminosity distribution of the central galaxy. Bottom right panel: B/T ratio distribution of the central galaxy. Red data belong to the fossil cluster sample and black data represent the control sample. Fossil clusters have lower masses and reside in less dense environments. While their BCGs are brighter than those of control clusters, both types are ellipticals.

repeated minor mergers) such that the G11 model considers the disk of those systems to be non-existent, i.e., they are ellipticals at present time. On the other hand, this result is not surprising since only 13 out of 180 cluster centrals are not ellipticals when considering $B/T = 0.7$ as transition to disk galaxies.

9.1.2 *The fossil phase*

As pointed out in Sect.1.5, simulations revealed that fossil groups are merely a phase in the evolution of galaxy groups and clusters (e.g., von Benda-Beckmann *et al.* 2008). It is a basic intention of this thesis to address this finding. D10 emphasize this as they find only very few clusters that remain fossil after 7.6 Gyrs, or in return, fossils we see today were not fossils at $z = 1$. In Fig.35 we present the same analysis. In order to be comparable, we choose the magnitude gap criterion only to define a fossil and a control cluster. The figure shows the same trend Dariush *et al.* (2010) found. After $\sim$ 7.6 Gyrs the majority of fossil systems is not fossil anymore. Similarly, a fossil cluster at $z = 0$ was unlikely fossil at $z = 1$. Control clusters behave

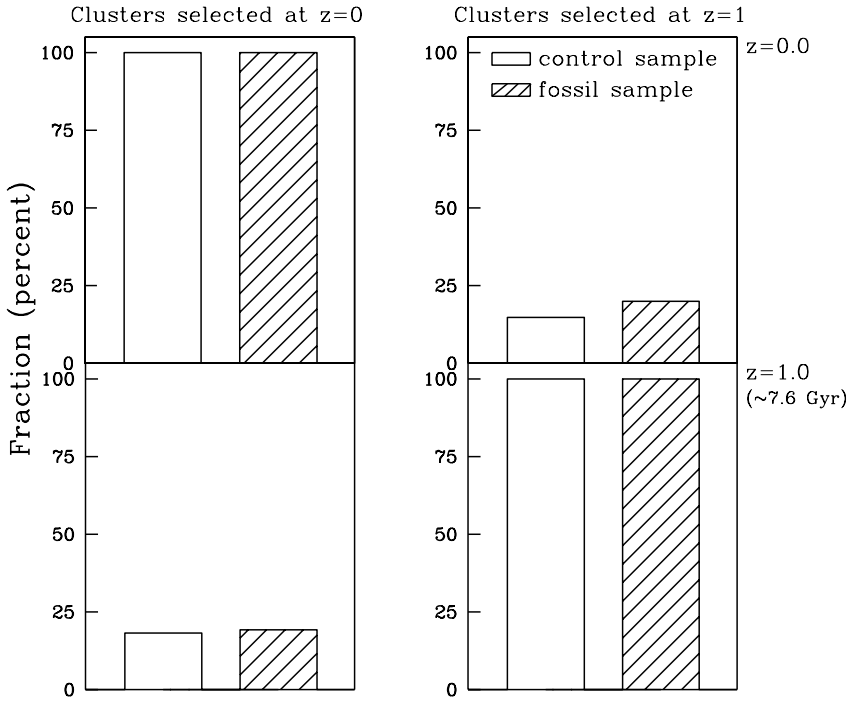

Figure 35: Evolution of fossil and control clusters (see text). We select control and fossil clusters at $z = 0$ (left column) and $z = 1$ (right column) and explore what fraction remains fossil or control at the other epoch. It is clear that the "fossil phase" does not last in 80% of all cases.

in the same fashion as they do not belong to the control sample anymore when looking back (or forward) in time.

While the relative numbers for the control sample ($\sim$ 15% remain in the control sample after 7.6 Gyrs) are in agreement with the D10 analysis of clusters, they are not in the case of fossil systems. In either case, about 20% of all fossil clusters remain fossil. This is a factor of $\sim$ 10 more than the fraction Dariush *et al.* (2010) found to remain fossil. It has to be noted again that the numbers have to be treated with care (5 of 25 remain fossil). Even the Poissionian error can push the fraction to the level of D10. Additionally, compared to their study we are biased towards low-mass systems within the cluster regime. As pointed out in Sect. 8.2, the fossil fraction increases with decreasing halo mass. However, the general message of the figure is that galaxy clusters in the G11 model evolve in terms of their magnitude gap.

9.1.3 *Progenitor halos*

Oser *et al.* (2010) showed in simulations that the stars in galaxies are formed within the galaxy during a phase of infalling gas before $z = 2$ which is followed by a phase of accretion of stars formed outside the virial radius, essentially in other galaxies. Inspired by their work we want to investigate whether differences exist between the formation of progenitor DM halos that eventually merge in the central DM halo among a fossil and a control cluster. In Fig. 36a such an analysis of progenitor halos as identified by `subfind` is presented for a fossil (red) and a control cluster (black) of similar mass ($\log(M_{vir}/h^{-1}M_{\odot}) \approx 13.6$) and environment. We plot the "formation" time (in terms of redshift) over the distance to the DM halo (in terms of factors of r_{vir}) that is considered to be the root of the central halo (bottom left panel).

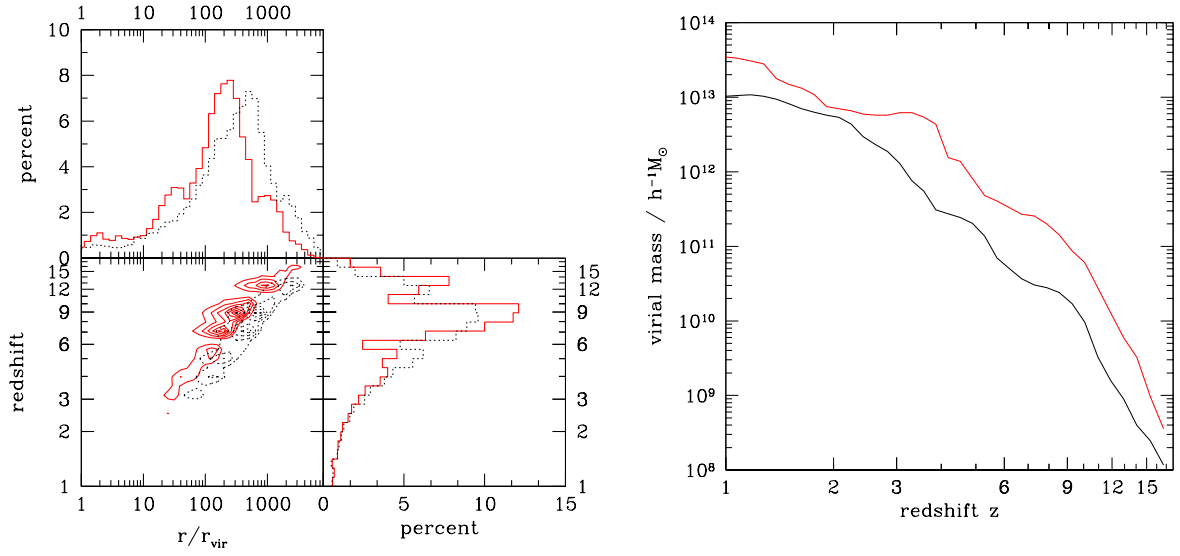

(a) mass origin

(b) mass assembly

Figure 36: Origin and assembly of mass for a fossil (red) and a control cluster (black) of comparable mass ($\log(M_{vir}/h^{-1}M_{\odot}) \approx 13.6$) and similar environment at $z = 0$. (a) Origin time (in redshift) and place (in terms of distance to the central halo) of all DM halos that eventually merge in the central DM halo of the cluster. The formation of the progenitor DM halos of a cluster is clumpy in space and time. The formation time distribution of both samples is comparable, while the progenitor halos of the control cluster form more distant as compared to the fossil. (b) Mass assembly of the same clusters with respect to redshift. Before $z = 3$ the fossil cluster is roughly an order of magnitude more massive than the control cluster.

There is a correlation in Fig. 36a between formation time of the progenitor halos and their distance to the central halo. The earlier a DM halo is formed the more distant from the central halo it happens. This is owing to our definition of distance to the central halo in terms of its virial radius. The higher the redshift the smaller the virial mass of the central halo (see Fig. 36b) and therefore the smaller its virial radius (see Eq. 5). Although the absolute distances in factors of h^{-1}Mpc may be similar, our relative defined distances must increase with redshift.

However, there is a shift between the distance distributions of both clusters (see top panel of Fig. 36a). The control cluster seems to be capable to accrete DM halos that have formed in greater distance, although its final mass is the same as that of the fossil cluster. To explain this behavior, Fig. 36b is needed. The fossil cluster (red) assembles more virial mass before $z \sim 3$, the period when almost all progenitor halos are formed. Before $z = 3$, the virial mass of the fossil cluster is almost an order of magnitude larger as compared to the control cluster. Hence, its virial radius is larger. This makes the fossil cluster assigning a smaller relative distance (in terms of r_{vir}) to an object located at the same physical distance as compared to the relative distance the control cluster assigns. This accounts for the shift in the formation distances distribution, which is ~ 3 as expected from Eq. 5.

Generally, the progenitor halos of the central cluster halos are equally distributed in time but the distribution is different in space with respect to the central halo. That the control cluster assembles its virial mass later than the fossil cluster suggests that the central halo originates from a less dens environment and needed thus more time to assemble its mass.

9.2 FOSSIL GROUPS

In order to compare our observationally obtained findings of NGC 6482 to the G11 model, we are particularly interested in properties of fossil groups in the group mass range. We have selected 59 FGs and 141 control groups as they are specified in Tab. 5. The central galaxy of the control sample has not a luminosity constraint but needs to be non star forming in order to compare it to the red FG sample. Additionally, we will investigate the star forming "fossils" whose centrals look like spiral galaxies, simply because we are curious about those. The star forming "fossil" sample is accordingly defined, except for their high SFR, and consists of 298 groups. While the representation of fossils (red) and controls (black) is adopted from the previous section in plots, the star forming "fossils" will be displayed in blue throughout this section.

9.2.1 *Properties*

In Fig. 37 the properties of the groups are presented similar to Fig. 34. The mass distributions in the top left panel provides first insights. Clearly seen is the adopted mass range for groups ($10^{12} \leqslant M_{vir}/M_{\odot} \leqslant 10^{13}$) which cuts the distributions on both edges. While the control sample shows a uniform mass distribution blue "fossil" and red FG distributions are very different from each other. The masses of the passive FGs are basically higher than $1.6 \times 10^{12} M_{\odot}$ and fairly uniformly distributed up to the cut-off at the high mass end. The mass distribution of the active "fossils" looks like the tail of a Gaussian distribution, cut at the low mass end. There is actually not a single star forming "fossil" more massive than $4.5 \times 10^{12} M_{\odot}$.

The local density distributions (see Sect. 8.2) in the top right panel of Fig. 37 show that environmental differences among the samples are not as strong as one would expect it from their mass distributions, although they exist. Again, the control sample and the red FGs have strikingly similar distributions. The median overdensity a group resides in is ~ 13 for the FG sample and ~ 14 in the case of the control sample. In contrast, the median local density a blue "fossil" resides in is ~ 10. Obviously, these "fossils" reside in on average lower density regions as compared to the other samples. This again indicates that we are facing a kind of "field groups". In addition, the comparison to the cluster environment (see Sect. 9.1.1) shows that groups tend to reside in less dense environments, although they also cover the range of environmental densities in which clusters are situated.

The distribution of the centrals' luminosity in the bottom right panel of Fig. 37 reveals the magnitude cut which was imposed on the fossil systems. Their distribution is similar to a tail of a Gaussian. Remarkably, the centrals of star forming "fossils" are on average slightly brighter in the r band than those of red FGs. This is not a "projection" effect. If we were plotting the whole distribution without applying the luminosity cut-off, a gap of ~ 1 mag would be visible between the mean M_r-values of both fossil samples. The difference between the median magnitude of the centrals of our luminosity limited samples is ~ 0.1 mag – not a large gap. The centrals of the control sample, in contrast, have a much lower median r band luminosity, even compared to their cluster counterparts they are much fainter. Of course, there is always another similarly bright galaxy nearby. This seemingly implies that it is very unlikely that those non-star forming control groups harbor a central galaxy brighter than $M_r \leqslant -22$ mag (1 of 141 groups).

For the sake of completeness, B/T ratios of the central galaxies are provided in the lower right panel of Fig. 37. It shall be stressed here that the B/T might not be reliable since Guo *et al.* (2011) mention that the reddest galaxies are passive but contain a disk. This is seen for the red FG sample in the figure. The majority has $B/T \approx 1$, i.e., they are ellipticals. On the other hand,

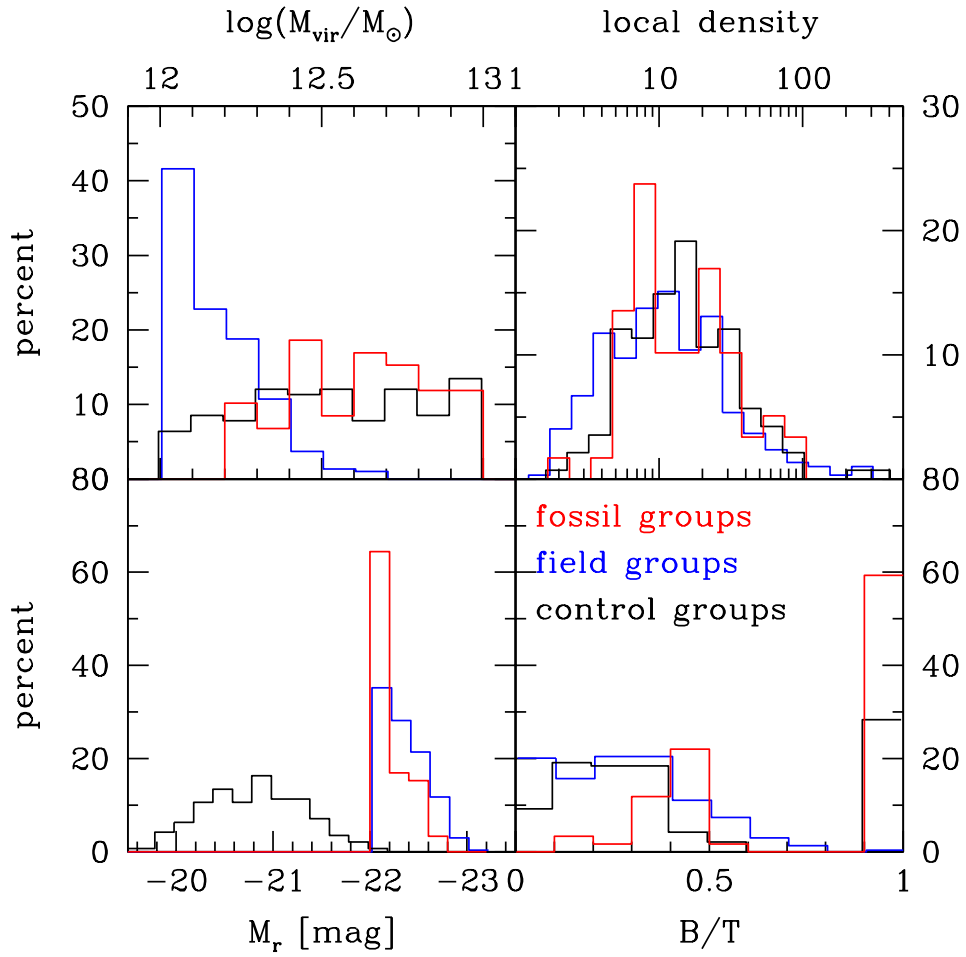

Figure 37: Same as Fig. 34 but for groups with masses $10^{12} \leqslant M_{vir}/M_{\odot} \leqslant 10^{13}$ at $z = 0$. Red data are FGs, black data represent the control sample while blue lines belong to the star forming "fossil" sample (see text). Control groups and FGs have similar mass distribution and similar environment. The properties of their central galaxies differ (see text). The blue "fossil" sample are low mass groups in low dense regions with central disk galaxies.

$\sim$ 40% of all red FGs have disks in the model although we consider all centrals in the red FG sample to be ellipticals because they are passive (see Sect 8.3.1).

The control sample central galaxies is even stronger affected by galaxies with $B/T < 0.7$, although the same constraints were imposed on both samples, except for the luminosity cut-off. 70% of control centrals are (passive) disk galaxies but supposedly ellipticals. This is expected as Guo *et al.* (2011) note that (passive) disk galaxies dominate particularly the intermediate stellar mass regime of the reddest galaxies ($9.5 \leqslant \log M_* \leqslant 11.0$), which is similar to the stellar mass range of the control centrals. The lower stellar mass range as compared to FGs is indirectly seen in the bottom left panel of Fig. 37 since their luminosities are on average more than 1 mag fainter. In any case, the blue and star forming "fossil" centrals are purely disk galaxies.

There are two points to emphasize regarding Fig. 37. The passive FG sample and the passive control sample have similar masses and reside in similar environments, they are thus comparable. Their different central galaxies are expected since FG centrals are outstanding in terms of their luminosity as we have imposed a luminosity cut-off on these. The other point to make concerns the blue "fossils". They reside in low density regions, have low masses, and their centrals are star forming disk galaxies. We now may identify these "fossils" as loose groups, their centrals may represent field galaxies.

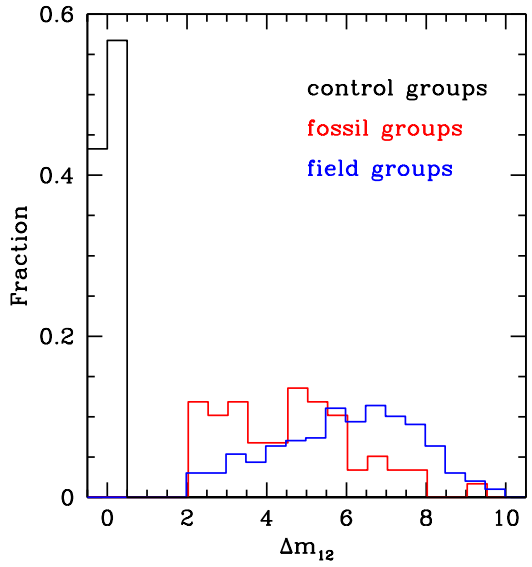

Figure 38: Magnitude gap distribution. The magnitude gap of field groups is on average larger than that of fossil groups.

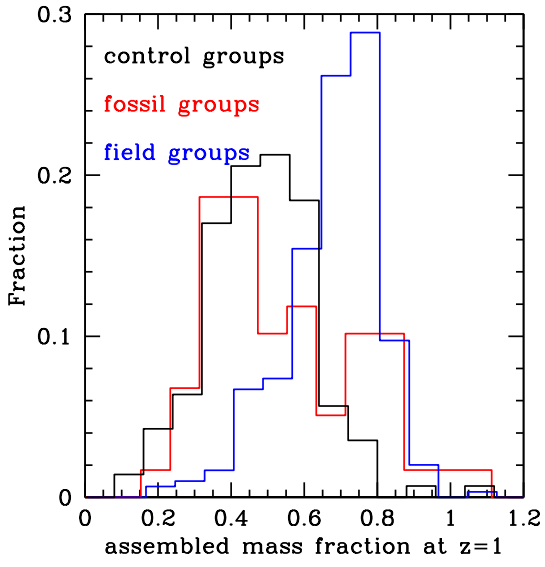

Figure 39: Fraction at $z = 1$ of the final assembled mass. While most of the field groups have assembled more than 70% of their final mass at $z = 1$, almost no control group assembles more than 65% of its final mass at $z = 1$. The fossil groups distribution looks split. The major fraction are late assemblers but also a significant fraction of the fossils has assembled most of its final mass at $z = 1$.

In Fig. 38 the magnitude gap distribution of the samples is shown. Of course, the cut-offs which are imposed on the samples are visible. The figure also shows that the field groups have on average larger magnitude gaps than the fossil groups – represented by the shift between both samples. The field distribution peaks at $6 \sim 7$ mag. This is a giant gap between the BGG and the second ranked galaxy, justifying the terminology "field group". However, the fossil group's Δm_{12}-distribution looks bimodal, maybe due to low number statistics but more likely because of the imposed criteria (in particular the SFR criterion).

We therefore also examine the fraction of assembled mass at $z = 1$ as opposed to the final mass achieved at $z = 0$, illustrated in Fig. 39. Clearly, field groups have assembled the major fraction of their final mass already ~ 7.6 Gyr in the past. The median of the distribution is a fraction of 71%. Control groups assemble their mass on average later. The median control group has assembled 48% of its final mass at $z = 1$. On the other hand, roughly half of the control groups have assembled half of their final mass or more at $z = 1$.

The picture for the fossil groups again looks more complicated, maybe bimodal. They seem to follow the distribution of the control groups. But there is a significant fraction of fossil groups which have assembled $\sim 80\%$ of their final mass already at $z = 1$. There is no correlation with the two peaks of the fossil distribution in Fig. 38. Roughly half of the fossil groups with a high assembled mass fraction have $\Delta m_{12} < 4$, so do not behave like the field groups as one could have expected from the assembled mass distribution. Similarly there is no correlation with B/T ratios either (not illustrated in the figures).

However, as seen in Fig. 39 at the high fraction tail, there are (fossil) groups that had assembled more mass at $z = 1$ as compared to $z = 0$, i.e., they have lost mass. Therefore, the process of mass loss provides an reasonable explanation for shifting groups within the figure. On the

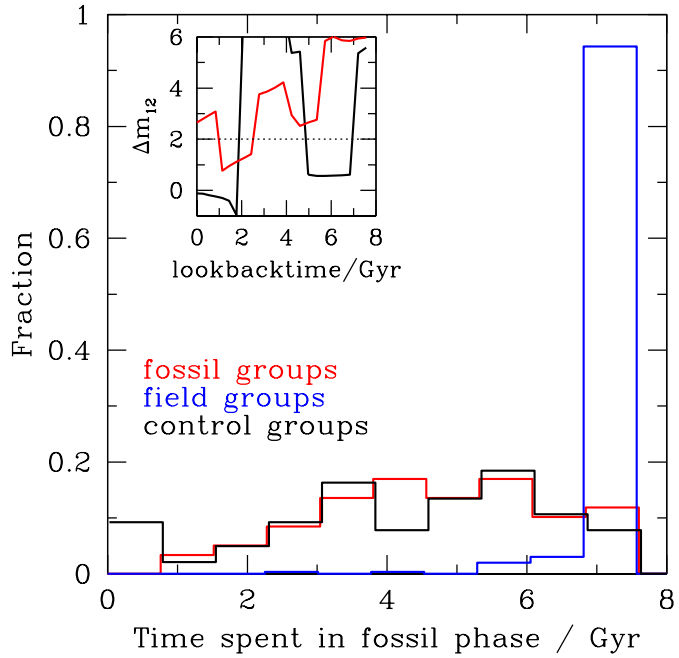

Figure 40: Time spent in fossil phase since $z = 1$ for groups as indicated in the figure. The broadened distributions of both the passive FG and control sample "peak" at ~ 5 Gyrs and are similar to each other. The inlay plot shows the Δm_{12} history for two arbitrarily chosen fossil and control groups. It illustrates the transient character of the fossil phase. In stark contrast, almost all star forming field groups have spent the complete 7.6 Gyrs in the fossil phase.

other side, only 5 of 16 fossil groups with $\alpha_{1.0} > 0.7$ experience a significant mass loss since $z = 1$ (more than 20% between two arbitrary snapshots).

9.2.2 *The fossil phase*

In Sect. 9.1.2 we have found evidence in the G11 model that the fossil phase seems indeed transient in a cluster's evolution. In this section this phase shall be examined in more detail. We thus extract from the SAM[1] how often a group was in the fossil phase since $z = 1$. Fig. 40 displays the distribution of time which a group has spent in the fossil phase, i.e., during that time there was no other bright galaxy – according to the magnitude gap of 2 – within half the virial radius.

The distributions of the passive fossil and the control sample are strikingly similar. They span the whole range of values, but none of the fossil groups has spent less than ~ 0.8 Gyrs in the fossil phase. Most of the groups in both samples have spent at least ~ 2 Gyrs in a fossil phase, in some cases several times. Interestingly, even ~ 8% of all control groups were fossils for more than 7 Gyrs. A bright galaxy has entered their $0.5r_{vir}$-sphere only recently as they are labeled "control". However, the similar distributions of the control and the fossil sample are a manifestation of the transient fossil phase.

The picture is completely different for the star forming field groups. Almost all of those have spent more than ~ 7 Gyrs in the fossil phase, which is in this case not transient. Although we know that they did not experience any major merger in the past (see Sect. 8.3.1, this is

1 In this calculation a group is considered to remain fossil for the whole time period between two snapshots, as indicated by the inlay plot of Fig. 40. This introduces an uncertainty of up to 0.35 Gyrs within a snapshot. However, this uncertainty applies to both situations. Groups can leave or enter the fossil phase. On average and for a large sample both uncertainties might cancel out unless there was no preference of galaxies to cluster as they attract each other, biasing the magnitude gap. That is, one of both regimes might be entered one time more as compared to the other. Therefore, the mentioned uncertainty applies which is a maximum error of ~ 5% as compared to the whole "observation" period of 7.6 Gyrs.

somewhat surprising since it apparently also excludes that any other bright galaxy was nearby during the last 7.6 Gyrs. This is another evidence that they must be "loose groups" of field galaxies.

9.2.3 *The faint satellite system*

As the LF is a key tool to study the faint satellite system of a cluster or group it is a crucial point of this work to figure out what values for faint end slopes can be obtained from the galaxy groups of the G11 SAM, particularly in the light of the normal slope that we found in our study of NGC 6482 (see Sect. 5.3). As fossil groups are special due to their magnitude gap, a Schechter function will not be appropriate to fit their LFs. In a first approach, we instead fit the faint end only and use a simple linear approximation whose slope represents the faint end slope. In order to compare the groups to each other, the LF is normalized to the volume a group occupies, determined by its virial radius. Hence, the galaxy number is scaled to the virial volume in order not to overweight the number density of massive groups (or underrepresent less massive groups) in the calculation. After that the LF is examined in two different ways.

The first method fits a linear function (in log-number-magnitude) to the faint end of the LF of each group within a sample ($-18\,\mathrm{mag} \leqslant M_r \leqslant -10\,\mathrm{mag}$). Errors on the number counts are treated as Poissonian, and are incorporated as weights into the liner fitting. After that, the obtained functions are statistically analyzed, represented by mean and standard deviation. We only provide 1σ confidence levels because the distributions are not Gaussian (we return to this issue later).

The other determination method collects all galaxies within a given magnitude bin from all groups of a sample and sums them up (normalized by volume and number of considered groups). This treatment returns a composite LF, i.e., all galaxies in the sample are considered to belong to one single group. It provides a smooth distribution which is less affected by low number statistics as compared to the first method. In order to account for the Poissonian error on a single number count that a group galaxy contributes, errors are propagated accordingly. While the latter method provides a view on the global properties of the sample LF, the former method gives insights into the scatter around those global properties.

The resulting luminosity functions are presented in Fig. 41. The results of the first computation method are displayed by lines – dashed for the mean linear fit, solid for the corresponding 1σ scatter. The data points belong to the composite LFs. The mean slope of all single LF fits within a sample is given in the top left corner and the slope of the composite LF (linear fit) is provided in the bottom right corner.

The absolute numbers differ significantly from those given in Fig. 23, where Guo *et al.* (2011) compare the overall abundance of galaxies within the whole SAM and compare it to a SDSS volume of $7.6 \times 10^5 h^{-3} \mathrm{Mpc}^3$. Of course, within those volumes, universe is on average less dense as compared to our study, yielding lower numbers for Φ – the galaxy number density.

Disregarding the different samples in the top left panel of Fig. 41, the overall shape of the LF looks like a Schechter function, i.e., two power laws at both the faint and the bright end. Of course, there are differences. At the bright end, each sample departs from a normal Schechter function, owing to the environment we are looking at – the centers. The brightest galaxies are known to reside in the centers of groups and clusters, so we always catch the BGG.

The bright end of the field LF provides a surprise since a data point is missing at $M_r = -21.5\,\mathrm{mag}$. This is not expected since we are consider all galaxies within the complete virial radius. The missing data point indicates that even within the virial radius the fossil criterion still holds for the field groups. In the case of fossil groups the magnitude gap is washed out

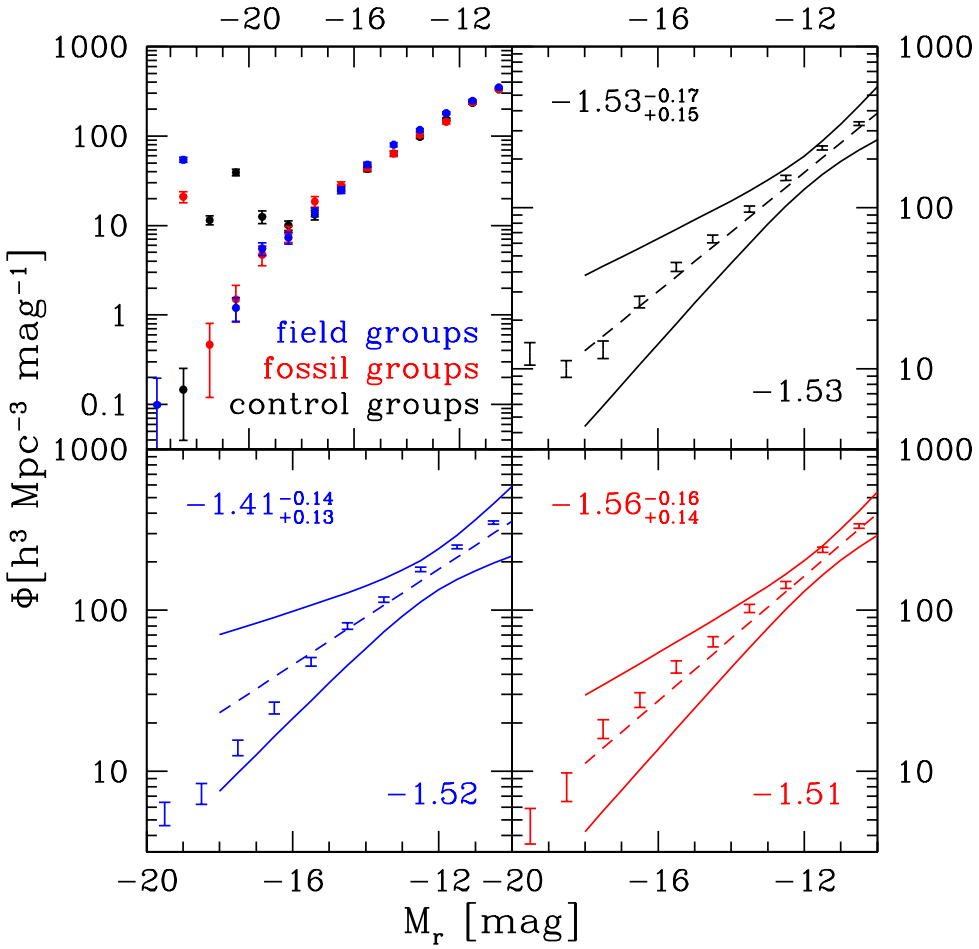

Figure 41: Luminosity functions on the group mass scale. Top left panel: data points represent the composite LF of each sample assuming Poissonian errors (see text). The remaining three panels are close-ups of each sample (color coding as indicated) to emphasize the faint end. Dashed lines represent the mean value which is obtained when evaluating the function values of the linear fit to the luminosity function of each single group in the sample. Solid lines denote the corresponding 1σ scatter. Numbers in the top left corner of each panel provide the slope of a linear function which is fitted to the mentioned mean values, including 1σ scatter. Numbers in the bottom right corner provide the slope of a linear function fitted to the composite LF in the interval $-18 \leqslant M_r \leqslant -10$ mag.

because in some cases there are apparently bright galaxies nearby. This is not a sampling effect, since all magnitude bins are centered accordingly. All BGGs of the fossil sample are cumulated in the −22.5 mag bin. In return, the number densities at the bright end of the control sample are generally high as compared to the other samples. This is owing to (a) the broad range of central galaxy luminosities (see bottom left panel of Fig. 37) and (b) their definition – there has to be a comparable bright galaxy nearby.

The focus of the figure, however, is on the faint satellites. Therefore, close-ups of the faint end of the LFs for each sample are presented in the other three panels of Fig. 41. The composite LF of the control sample follows tightly the mean LF of the individual groups, i.e., the composite LF is a good representation of individual LFs. This is also reflected in the same slopes for the mean LF and the composite LF. Furthermore, we note that the scatter around the mean LFs is of similar scale for all three samples.

In the case of fossil groups the picture is similar to that of control groups, except that the composite LF tends to lie systematically above the mean individual LF, at least for $-18 \leqslant M_r \leqslant$

-14 mag. However, the both LFs follow each other and their faint end slopes are of the same order.

The field sample looks different. The "bright end" of the composite LF around $M_r \sim -17$ mag deviates significantly from the mean LF of the field sample. Bright dwarfs are underrepresented in field groups as one would expect from a linear faint end. It is therefore not a good representation of field groups. In fact, the faint end dominates these groups. Often, bright dwarf galaxies are missing in those groups. However, at the "faint end", the mean LF and the composite LF agree fairly well.

The different computation methods for both LFs provide an explanation for the different faint end slopes obtained for the field sample ($\alpha = -1.41$ for the mean individual LF and $\alpha = -1.52$ for the composite LF). The composite LF slope averages all data points and is not well constrained as the LF is curved rather than linear. On the other side, the linear fit of the individual LFs often takes only the faintest three bin into account since brighter galaxies do not reside within the virial radius. The low number of data points to be fit is reflected in the larger scatter (solid lines) as compared to the other samples.

In reality, the spatial distribution of galaxies in groups and clusters is hard to obtain. In observations the line-of-sight coordinate information gets lost and only a 2d-projection is obtained. The information of the third missing coordinate is generally achieved by spectroscopy of individual galaxies. The Doppler shift contains recessional velocity information. If a large number n of galaxies within a cluster can be spectroscopic surveyed the radial velocity dispersion σ_r centered on the mean recessional velocity $\bar{v}$ of the galaxy cluster can be calculated by

$$\sigma_r^2 = \frac{1}{n} \sum_i^n (v_i - \bar{v})^2 \tag{8}$$

whereas v_i are the radial velocities of the individual cluster galaxies. The radial velocity dispersion is also a projection of the true 3-d velocity dispersion of the cluster. If the virial theorem applies to a galaxy cluster, the mean velocity of galaxies within the virial radius is about 3 times the 3-d velocity dispersion σ_{200} of the cluster. This implies a 1-d velocity dispersion of $\sigma_r = \sigma_{200}/\sqrt{3}$ which is commonly used in the community (see e.g. Cypriano *et al.* 2006; Evrard *et al.* 2008).

In order to be comparable to observational studies we want to determine the LF for FGs when they are projected. The virial radius shall be known (e.g. from X-ray observations). We then determine all line-of-sight velocities of all galaxies whose projections are located within the virial radius. From those σ_r is calculated. In order to account for the radial extent of the group, we then reject all galaxies from a projected sample which have radial velocities which deviate from the velocity of the central group galaxy by more than $\sqrt{3}\sigma_r$. To make this model more realistic we assume that spectroscopic data is only available for galaxies brighter than $M_r = -18$ mag and so that all dwarf galaxies with projections within the virial radius are taken into account for the LF determination. For the three cartesian projections we calculate the composite LF as done for Fig. 41. The analysis is presented in Fig.42.

The comparison to the unprojected LF of the fossil groups shows that projection does not affect the overall shape of the LF. Within error bars the number densities remain the same at the bright end but are generally higher for the projected LFs. There is also systematical overabundance of dwarf galaxies in every projection. However, the introduced offset does not change the shape of the LFs. In particular, within error bars (~ 0.01) the faint end slope remains the same for each projection. The luminosity distribution of the additionally considered galaxies must thus have a LF similar shaped as the unprojected LF.

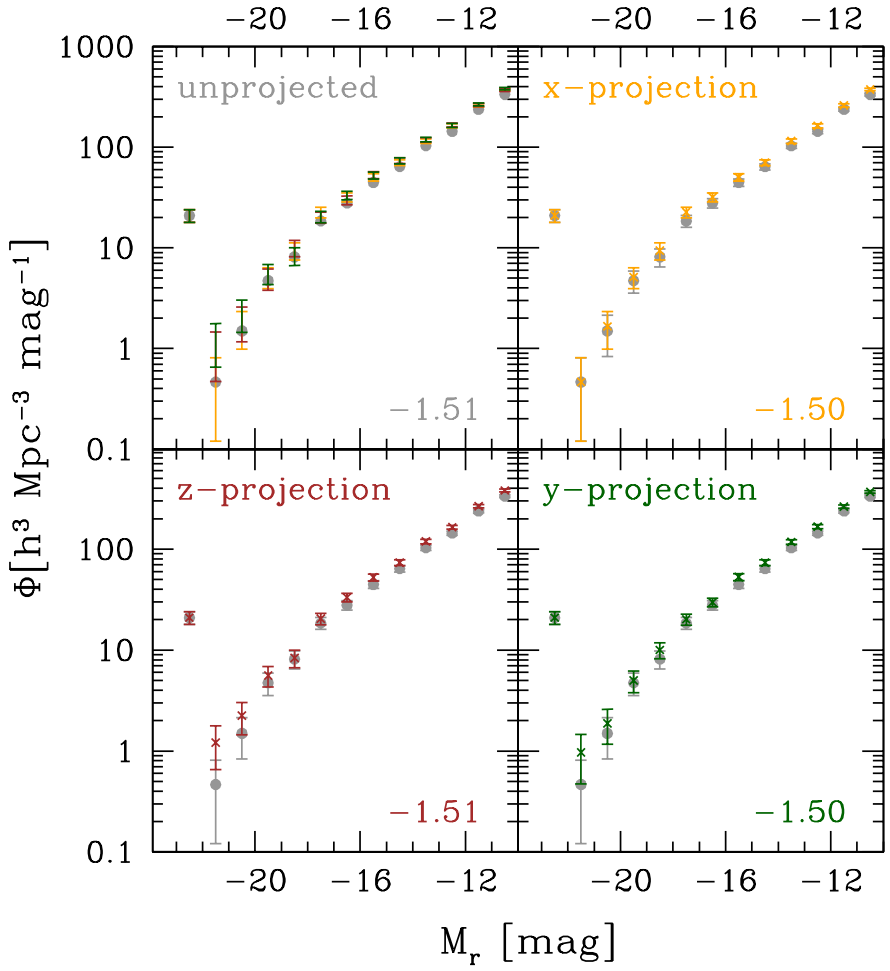

Figure 42: Luminosity functions of fossil groups projected along an axis as labeled in the top of each panel. Shown are the composite LFs as of Fig. 41. Numbers in the bottom right corner are slopes of a linear fit to the faint end of the LF ($-18 \leqslant M_r \leqslant -10$ mag). Top left panel: Comparison between all LFs. The other panels show the comparison of the unprojected LF (gray) and one particular projection (see text). Projection generally overpredicts the number of galaxies. The faint end slope, however, remains unaffected.

As pointed out by Lieder *et al.* (2012), there is an offset between the LF faint end slope of a Schechter fit and an simple linear fit (in log space) such that linear slopes exceed the values of the Schechter slopes. As already mentioned, the Schechter fit is not a good choice for fossil groups or small spatial covered samples. On the other hand we want to compare our results to other studies which generally adopt a Schechter function to fit the LF (see Tab.4). Therefore, in Fig. 43 we present the Schechter faint end slopes which are still meaningful as the faint end is numerous occupied. The figure shows the distribution of the particular mean LFs of Fig. 41.

While the distributions of the Schechter faint end slopes are fairly symmetrical for the control and the fossil groups sample, the distribution is clearly skewed for field groups. Hence, the mean LF is not a good representation for the whole sample of the field group LFs. The median (or even better the mode) are better representatives of a skewed distribution. Median slopes are $-1.44, -1.42$ and -1.31 for the fossil, control and field sample, respectively. These offsets are visible in Fig. 43, with field groups tend to have smaller slopes as the mode of the distribution is $\alpha \sim -1.2$. The differences between the Schechter slope and the linear slope are thus of the order of ~ 0.1, in agreement with Lieder *et al.* (2012). The basic result of Fig. 41 and Fig. 43, however, is the same. The faint satellite system of fossil groups and control groups is comparable in terms

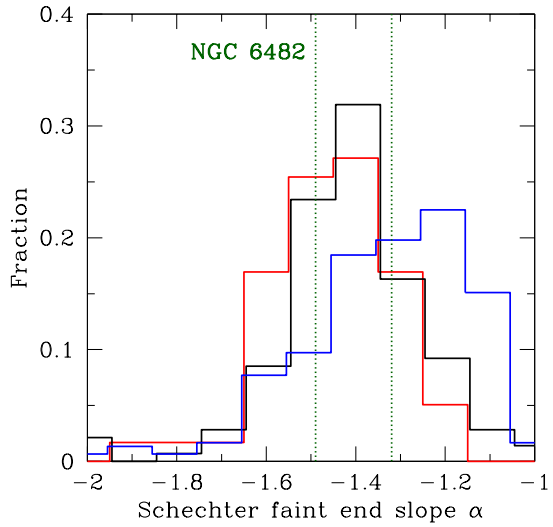

Figure 43: Faint end slopes from Schechter fits to the LF of each fossil (red), control (black) and field groups (blue). While the distributions of the fossil and control sample is fairly symmetric, the field Schechter slope distribution is negatively skewed. Field groups have on average smaller faint end slopes as compared to the control and fossil sample. For comparison, the derived Schechter faint-end slopes for NGC 6482 (see Sect. 5.3) are illustrated by vertical green dotted lines.

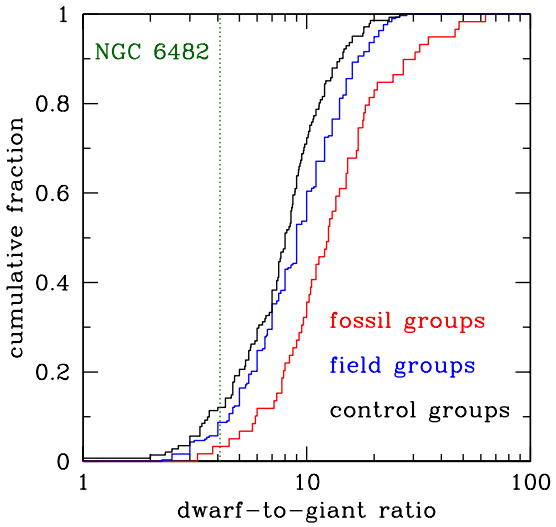

Figure 44: Cumulative distribution of d/g ratios of samples as indicated in the bottom right corner. d/g ratios of control and fossil groups are clearly offset. For comparison, the d/g value of NGC 6482 derived in Sect. 6.3 is denoted by the green dotted line.

of their abundance and luminosity, they have the same faint end slope. The number of faint satellites of field groups, in contrast, increase less strong with decreasing luminosity.

We finish this section with a consideration of dwarf-to-giant ratios for all group samples. The d/g ratio is determined according to Sect. 6.3. Only dwarf galaxies brighter than $M_r = -11$ mag are considered, and the transition between dwarfs and giants is $M_r = -17$ mag. The cumulative d/g distributions obtained within the virial radius are displayed in Fig. 44.

The overall appearance of the three distributions look similar, statistical variance is thus on similar scale among each sample. Therefore, the clear offset between the d/g of fossil and control groups is significant. While the median d/g of fossil groups is 12.5, it is only 8.0 for control groups. Assuming the number of dwarf galaxies is similar among both samples as suggested by Fig. 41, the significant difference can only arise from a different number of bright galaxies. The difference in both d/g ratios could therefore suggest that the number of giants in control groups is a factor of ~ 1.5 larger than that in fossil groups. This appears to be reasonable since control groups are defined to contain more bright galaxies (similar to the central galaxy).

On the other hand, field groups have d/g ratios similar (but somewhat higher, median d/g = 9.0) to those of control groups. This is somewhat surprising and we can only speculate about the reason. The magnitude gap of 2 mag even within r_{vir} suggests a lack of bright galaxies and the shallower faint end slopes may indicate a lower number of dwarf galaxies as compared to the control sample. As a consequence, the d/g ratios of field groups happen to be comparable to those of control groups.

10

DISCUSSION AND CONCLUSIONS

10.1 FOSSIL CLUSTERS

Many publications have been investigating fossil "groups" in the MS using all available SAMs (e.g., Dariush *et al.* 2007; Sales *et al.* 2007; Díaz-Giménez *et al.* 2008; Dariush *et al.* 2010; Díaz-Giménez *et al.* 2011; Cui *et al.* 2011). All of these studies find percentages in the range of $3 \sim 13\%$ for (optical) fossil groups among clusters with masses higher than $M_{vir} \sim 10^{13} h^{-1} M_{\odot}$. In the given mass range, this is in agreement with the occupation statistics of 2dFGRS observations but the fossil fraction of $18\% \sim 60\%$ in the SDSS is (somewhat) higher (van den Bosch *et al.* 2007; Yang *et al.* 2008). According to our definition of a cluster ($\log M_{vir}/h^{1} M_{\odot} > 13.2$) and our selection criteria (see Tab.5) we find a fraction of $\sim 14\%$ of optical fossil clusters in the SAM of Guo *et al.* (2011), in agreement with the quoted studies. When we employ more conditions in order to account for X-ray luminosity and relaxed systems the fractions drops to $\sim 7\%$, in agreement with the optical and X-ray study of Jones *et al.* (2003). However, we stress that this number is confronted with low-number statistics as 12 of only 180 clusters are fossil.

It is known, from a semi-analytical perspective, that fossil clusters assemble their mass earlier than "normal" clusters (Dariush *et al.* 2007; Díaz-Giménez *et al.* 2008, 2011). Our study confirms that behavior for the cluster mass regime, clearly visible in Figs. 27 and 36b. Our finding that fossil clusters reside in less dense environments as compared to "normal" clusters, additionally favors the picture that the "surroundings of fossil groups could be responsible for the formation of their large magnitude gap" (Díaz-Giménez *et al.* 2008).

von Benda-Beckmann *et al.* (2008) have shown in simulations that fossil groups are not an end product of galaxy evolution in a group or cluster environment. New galaxies may infall into the cluster making its fossil status a fossil phase. We confirm that picture of the fossil phase as $\sim 80\%$ of all fossil clusters at $z = 1$ are non-fossil after 7.6 Gyrs, and vice versa, $\sim 80\%$ of fossil clusters at $z = 0$ have been non-fossils at $z = 1$. Although our clusters are afflicted with low number statistics, there is general agreement with the fractions of clusters that remain fossils in the study of Dariush *et al.* (2010). However, control clusters behave in a similar way as they are "non-controls" after the considered time period. This could indicate that fossil clusters can evolve into control clusters, giving rise that no differences should exist between both cluster types. This has found to be true for the BCG properties in SAMs (Cui *et al.* 2011) and in observations (Harrison *et al.* 2012; Zarattini *et al.* 2014; Girardi *et al.* 2014), and is supported by our finding that both merger histories and star formation histories for both types of BCGs are similar from a statistical point of view (see Figs. 30 and 31).

10.2 FOSSIL GROUPS

As far as we aware of, there is no study of fossil groups in the SAM of Guo *et al.* (2011). Beyond that, the group mass regime with masses $10^{12} \leqslant M_{vir}/M_{\odot} \leqslant 10^{13}$ has not been explored so

far, except for Cui *et al.* (2011). On the other hand, those groups are just as massive as NGC 6482 we aim to compare with.

In contrast to the cluster regime, no significant differences exist between control groups and fossil groups. They reside in similarly dense environments, have comparable star formation and merger histories, have similar mass distributions and their faint satellite system is similarly distributed with respect to luminosity. This is in agreement with Cui *et al.* (2011) who find that the satellite number distribution between fossils and non-fossils is not different. It has already been stated by Miles *et al.* (2004) that the faint end slope of the LF should not be affected by (possible) merging activities at the bright end.

Control groups differ from fossil groups by definition. This is reflected by the bright end upturn of their composite LF. In particular, we find that control groups are unlikely to form a central galaxy brighter than $M_r < -22$ mag, the imposed cut-off for fossil centrals. That fossil centrals are on average more than twice as luminous as control centrals could indicate that in fossil groups the two brightest galaxies have merged, making a control group fossil. The same argumentation is used by Zarattini *et al.* (2014) who also find that the fraction of light enclosed in BGGs of (observational) fossil groups is larger than in non-fossil systems.

However, the most striking similarity between fossil and control groups is that they have spent the same time periods in the fossil phase, from a statistical perspective. This is somewhat surprising since control groups are not merely non-fossils, they are sort of counterparts because another galaxy *similar bright* as the central galaxy has to be located nearby. If the fossil phase is part of the evolutionary process of galaxy groups and clusters as pointed out by von Benda-Beckmann *et al.* (2008), it gives rise to an identical evolution of fossil groups and control groups. Galaxy groups are favorite sites for major mergers because in low-mass environments peculiar velocities of galaxies are slower which makes encounters more likely (Dubinski 1998; Zabludoff & Mulchaey 1998). Fossil groups in this picture can be fueled by environment with another bright galaxy and become non-fossils. After a certain time period both galaxies have merged and the group becomes fossil again.

At $z = 1$ control groups have assembled $\sim 50\%$ of their final mass. This is basically in concordance with the major fraction of fossil groups, again emphasizing the similarity among both samples. On the other hand, half of both the fossil and the control groups could be labeled "fossil" if assigning an assembled mass fraction $\alpha_{1.0} > 0.5$ to fossil systems – which is the way to account for the original intention of what a fossil group means (Ponman *et al.* 1994). This has already been shown for the cluster mass regime by Dariush *et al.* (2010) who found a much higher fraction owing to the low number of (optical) fossil groups. However, in our study a significant fraction of fossil groups has achieved $\sim 80\%$ of their final mass at $z = 1$, resembling the typical assembled mass fractions of field groups, which reside in less dense environment as compared to fossil groups and contain a star forming central disc galaxy, i.e., a spiral.

The field groups are actually fossil by both meanings. They have assembled $\sim 70\%$ of their final mass already at $z = 1$ and stand out by huge magnitude gaps between the first and second ranked galaxy, visible in Fig.41. These field or poor groups would fit into the picture of the "failed" group model proposed by Mulchaey & Zabludoff (1999). All baryons are initially used up in a single luminous galaxy. We find that field group centrals are overluminous and have not experienced a major or any merger during the last 7.6 Gyrs. In addition, even within the virial radius there is no other bright galaxy nearby, and the overwhelming majority of field groups has spent almost the whole time since $z = 1$ in the fossil phase. Their faint satellite systems are less unique, as there is a large scatter in the faint end slopes of their LFs. This is in agreement with the finding that LF properties experience a significant variation in low-density

regions Zandivarez & Martínez (2011). These authors note that "galaxy evolution in groups may follow different paths depending on where the group inhabits."

However, field groups are unlikely to have accumulated a significant hot gas halo since gas was not expelled by a major merger. In addition, Cui *et al.* (2011) show that high X-ray luminosity requires are dense environment. Field groups are thus not fossil in the sense of galaxy evolution as intended by Ponman *et al.* (1994) but they are fossil by means of their history. They remained almost untouched by environmental influences and resemble groups which should not have changed significantly since their formation.

In a nutshell, fossil groups and non-fossil groups are strikingly similar suggesting that they are two representations of the same evolutionary process of galaxies. Field groups, on the other hand, are likely to have not changed significantly their appearance since they were formed. An indication that fossil groups (or non-fossil groups) may be merged field groups is given by Fig. 43. The number density of faint satellites in fossil (and control) groups increases stronger than that of field groups, represented by their LF faint end slopes. While giant galaxies merge, the faint satellite systems of two groups do not (Zabludoff & Mulchaey 1998). This could eventually account for the steeper slope for fossils and controls as opposed to field groups. However, this argumentation is not robust as we find that dwarf-to-giant ratios are too high in galaxy groups of the G11 model as compared to observations. The observational study of d/g ratios in different environment shows that typical values for non-fossil systems are $d/g \sim 2-5$ Trentham & Tully (2002). These would be rather extreme cases when compared to d/g ratios of control clusters in the G11 model (see Fig. 44).

Part IV

CONCLUSIONS

CONCLUSIONS

In this thesis various aspects of fossil groups were studied. We provide here a photometric analysis of the nearest fossil group NGC 6482 down to $M_r \simeq -10.5$ mag — to our knowledge the deepest fossil group study yet. Additionally, we investigate the fossil groups in the state-of-the-art semi-analytical model of Guo *et al.* (2011) in order to compare it with the observationally obtained results and to draw conclusions on the evolution of galaxies in groups. The semi-analytic model provides high resolution and is the first one that allows to study the faint satellite systems of fossil groups to luminosities as faint as our observational study. As far as we are aware of, there is no other study of fossil groups in the semi-analytic model of Guo *et al.* (2011).

We found that present day fossil clusters with masses higher than $M_{vir} \approx 2 \times 10^{13} M_\odot$ show properties in agreement with previous semi-analytic studies of fossil clusters (cf. Dariush *et al.* 2007; Díaz-Giménez *et al.* 2008, 2011; Cui *et al.* 2011). Furthermore we found the history of fossil and non-fossil systems to be similar in terms of star formation and number of mergers. In the mass regime of galaxy groups ($10^{11} \leqslant M_{vir}/M_\odot \leqslant 10^{12}$) the similarity between fossil and non-fossil systems is even more pronounced. Both types of galaxy groups reside in similar environments, have similar mass distributions and had assembled similar fractions of mass ~ 8 Gyrs in the past. In particular, we confirmed the scenario that fossil groups are a transient phase in the evolution of galaxy groups. Both fossil and non-fossil groups have spent the same time in the fossil phase. Therefore, this suggests that fossil and non-fossil groups are representations of the same evolutionary track of ordinary galaxy groups.

In agreement with observations(e.g., Lin & Mohr 2004; Zarattini *et al.* 2014), we found central galaxies of fossil groups to be more luminous than those of non-fossil systems where another bright galaxy is in close vicinity. The luminosity difference between central galaxies of fossil and non-fossil is compatible with the evolutionary picture that fossil groups may form by a merger of both bright galaxies in non-fossil systems, which accounts for the overluminous central galaxy in fossils. By this process, a non-fossil group becomes a fossil group, while the infall of another bright galaxy into the systems turns a fossil group non-fossil.

There are no differences among the faint satellite systems of fossil and non-fossil systems in the semi-analytic model. Although Guo *et al.* (2011) show that their model underpredicts the overall abundance of dwarf galaxies, our study revealed that the luminosity function faint-end slopes of both galaxy group types found in the semi-analytic model encompass the observed values in literature (cf. Tab. 4 and Fig. 43). The *missing satellite problem* is thus not of statistical significance in the semi-analytic model of Guo *et al.* (2011). We particularly found the luminosity function's faint-end slope of NGC 6482 in agreement with those of fossil groups in the semi-analytic model (see Fig. 43). However, the dwarf-to-giant ratios the semi-analytic model assigns to galaxy groups are too high in comparison to observations (by a factor of $2 \sim 3$). This was already found by Weinmann *et al.* (2011). Similarly, the dwarf-to-giant ratio of NGC 6482 is very small as compared to those provided by the semi-analytic model for fossil groups (see Fig. 44). This in particular remarkably since we found the faint end, i.e., the number of dwarfs, in agreement with observations. Therefore, giant galaxies must be underrepresented in the groups we have investigated in order to obtain the high ratios.

In NGC 6482 we have not found any dwarf galaxy in the range $-14 \leqslant M_r/mag \leqslant -13$. In the semi-analytic model a deviation in the composite luminosity function for fossil groups in this magnitude range is not evident (see Fig. 42). The "missing" galaxies in this magnitude range are thus a peculiarity of the NGC 6482 system and probably due to low number statistics of its faint satellite system.

Furthermore, we investigated groups in the Guo *et al.* (2011) semi-analytic model that resemble loose or field groups as they reside in low-density environments and their central galaxy is star forming like a spiral galaxy. These groups appear "fossil" in the sense that they had assembled $\sim 80\%$ of their final mass already $\sim 8\,Gyrs$ ago. They have spent almost the whole time since $z = 1$ in the fossil phase, and even within the virial radius they remain (optical) fossils manifested by the magnitude gap of 2. However, they are not fossil within the meaning of Ponman *et al.* (1994), who suspected the outstanding luminous central galaxy to be a merging product of all bright galaxies within the central region of the group. As the central galaxies of our field groups have not experienced any significant merger in the past, they can not contain an elliptical galaxy embedded in a hot gas halo, which would be bright in the X-ray. Field groups therefore represent another evolutionary track in the Guo *et al.* (2011) semi-analytic model. This is also indicated by their systematically shallower faint-end slopes as compared to the fossil and non-fossil systems (see Fig. 43).

The latter fact suggests that encounters of field groups form the systems that we label fossil and non-fossil, i.e., they contain a passive central galaxy. In the course of such an encounter, the giant galaxies will merge earlier than their faint satellites, yielding a steeper faint-end slope. This particular scenario (which might not be the only fossil group formation scenario) implies that mergers of gas-rich (star forming) giant galaxies have taken place in fossil groups and is supported by the finding of wet merger signatures in NGC 6482.

In the future, a major advance of any semi-analytic model would be the incorporation of the emission by the hot gas, i.e., the X-ray luminosity. It is the crux of this work that the Guo *et al.* (2011) model does not provide the X-ray luminosity. Another exercise is to figure out whether the results of the semi-analytic model presented in our study change when considering elliptical galaxies by means of their bulge-to-total ratios, instead of the activity by means of their specific star formation rates. Since the semi-analytic model data is available, we could also prove whether L^* galaxies are indeed missing in fossil groups as claimed by D'Onghia & Lake (2004).

From the available data and the semi-analytic model, fossil groups are merely a phase in the evolution of galaxy groups. In order to specifically understand its beginning (and its end), we would need further insight how fossil groups form in the semi-analytic model, and in particular how their faint satellite system evolves with time.

Part V

APPENDIX

A

DATA REDUCTION

Data reduction is the process that turns raw CCD images into science images, free of artifacts and instrument signatures. Here, all steps of data reduction applied to the Suprime-Cam data of NGC 6482 shall be described briefly in a general manner to introduce the vocabulary used in Sect. 2.3. The interested reader is referred to Howell (2006) for a detailed description of data reduction.

A.1 BIAS CORRECTION

The bias of a pixel is the value that is read out if the CCD was not illuminated, i.e., with an exposure time of 0 seconds. The A/D converter that translates the analog current signal in a digital pixel value, introduces a variation which is not gaussian (Howell 2006). Since the A/D converter can not deal with negative values, each pixel value has to be read in with a positive offset, in order to account for the "negative introduced" values by the A/D converter. In order to determine this offset, additional read-out cycles are sent to the electronics which generates rows or columns of only the signal by the read-out electronics. These ~ 50 columns or rows are commonly referred to as *overscan region*.

As mentioned in Sect. 2.3, after a chip replacement of the Suprime-Cam instrument, the CCDs contained four read-outs, resulting in 4 different overscan regions per CCD (see Fig. 46a). We used `SDFRED`, the Suprime-Cam reduction software, since it was the only one which could handle four read-outs per CCD. `SDFRED` determines the median of each overscan row. The bias is then corrected by subtracting the obtained value from each pixel value in the corresponding row. The different corrected fields are then sticked together by trimming the overscan regions as seen in Fig. 46b.

A.2 FLATFIELDING

Each pixel of a CCD differs from its neighbor in quantum efficiency and *gain*, i.e., the conversion factor of initially read-out electrons in a pixel related to the final number count reported by any software. The process to correct for these *pixel-to-pixel variations* in a detector is called flatfielding. That correction is achieved by illuminating the detector uniformly. The response of each pixel is recorded and called flat field since the illumination is "flat". A side-effect of flatfielding is the correction for so-called vignetting and time dependent dust accumulation in the optical path. This different illumination is thus treated as an intrinsic property of a pixel.

Under the assumption that this response does not change with time, the science images can be divided by the flat fields in order to correct for the pixel-to-pixel variation. Unfortunately, the assumption does not hold so that before and after a observing night flat fields are taken and a combination of those is used instead. Moreover, there is a wavelength dependence of a pixel's

response – the quantum efficiency. In order to account for this issue, commonly a combination of sky flats (at dusk and dawn) and dome flats (recorded in a uniformly illuminated telescope dome) are taken.

We used SDFRED for the flatfielding step of our data reduction because it was able to flat-field the four fields within one chip separately, including their different brightness levels tailas Fig. 46c illustrates. The data was not affected by other large-scale illumination effects so that further superflatting of defringing (see Howell 2006) was not needed.

A.3 ASTROMETRIC CALIBRATION

Astrometry is the precise measurement of position and movement of stars. In particular the precise position of stars is a central but complicated issue in data reduction. There are many effects to be aware of when mapping the sky on the CCD detector. Here we mention a few:

- Temperature gradients in the whole suspension of a telescope and in particular within the (cryogen) detector lead to expansion/shrinking of the whole setup. This affects the effective focal length, and hence the pixel scale.
- The CCDs are slightly tilted to the focal plane that causes the pixels projected on the sky are slightly rectangular and not squared. This results in different X and Y pixel scales.
- In a mosaic camera the chips can be slightly rotated and tilted to each other so that the pixels are not aligned along a global instrument axis.
- The outermost CCDs of the detector cover areas that have a large distance from the optical axis. Also, a spherically curved sky is mapped on a flat detector plane. Field distortions are introduced anyway.

We use THELI for astrometric calibration. It generates a reference catalog of non-saturated stars the image data contains. That catalog is then compared to a catalog of standard stars in order to match relative position and brightness differences within a given tolerance. We have used the PPMXL catalog (Roeser *et al.* 2010) because it covered the NGC 6482 field. This matching is a first order approximation of the astrometry and also imposes a photometric calibration. Because of the issues listed above, in a second step a polynomial approach is been made by THELI to obtain a precise astrometric solution (Erben *et al.* 2005). The pixel scale variation over the whole CCD array is small but reaches ~ 2% in the outskirts as seen in Fig. 45. This leads to an position offset of several pixels when comparing the first order approximation to the third order solution. If not correcting with that accuracy, in the outskirt the coadding image (see below) would contain the same object several times according the number of stacked images – or at least smear over the object significantly.

A.4 BACKGROUND SUBTRACTION

Background or *sky* is characterized by photons which are collected by the detector but not of interest (Howell 2006). Background does not only contain sky, but also photons from unresolved objects read noise and other sources. THELI offers the possibility of either subtracting a constant sky or model the sky to obtain a spatial varying sky. In either case, SExtractor (see Sect. 3.1) is applied in order to reject all bright sources from an image. The from the remaining pixels the sky is estimated. In the case of the model, the background is smoothed by either a Gaussian or SExtractor. The images of CCDs that contain bright galaxies (number 1-3 in Tab. 6)

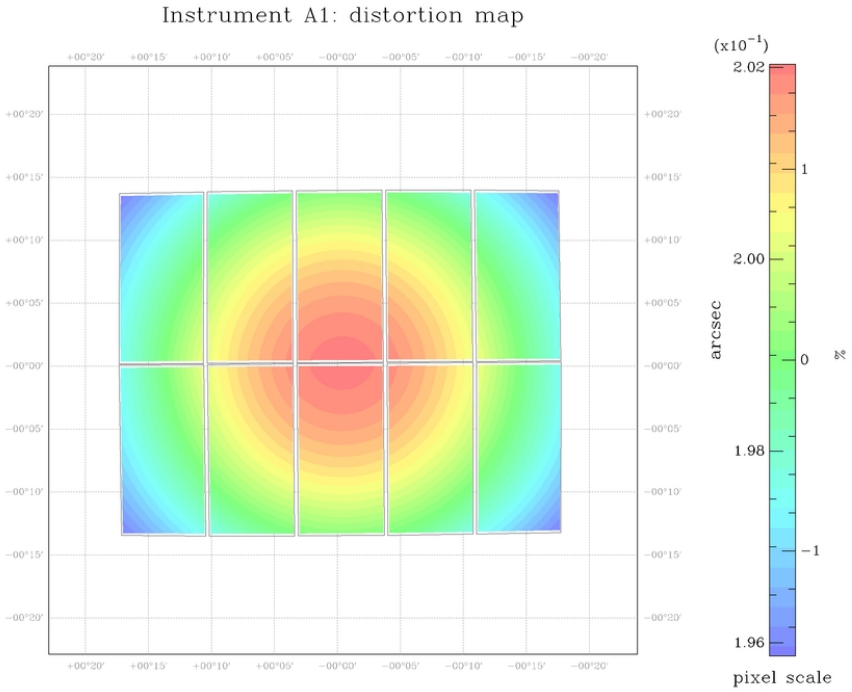

Figure 45: Pixel scale distortion map of R band observations. The deviation from the nominal pixel scale of 0.2 arcsec per pixel is largest in the outskirts of the CCD array, corresponding to the largest field distortions.

were ignored for the background estimation because the smooth brightness gradients were not properly accounted for by `THELI`'s algorithm. This results in an overestimation of the sky (see Lieder 2010 for a detailed description).

A.5 COADDING IMAGES

Deep imaging date are obtained by long time observation – lasting up to hours. But there are good reasons to limit a single exposure to 10–20 minutes, and not to take such a long single exposure.

- The objects of interest will saturate pixels if too much flux is collected.
- The number of cosmic rays[1] hitting the detector increases with time. Those hits are recorded by the CCD and disturb the actual observation. They occur more likely in short wavelengths.
- Atmospheric conditions may change, leading to flux variations (e.g. a cloud may move through the image).
- Dark current caused by the heat of the system begins to become important.

The signal-to-noise (S/N) of an object is determined by many parameters like readout noise, background counts, detector gain, but also the flux of the object of interest (Merline & Howell

1 energy-rich particles originating presumably in supernova explosions (Fermi LAT Collaboration 2013)

1995). If the signal is dominated by the object's flux and the gain is 1 (valid for electrons/photons), the signal-to-noise ratio is simply the Poisson error of its number counts.

$$S/N = \sqrt{N} \tag{9}$$

Howell (2006) mentions, that the S/N is a useful method to define the difference between a bright and a faint source. Deep images need a good S/N so that even faint objects on short exposures look bright on a long exposure. Eq. 9 shows that the relation between exposure time (flux) and S/N is not linear – making deep exposures (time) expensive.

As several "short" exposures are taken, they have to be stacked to obtain a deep image, i.e., with high S/N. The process of stacking the images is called *coadding* and performed by `THELI`. But the exposures might be shifted, rotated and tilted to each other. Therefore, the images have to be geometrically transformed to one global coordinate system. This step uses the astrometric calibration, described in Sect. A.3. During this step `THELI` also checks for flux variations. With increasing airmass the transmitted flux through the atmosphere decreases. Based on fluxes at a given *airmass*[2] `THELI` calculates the expected flux of objects at another airmass. If the flux differs towards lower values than expected (because of a cloud) `THELI` corrects the flux by the `fluxscale` parameter (see Erben *et al.* 2005 for a detailed description).

The particular difficulty in coadding arises from the redistribution of the flux, called resampling (see Bertin 2010 for detailed information). The flux of a certain pixel has to be distributed properly to four pixels by the above mentioned coordinate transformation. However, if the astrometric calibration was accurate and the resampling algorithm advanced, the S/N does not decrease significantly from what is ideally expected as illustrated in Fig. 46d.

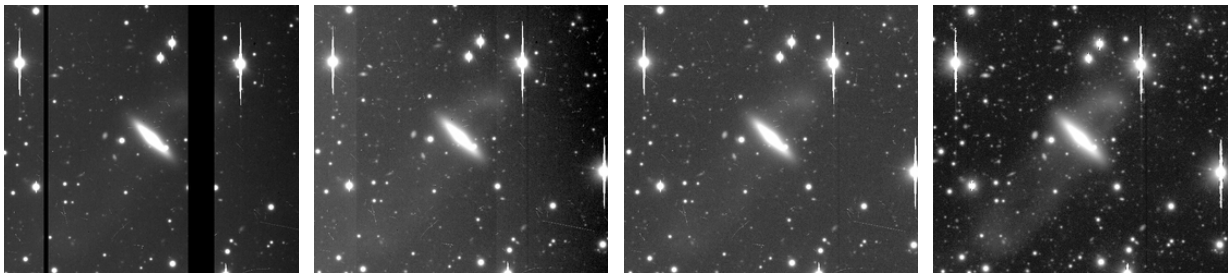

(a) raw image (b) overscan corrected (c) flatfielded (d) coadded

Figure 46: Illustration of the data reduction process for a B band image. (a) The excerpt of the raw image contains three different readout fields within one CCD, and also three overscan regions are shown. (b) The image is corrected by the readout bias and trimmed but brightness differences among the readout fields are visible. (c) The flatfielding step removes not only those brightness differences but also the global brightness gradient (vignetting). (d) By stacking four 520s exposures the S/N increases, making the tidal debris of the disrupted galaxy not disappear in the noise. Background has been subtracted and cosmic rays were removed (see lower right corner). The image is not smeared and no object has a ghost companion, i.e., astrometric calibration, needed for stacking, was precise.

2 In astronomy, airmass is a number for the optical path length through Earth's atmosphere.

B

TABLES

Table 6: Parameters of all investigated objects.

ID	RA (J2000.0)	DEC (J2000.0)	M_R [mag]	M_B [mag]	$B-R$ [mag]	μ_e [mag/arcsec^2]	r_e [kpc]	n	Type
1*	267.95346	23.07192	-22.73 ± 0.02	-21.09 ± 0.02	$1.73 \pm 0.02^{\ddagger}$	19.88 ± 0.02	3.73 ± 0.13	2.82 ± 0.03	E
2*	268.22717	23.21117	-20.54 ± 0.04	-18.92 ± 0.07	1.72 ± 0.07	21.01 ± 0.01	2.42 ± 0.13	1.05 ± 0.01	Sc
3*	267.69073	23.13864	-20.26 ± 0.02	-18.64 ± 0.03	1.69 ± 0.02	18.94 ± 0.01	0.85 ± 0.13	1.88 ± 0.02	S0
4*	268.20694	23.01428	-19.69 ± 0.04	-18.53 ± 0.05	1.19 ± 0.06	21.84 ± 0.02	2.88 ± 0.13	1.07 ± 0.03	SBc
5	268.09314	22.87197	-19.15 ± 0.09	-17.97 ± 0.09	1.19 ± 0.07	23.51 ± 0.03	4.99 ± 0.14	0.60 ± 0.03	SBc
6	267.90015	23.07572	-18.38 ± 0.01	-16.75 ± 0.03	1.60 ± 0.01	21.71 ± 0.02	1.36 ± 0.13	1.38 ± 0.03	S(lens)0
7	267.68355	23.14623	$-17.70^{-0.5}_{+0.01}$	$-16.37^{-0.5}_{+0.02}$	$1.33 \pm 0.13^{\dagger}$	—	—	—	disrupted
8	267.74030	22.90452	-17.66 ± 0.02	-16.25 ± 0.02	1.53 ± 0.02	22.44 ± 0.01	1.42 ± 0.13	1.42 ± 0.01	dE,N
9	267.78040	23.14328	-17.23 ± 0.05	-16.17 ± 0.05	1.07 ± 0.05	23.05 ± 0.01	1.59 ± 0.13	1.12 ± 0.02	dIrr
10	267.84186	23.06776	-16.51 ± 0.02	-15.08 ± 0.04	1.55 ± 0.01	23.09 ± 0.01	1.13 ± 0.13	1.34 ± 0.01	dE,N
11	268.22913	23.11805	-16.35 ± 0.03	-14.96 ± 0.06	1.52 ± 0.02	23.81 ± 0.01	1.22 ± 0.13	1.09 ± 0.01	dE,N
12	267.85382	23.06654	-15.90 ± 0.04	-14.53 ± 0.05	1.42 ± 0.03	24.20 ± 0.01	1.62 ± 0.13	0.74 ± 0.01	dE
13	267.76700	22.85475	-15.76 ± 0.05	-14.38 ± 0.08	1.47 ± 0.02	23.68 ± 0.01	1.01 ± 0.13	1.20 ± 0.02	dE,N
14	267.91089	23.12349	-15.67 ± 0.04	-14.35 ± 0.06	1.41 ± 0.03	23.66 ± 0.02	1.02 ± 0.13	1.54 ± 0.02	dE,N
15	267.76242	23.04759	-15.30 ± 0.05	-14.17 ± 0.06	1.11 ± 0.08	23.72 ± 0.02	0.73 ± 0.13	0.55 ± 0.01	dIrr
16	267.66498	23.25852	-15.08 ± 0.07	-13.90 ± 0.08	1.19 ± 0.03	23.90 ± 0.02	0.96 ± 0.13	0.85 ± 0.02	dIrr?
17	267.81354	23.30462	-14.64 ± 0.03	-13.48 ± 0.05	1.14 ± 0.03	23.95 ± 0.02	0.71 ± 0.13	1.08 ± 0.04	dIrr
18	267.68402	22.87308	-14.61 ± 0.07	-13.09 ± 0.09	1.55 ± 0.02	24.82 ± 0.02	1.16 ± 0.13	0.87 ± 0.01	dE
19	268.04355	22.84158	-14.22 ± 0.05	-12.83 ± 0.12	1.48 ± 0.04	24.01 ± 0.01	0.63 ± 0.13	0.99 ± 0.01	dE,N
20	267.75461	23.08187	-14.21 ± 0.08	-12.92 ± 0.25	$2.48^{+0.12}_{-1.13}$	25.91 ± 0.09	2.37 ± 0.20	1.32 ± 0.06	dE
21	267.69376	22.86386	-14.19 ± 0.07	-12.70 ± 0.08	1.57 ± 0.03	24.22 ± 0.01	0.68 ± 0.13	0.71 ± 0.01	dE,N
22	267.93338	23.09780	-14.11 ± 0.15	-12.52 ± 0.35	1.74 ± 0.13	25.84 ± 0.14	2.28 ± 0.27	1.11 ± 0.09	dE,N
23	267.84854	23.17222	-12.95 ± 0.21	-11.61 ± 0.19	1.38 ± 0.09	25.47 ± 0.02	0.73 ± 0.13	0.66 ± 0.02	dE
24	267.72772	23.02693	-12.91 ± 0.10	-11.60 ± 0.14	1.41 ± 0.05	24.16 ± 0.01	0.41 ± 0.13	0.60 ± 0.02	dE
25	267.82730	23.01918	-12.87 ± 0.05	-11.69 ± 0.10	1.43 ± 0.04	24.56 ± 0.02	0.49 ± 0.13	1.03 ± 0.02	dE

Continued on Next Page...

Table 6 – Continued

ID	RA (J2000.0)	DEC (J2000.0)	M_R [mag]	M_B [mag]	$B-R$ [mag]	μ_e [mag/arcsec^2]	r_e [kpc]	n	Type
26	267.89713	23.13568	-12.70 ± 0.08	-11.37 ± 0.15	1.48 ± 0.07	25.19 ± 0.02	0.57 ± 0.13	0.60 ± 0.02	dE,N
27	268.15881	23.30970	-12.64 ± 0.09	-11.73 ± 0.12	0.78 ± 0.07	24.64 ± 0.01	0.43 ± 0.13	0.71 ± 0.02	dE
28	267.75369	22.86655	-12.54 ± 0.06	-11.17 ± 0.13	1.50 ± 0.04	25.18 ± 0.02	0.53 ± 0.13	0.78 ± 0.02	dE
29	267.97821	22.92692	-12.53 ± 0.18	-11.21 ± 0.32	1.31 ± 0.11	27.14 ± 0.08	0.88 ± 0.14	0.88 ± 0.06	dE
30	267.80301	23.05564	-12.34 ± 0.07	-11.12 ± 0.22	1.43 ± 0.05	25.53 ± 0.04	0.54 ± 0.13	0.86 ± 0.04	dE,N
31	268.06989	23.01075	-12.33 ± 0.06	-10.94 ± 0.17	1.52 ± 0.06	25.66 ± 0.04	0.67 ± 0.13	0.81 ± 0.03	dE,N
32	267.97345	22.99362	-12.16 ± 0.04	-10.83 ± 0.10	1.37 ± 0.03	24.81 ± 0.02	0.39 ± 0.13	0.84 ± 0.03	dE
33	267.83710	23.06381	-11.94 ± 0.04	-10.64 ± 0.10	1.46 ± 0.03	24.57 ± 0.01	0.32 ± 0.13	0.63 ± 0.01	dE
34	268.01102	23.16201	-11.57 ± 0.09	-10.63 ± 0.08	1.12 ± 0.05	24.30 ± 0.02	0.23 ± 0.13	0.69 ± 0.04	dE
35	267.69958	23.06408	-11.55 ± 0.08	-10.36 ± 0.17	1.36 ± 0.08	25.97 ± 0.07	0.50 ± 0.13	0.59 ± 0.05	dE
36	267.87686	23.19275	-11.44 ± 0.07	-10.06 ± 0.12	1.54 ± 0.11	24.71 ± 0.01	0.29 ± 0.13	0.34 ± 0.01	dE
37	267.92081	23.14277	-11.29 ± 0.09	-10.20 ± 0.24	1.34 ± 0.07	26.14 ± 0.13	0.55 ± 0.14	0.64 ± 0.09	dE
38	268.07532	23.29704	-11.03 ± 0.14	-10.21 ± 0.15	0.96 ± 0.12	25.51 ± 0.03	0.33 ± 0.13	0.42 ± 0.02	dE
39	268.19034	23.20517	-10.92 ± 0.12	-9.80 ± 0.44	1.23 ± 0.10	26.46 ± 0.37	0.47 ± 0.17	1.01 ± 0.33	dE,N
40	268.02652	22.90529	-10.77 ± 0.18	-9.20 ± 0.32	1.49 ± 0.15	26.53 ± 0.34	0.52 ± 0.20	0.72 ± 0.22	dE
41	267.84235	22.85096	-10.76 ± 0.09	-9.47 ± 0.11	1.52 ± 0.10	24.92 ± 0.02	0.24 ± 0.13	0.36 ± 0.02	dE
42	267.67389	23.22414	-10.75 ± 0.14	-8.78 ± 0.25	1.54 ± 0.18	26.92 ± 0.21	0.40 ± 0.16	0.34 ± 0.11	dE
43	267.97455	23.11946	-10.71 ± 0.14	-9.29 ± 0.33	1.46 ± 0.21	27.79 ± 0.27	0.29 ± 0.15	0.67 ± 0.16	dE
44	267.67850	22.96362	-10.67 ± 0.09	-9.76 ± 0.16	1.07 ± 0.07	25.19 ± 0.01	0.23 ± 0.13	0.29 ± 0.01	dE
45	267.85178	23.01907	-10.61 ± 0.17	-9.83 ± 0.22	0.95 ± 0.12	27.06 ± 0.14	0.48 ± 0.14	0.62 ± 0.08	dE
46	268.05835	22.93668	-10.59 ± 0.10	-9.36 ± 0.21	1.53 ± 0.09	25.47 ± 0.04	0.27 ± 0.13	0.52 ± 0.05	dE
47	268.10507	23.04556	-10.55 ± 0.20	-9.52 ± 0.25	1.31 ± 0.12	25.64 ± 0.04	0.31 ± 0.13	0.47 ± 0.04	dE
48	268.06409	22.86462	-10.53 ± 0.30	-9.84 ± 0.29	1.08 ± 0.16	25.94 ± 0.08	0.28 ± 0.13	0.76 ± 0.08	dE

Notes. ID: galaxy identification number in our catalog sorted by M_R. α (J2000): Right ascension, in units of degrees. δ (J2000): Declination, in units of degrees. M_R: absolute R-band magnitude (adopted $m - M = 33.71$ mag), errorbars do not include photometric calibration uncertainty of $\sigma_R = 0.04$ mag. M_B: absolute B-band magnitude (adopted $m - M = 33.71$ mag), errorbars do not include photometric calibration uncertainty of $\sigma_B = 0.12$ mag. $B-R$: integrated $B-R$ colour (within half-light radius r_{50}). μ_e: effective surface brightness in R-band from Sérsic fit in R-band applied to circularized isophotes. r_e: effective radius from Sérsic fit in R-band applied to circularized isophotes, errors include uncertainty introduced by seeing. n: Sérsic index. Type: classification type (for member considered galaxies only; all early-type dwarf galaxies are labeled dE)

$*$ objects with NED-listed velocities, qualiyfing the galaxy as a group member

† color determined using SExtractor

‡ color determined *at* half-light radius

Table 7: Correlation between snapshot number, redshift and lookback time in the Millennium-II Simulation.

snapnum	redshift	H(z)	t	Δt	snapnum	redshift	H(z)	t	Δt
00	127.0	53416.9	13.56	—	34	2.422	239.6	10.79	0.22
01	80.00	26787.1	13.55	0.01	35	2.239	222.1	10.56	0.23
02	40.00	9615.1	13.51	0.04	36	2.070	206.3	10.31	0.25
03	31.25	6703.9	13.48	0.03	37	1.913	192.2	10.06	0.26
04	28.51	5866.5	13.47	0.01	38	1.766	179.5	9.78	0.27
05	26.03	5142.3	13.45	0.02	39	1.630	168.1	9.50	0.28
06	23.79	4515.0	13.43	0.02	40	1.504	157.8	9.20	0.30
07	21.76	3970.8	13.41	0.02	41	1.386	148.6	8.90	0.31
08	19.92	3498.1	13.39	0.02	42	1.276	140.4	8.58	0.32
09	18.24	3086.8	13.37	0.02	43	1.173	133.0	8.25	0.33
10	16.72	2728.4	13.34	0.03	44	1.078	126.3	7.91	0.34
11	15.34	2415.6	13.31	0.03	45	0.989	120.3	7.56	0.35
12	14.09	2142.3	13.27	0.03	46	0.905	115.0	7.20	0.36
13	12.94	1903.1	13.23	0.04	47	0.828	110.1	6.84	0.36
14	11.90	1693.4	13.19	0.04	48	0.755	105.8	6.47	0.37
15	10.94	1509.4	13.15	0.05	49	0.687	102.0	6.10	0.37
16	10.07	1347.7	13.09	0.05	50	0.624	98.5	5.73	0.37
17	9.278	1205.4	13.04	0.06	51	0.564	95.4	5.35	0.38
18	8.550	1079.9	12.97	0.06	52	0.509	92.6	4.97	0.38
19	7.883	969.2	12.90	0.07	53	0.457	90.1	4.60	0.38
20	7.272	871.3	12.83	0.08	54	0.408	87.8	4.23	0.37
21	6.712	784.7	12.74	0.08	55	0.362	85.8	3.85	0.37
22	6.197	707.9	12.65	0.09	56	0.320	84.0	3.49	0.37
23	5.724	639.9	12.56	0.10	57	0.280	82.4	3.13	0.36
24	5.289	579.4	12.45	0.11	58	0.242	80.9	2.77	0.35
25	4.888	525.6	12.33	0.12	59	0.208	79.6	2.43	0.35
26	4.520	477.7	12.21	0.13	60	0.175	78.5	2.09	0.34
27	4.179	435.0	12.07	0.14	61	0.144	77.4	1.76	0.33
28	3.866	397.0	11.92	0.15	62	0.116	76.5	1.44	0.32
29	3.576	363.0	11.76	0.16	63	0.089	75.6	1.13	0.31
30	3.308	332.6	11.59	0.17	64	0.064	74.9	0.83	0.30
31	3.060	305.4	11.41	0.18	65	0.041	74.2	0.54	0.29
32	2.831	281.0	11.22	0.19	66	0.020	73.6	0.26	0.28
33	2.619	259.2	11.01	0.21	67	0.000	73.0	0.00	0.26

Notes. snapnum: number of snapshot ($N + 3$ in Eq. 6). $H(z)$: Hubble constant as function of redshift z in $km\,s^{-1}\,Mpc^{-1}$. t: lookback time in Gyr. Δt: time difference to previous snapshot in Gyr. (priv. comm. S. Weinmann)

BIBLIOGRAPHY

Abel, T., Bryan, G. L. & Norman, M. L. (2002). The Formation of the First Star in the Universe. *Science*, **295**, 93.

Adami, C., Picat, J. P., Savine, C., *et al.* (2006). Deep and wide field imaging of the Coma cluster: the data. *A&A*, **451**, 1159.

Aguerri, J. A. L., Girardi, M., Boschin, W., *et al.* (2011). Fossil groups origins. I. RX J105453.3+552102 a very massive and relaxed system at $z \sim 0.5$. *A&A*, **527**, A143.

Alamo-Martínez, K. A., West, M. J., Blakeslee, J. P., *et al.* (2012). Globular cluster systems in fossil groups: NGC 6482, NGC 1132, and ESO 306-017. *A&A*, **546**, A15.

Alpher, R. A. & Herman, R. (1948). Evolution of the Universe. *Nature*, **162**, 774.

Alpher, R. A., Follin, J. W. & Herman, R. C. (1953). Physical Conditions in the Initial Stages of the Expanding Universe. *Physical Review*, **92**, 1347.

Amanullah, R. & the Supernova Cosmology Project. (2010). Spectra and Hubble Space Telescope Light Curves of Six Type Ia Supernovae at $0.511 \leqslant z \leqslant 1.12$ and the Union2 Compilation. *ApJ*, **716**, 712.

Anderson, L., Aubourg, E., Bailey, S., *et al.* (2012). The clustering of galaxies in the SDSS-III Baryon Oscillation Spectroscopic Survey: baryon acoustic oscillations in the Data Release 9 spectroscopic galaxy sample. *MNRAS*, **427**, 3435.

Baade, W. (1944). NGC 147 and NGC 185, Two New Members of the Local Group of Galaxies. *ApJ*, **100**, 147.

Bahé, Y. M., McCarthy, I. G., Balogh, M. L. & Font, A. S. (2013). Why does the environmental influence on group and cluster galaxies extend beyond the virial radius? *MNRAS*, **430**, 3017.

Barkana, R. & Loeb, A. (2001). In the beginning: the first sources of light and the reionization of the universe. *Phys. Rep.*, **349**, 125.

Barnes, J. E. (1988). Encounters of disk/halo galaxies. *ApJ*, **331**, 699.

Bartelmann, M. (2010). The dark Universe. *Reviews of Modern Physics*, **82**, 331.

Bedregal, A. G., Aragón-Salamanca, A. & Merrifield, M. R. (2006). The Tully-Fisher relation for So galaxies. *MNRAS*, **373**, 1125.

Bell, E. F., McIntosh, D. H., Katz, N. & Weinberg, M. D. (2003). The Optical and Near-Infrared Properties of Galaxies. I. Luminosity and Stellar Mass Functions. *ApJS*, **149**, 289.

Bell, E. F., Naab, T., McIntosh, D. H., *et al.* (2006). Dry Mergers in GEMS: The Dynamical Evolution of Massive Early-Type Galaxies. *ApJ*, **640**, 241.

Bender, R. (1988). Velocity anisotropies and isophote shapes in elliptical galaxies. *A&A*, **193**, L7.

Bender, R., Doebereiner, S. & Moellenhoff, C. (1988). Isophote shapes of elliptical galaxies. I - The data. *A&AS*, **74**, 385.

Benson, A. J., Bower, R. G., Frenk, C. S., *et al.* (2003). What Shapes the Luminosity Function of Galaxies? *ApJ*, **599**, 38.

Beringer, J., Arguin, J.-F., Barnett, R. M. & the Particle Data Group. (2012). Review of Particle Physics. *Phys. Rev. D*, **86(1)**, 010001.

Bernardeau, F., Colombi, S., Gaztañaga, E. & Scoccimarro, R. (2002). Large-scale structure of the Universe and cosmological perturbation theory. *Phys. Rep.*, **367**, 1.

Bertin, E. (2010). *SWarp: Resampling and Co-adding FITS Images Together*. Astrophysics Source Code Library.

Bertin, E. & Arnouts, S. (1996). SExtractor: Software for source extraction. *A&AS*, **117**, 393.

Beutler, F., Blake, C., Colless, M., *et al.* (2011). The 6dF Galaxy Survey: baryon acoustic oscillations and the local Hubble constant. *MNRAS*, **416**, 3017.

Binggeli, B., Sandage, A. & Tammann, G. A. (1988). The luminosity function of galaxies. *ARA&A*, **26**, 509.

Binney, J. (1978). On the rotation of elliptical galaxies. *MNRAS*, **183**, 501.

Binney, J. & Tremaine, S. (2008). *Galactic Dynamics*. 2nd edition. Princeton University Press, New Jersey.

Blake, C., Kazin, E. A., Beutler, F., *et al.* (2011). The WiggleZ Dark Energy Survey: mapping the distance-redshift relation with baryon acoustic oscillations. *MNRAS*, **418**, 1707.

Blanton, M. (2008). A giant astronomical survey completes its mission: A new mission begins. *SDSS Press Release*.

Blanton, M. R., Lupton, R. H., Schlegel, D. J., *et al.* (2005). The Properties and Luminosity Function of Extremely Low Luminosity Galaxies. *ApJ*, **631**, 208.

Blumenthal, G. R., Faber, S. M., Primack, J. R. & Rees, M. J. (1984). Formation of galaxies and large-scale structure with cold dark matter. *Nature*, **311**, 517.

Böhringer, H., Briel, U. G., Schwarz, R. A., *et al.* (1994). The structure of the Virgo cluster of galaxies from Rosat X-ray images. *Nature*, **368**, 828.

Böhringer, H., Voges, W., Huchra, J. P., *et al.* (2000). The Northern ROSAT All-Sky (NORAS) Galaxy Cluster Survey. I. X-Ray Properties of Clusters Detected as Extended X-Ray Sources. *ApJS*, **129**, 435.

Bond, J. R. & Efstathiou, G. (1984). Cosmic background radiation anisotropies in universes dominated by nonbaryonic dark matter. *ApJ*, **285**, L45.

Bond, J. R., Cole, S., Efstathiou, G. & Kaiser, N. (1991). Excursion set mass functions for hierarchical Gaussian fluctuations. *ApJ*, **379**, 440.

Boselli, A., Boissier, S., Cortese, L. & Gavazzi, G. (2008). The Origin of Dwarf Ellipticals in the Virgo Cluster. *ApJ*, **674**, 742.

Bower, R. G., Benson, A. J., Malbon, R., *et al.* (2006). Breaking the hierarchy of galaxy formation. *MNRAS*, **370**, 645.

Boylan-Kolchin, M., Springel, V., White, S. D. M., Jenkins, A. & Lemson, G. (2009). Resolving cosmic structure formation with the Millennium-II Simulation. *MNRAS*, **398**, 1150.

Bridge, C. R., Carlberg, R. G. & Sullivan, M. (2010). The CFHTLS-Deep Catalog of Interacting Galaxies. I. Merger Rate Evolution to z = 1.2. *ApJ*, **709**, 1067.

Bruzual, G. & Charlot, S. (2003). Stellar population synthesis at the resolution of 2003. *MNRAS*, **344**, 1000.

Caloi, V. & D'Antona, F. (2007). NGC 6441: another indication of very high helium content in globular cluster stars. *A&A*, **463**, 949.

Calzetti, D., Kennicutt, Jr., R. C., Bianchi, L., *et al.* (2005). Star Formation in NGC 5194 (M51a): The Panchromatic View from GALEX to Spitzer. *ApJ*, **633**, 871.

Cantalupo, S., Arrigoni-Battaia, F., Prochaska, J. X., Hennawi, J. F. & Madau, P. (2014). A cosmic web filament revealed in Lyman-alpha emission around a luminous high-redshift quasar. *ArXiv e-prints*.

Caon, N., Capaccioli, M. & D'Onofrio, M. (1993). On the Shape of the Light Profiles of Early Type Galaxies. *MNRAS*, **265**, 1013.

Caon, N., Cairós, L. M., Aguerri, J. A. L. & Muñoz-Tuñón, C. (2005). Unveiling the Nature of the Low Surface Brightness Stellar Host in Blue Compact Dwarf Galaxies. *ApJS*, **157**, 218.

Cappellari, M., Bacon, R., Bureau, M., *et al.* (2006). The SAURON project - IV. The mass-to-light ratio, the virial mass estimator and the Fundamental Plane of elliptical and lenticular galaxies. *MNRAS*, **366**, 1126.

Chandrasekhar, S. (1943). Dynamical Friction. I. General Considerations: the Coefficient of Dynamical Friction. *ApJ*, **97**, 255.

Cole, S., Aragon-Salamanca, A., Frenk, C. S., Navarro, J. F. & Zepf, S. E. (1994). A Recipe for Galaxy Formation. *MNRAS*, **271**, 781.

Colless, M. & Dunn, A. M. (1996). Structure and Dynamics of the Coma Cluster. *ApJ*, **458**, 435.

Colless, M., Dalton, G., Maddox, S., *et al.* (2001). The 2dF Galaxy Redshift Survey: spectra and redshifts. *MNRAS*, **328**, 1039.

Conselice, C. J., Gallagher, III, J. S. & Wyse, R. F. G. (2002). Galaxy Populations and Evolution in Clusters. II. Defining Cluster Populations. *AJ*, **123**, 2246.

Côté, P., McLaughlin, D. E., Cohen, J. G. & Blakeslee, J. P. (2003). Dynamics of the Globular Cluster System Associated with M49 (NGC 4472): Cluster Orbital Properties and the Distribution of Dark Matter. *ApJ*, **591**, 850.

Cox, T. J., Dutta, S. N., Di Matteo, T., *et al.* (2006). The Kinematic Structure of Merger Remnants. *ApJ*, **650**, 791.

Croton, D. J., Farrar, G. R., Norberg, P., *et al.* (2005). The 2dF Galaxy Redshift Survey: luminosity functions by density environment and galaxy type. *MNRAS*, **356**, 1155.

Croton, D. J., Springel, V., White, S. D. M., *et al.* (2006). The many lives of active galactic nuclei: cooling flows, black holes and the luminosities and colours of galaxies. *MNRAS*, **365**, 11.

Cui, W., Springel, V., Yang, X., De Lucia, G. & Borgani, S. (2011). Properties of fossil groups in cosmological simulations and galaxy formation models. *MNRAS*, **416**, 2997.

Cypriano, E. S., Mendes de Oliveira, C. L. & Sodré, Jr., L. (2006). Velocity Dispersion, Mass, and the Luminosity Function of the Fossil Cluster RX J1416.4+2315. *AJ*, **132**, 514.

Dariush, A., Khosroshahi, H. G., Ponman, T. J., *et al.* (2007). The mass assembly of fossil groups of galaxies in the Millennium simulation. *MNRAS*, **382**, 433.

Dariush, A. A., Raychaudhury, S., Ponman, T. J., *et al.* (2010). The mass assembly of galaxy groups and the evolution of the magnitude gap. *MNRAS*, **405**, 1873.

Davis, M., Efstathiou, G., Frenk, C. S. & White, S. D. M. (1985). The evolution of large-scale structure in a universe dominated by cold dark matter. *ApJ*, **292**, 371.

de Lucia, G. & Blaizot, J. (2007). The hierarchical formation of the brightest cluster galaxies. *MNRAS*, **375**, 2.

de Lucia, G., Kauffmann, G. & White, S. D. M. (2004). Chemical enrichment of the intracluster and intergalactic medium in a hierarchical galaxy formation model. *MNRAS*, **349**, 1101.

de Propris, R., Colless, M., Driver, S. P., *et al.* (2003). The 2dF Galaxy Redshift Survey: the luminosity function of cluster galaxies. *MNRAS*, **342**, 725.

de Vaucouleurs, G. (1948). Recherches sur les Nebuleuses Extragalactiques. *Annales d'Astrophysique*, **11**, 247.

de Vaucouleurs, G. (1959). Classification and Morphology of External Galaxies. *Handbuch der Physik*, **53**, 275.

Dekel, A. & Birnboim, Y. (2006). Galaxy bimodality due to cold flows and shock heating. *MNRAS*, **368**, 2.

Dekel, A. & Silk, J. (1986). The origin of dwarf galaxies, cold dark matter, and biased galaxy formation. *ApJ*, **303**, 39.

Dekel, A. & Woo, J. (2003). Feedback and the fundamental line of low-luminosity low-surface-brightness/dwarf galaxies. *MNRAS*, **344**, 1131.

Dekel, A., Birnboim, Y., Engel, G., *et al.* (2009). Cold streams in early massive hot haloes as the main mode of galaxy formation. *Nature*, **457**, 451.

Díaz-Giménez, E., Muriel, H. & Mendes de Oliveira, C. (2008). Fossil groups in the Millennium Simulation. Evolution of the brightest galaxies. *A&A*, **490**, 965.

Díaz-Giménez, E., Zandivarez, A., Proctor, R., Mendes de Oliveira, C. & Abramo, L. R. (2011). Fossil groups in the Millennium simulation. Their environment and its evolution. *A&A*, **527**, A129.

Dicke, R. H. & Peebles, P. J. E. (1979). The Big Bang Cosmology: Enigmas and Nostrums. *In: General Relativity: An Einstein Centenary Survey*. Cambridge University Press, London.

Dicke, R. H., Peebles, P. J. E., Roll, P. G. & Wilkinson, D. T. (1965). Cosmic Black-Body Radiation. *ApJ*, **142**, 414.

Dietrich, J. P., Werner, N., Clowe, D., *et al.* (2012). A filament of dark matter between two clusters of galaxies. *Nature*, **487**, 202.

Dine, M. & Kusenko, A. (2003). Origin of the matter-antimatter asymmetry. *Reviews of Modern Physics*, **76**, 1.

Djorgovski, S. & Davis, M. (1987). Fundamental properties of elliptical galaxies. *ApJ*, **313**, 59.

Donahue, M., Horner, D. J., Cavagnolo, K. W. & Voit, G. M. (2006). Entropy Profiles in the Cores of Cooling Flow Clusters of Galaxies. *ApJ*, **643**, 730.

D'Onghia, E. & Lake, G. (2004). Cold Dark Matter's Small-Scale Crisis Grows Up. *ApJ*, **612**, 628.

D'Onghia, E., Sommer-Larsen, J., Romeo, A. D., *et al.* (2005). The Formation of Fossil Galaxy Groups in the Hierarchical Universe. *ApJ*, **630**, L109.

D'Onghia, E., Maccio', A. V., Lake, G., Stadel, J. & Moore, B. (2007). Universal Substructure Distributions in LCDM halos: Can we find a Fossil Group? *ArXiv e-prints*.

Doroshkevich, A. G. (1970). The space structure of perturbations and the origin of rotation of galaxies in the theory of fluctuation. *Astrofizika*, **6**, 581.

Doroshkevich, A. G., Zel'dovich, Y. B. & Novikov, I. D. (1967). The Origin of Galaxies in an Expanding Universe. *Soviet Ast.*, **11**, 233.

Dressler, A. (1980). Galaxy morphology in rich clusters - Implications for the formation and evolution of galaxies. *ApJ*, **236**, 351.

Dressler, A., Lynden-Bell, D., Burstein, D., *et al.* (1987). Spectroscopy and photometry of elliptical galaxies. I - A new distance estimator. *ApJ*, **313**, 42.

Drinkwater, M. J., Gregg, M. D. & Colless, M. (2001). Substructure and Dynamics of the Fornax Cluster. *ApJ*, **548**, L139.

Dubinski, J. (1998). The Origin of the Brightest Cluster Galaxies. *ApJ*, **502**, 141.

Duc, P.-A. & Mirabel, I. F. (1998). Young tidal dwarf galaxies around the gas-rich disturbed lenticular NGC 5291. *A&A*, **333**, 813.

Duc, P.-A., Brinks, E., Springel, V., *et al.* (2000). Formation of a Tidal Dwarf Galaxy in the Interacting System Arp 245 (NGC 2992/93). *AJ*, **120**, 1238.

Efstathiou, G., Lake, G. & Negroponte, J. (1982). The stability and masses of disc galaxies. *MNRAS*, **199**, 1069.

Eigenthaler, P. & Zeilinger, W. W. (2012). RX J1548.9+0851, a fossil cluster? *A&A*, **540**, A134.

Einasto, J. (1965). On the Construction of a Composite Model for the Galaxy and on the Determination of the System of Galactic Parameters. *Trudy Astrofizicheskogo Instituta Alma-Ata*, **5**, 87.

Einasto, J., Einasto, M., Tago, E., *et al.* (2007). Superclusters of galaxies from the 2dF redshift survey. I. The catalogue. *A&A*, **462**, 811.

Einstein, A. (1916). Die Grundlage der allgemeinen Relativitätstheorie. *Annalen der Physik*, **354**, 769.

Eisenstein, D. J., Zehavi, I., Hogg, D. W., *et al.* (2005). Detection of the Baryon Acoustic Peak in the Large-Scale Correlation Function of SDSS Luminous Red Galaxies. *ApJ*, **633**, 560.

Emsellem, E., Cappellari, M., Krajnović, D., van de Ven, G. & al., e. (2007). The SAURON project - IX. A kinematic classification for early-type galaxies. *MNRAS*, **379**, 401.

Epanečnikov, V. (1969). Non-parametric estimation of a multivariate probability density. *Theory of Probability and its Applications*, **14**, 156.

Erben, T., Schirmer, M., Dietrich, J. P., *et al.* (2005). GaBoDS: The Garching-Bonn Deep Survey. IV. Methods for the image reduction of multi-chip cameras demonstrated on data from the ESO Wide-Field Imager. *Astronomische Nachrichten*, **326**, 432.

Eskridge, P. B., Frogel, J. A., Pogge, R. W., Quillen, A. C. & al., e. (2000). The Frequency of Barred Spiral Galaxies in the Near-Infrared. *AJ*, **119**, 536.

Evrard, A. E., Bialek, J., Busha, M., *et al.* (2008). Virial Scaling of Massive Dark Matter Halos: Why Clusters Prefer a High Normalization Cosmology. *ApJ*, **672**, 122.

Faber, S. M. & Jackson, R. E. (1976). Velocity dispersions and mass-to-light ratios for elliptical galaxies. *ApJ*, **204**, 668.

Faber, S. M., Willmer, C. N. A., Wolf, C., *et al.* (2007). Galaxy Luminosity Functions to $z \sim 1$ from DEEP2 and COMBO-17: Implications for Red Galaxy Formation. *ApJ*, **665**, 265.

Fall, S. M. & Efstathiou, G. (1980). Formation and rotation of disc galaxies with haloes. *MNRAS*, **193**, 189.

Ferguson, H. C. & Binggeli, B. (1994). Dwarf elliptical galaxies. *A&A Rev.*, **6**, 67.

Fermi-LAT Collaboration, T. (2013). Dark Matter Constraints from Observations of 25 Milky Way Satellite Galaxies with the Fermi Large Area Telescope. *ArXiv e-prints*.

Fermi LAT Collaboration, t. (2013). Detection of the Characteristic Pion-Decay Signature in Supernova Remnants. *Science*, **339**, 807.

Ferrarese, L. & Merritt, D. (2000). A Fundamental Relation between Supermassive Black Holes and Their Host Galaxies. *ApJ*, **539**, L9.

Ferrarese, L., Côté, P., Cuillandre, J.-C., *et al.* (2012). The Next Generation Virgo Cluster Survey (NGVS). I. Introduction to the Survey. *ApJS*, **200**, 4.

Fixsen, D. J. (2009). The Temperature of the Cosmic Microwave Background. *ApJ*, **707**, 916.

FREEDMAN, W. L., MADORE, B. F., GIBSON, B. K., *et al.* (2001). Final Results from the Hubble Space Telescope Key Project to Measure the Hubble Constant. *ApJ*, **553**, 47.

FRIEDMANN, A. (1922). Über die Krümmung des Raumes. *Zeitschrift fur Physik*, **10**, 377.

GADOTTI, D. A. (2009). Structural properties of pseudo-bulges, classical bulges and elliptical galaxies: a Sloan Digital Sky Survey perspective. *MNRAS*, **393**, 1531.

GAMOW, G. (1946). Expanding Universe and the Origin of Elements. *Physical Review*, **70**, 572.

GAMOW, G. (1948). The Origin of Elements and the Separation of Galaxies. *Physical Review*, **74**, 505.

GARNETT, D. R. (2002). The Luminosity-Metallicity Relation, Effective Yields, and Metal Loss in Spiral and Irregular Galaxies. *ApJ*, **581**, 1019.

GAVAZZI, G., RANDONE, I. & BRANCHINI, E. (1995). Colors, luminosities, and masses of disk galaxies. 2: Environmental dependenceis. *ApJ*, **438**, 590.

GELLER, M. J. & HUCHRA, J. P. (1989). Mapping the universe. *Science*, **246**, 897.

GIRARDI, M., AGUERRI, J. A. L., DE GRANDI, S., *et al.* (2014). Fossil Groups Origins IV. The relation between optical and X-ray luminosities. *ArXiv e-prints*.

GNEDIN, N. Y. (2000). Effect of Reionization on Structure Formation in the Universe. *ApJ*, **542**, 535.

GOTT, III, J. R., JURIĆ, M., SCHLEGEL, D., *et al.* (2005). A Map of the Universe. *ApJ*, **624**, 463.

GOVERNATO, F., BROOK, C., MAYER, L., *et al.* (2010). Bulgeless dwarf galaxies and dark matter cores from supernova-driven outflows. *Nature*, **463**, 203.

GRAHAM, A. W. & DRIVER, S. P. (2005). A Concise Reference to (Projected) Sérsic $R^{1/n}$ Quantities, Including Concentration, Profile Slopes, Petrosian Indices, and Kron Magnitudes. *PASA*, **22**, 118.

GREBEL, E. K. (2001). Star Formation Histories of Nearby Dwarf Galaxies. *Astrophysics and Space Science Supplement*, **277**, 231.

GUNN, J. E. & GOTT, III, J. R. (1972). On the Infall of Matter Into Clusters of Galaxies and Some Effects on Their Evolution. *ApJ*, **176**, 1.

GUO, Q., WHITE, S., BOYLAN-KOLCHIN, M., *et al.* (2011). From dwarf spheroidals to cD galaxies: simulating the galaxy population in a ΛCDM cosmology. *MNRAS*, **413**, 101.

GUO, Q., WHITE, S., ANGULO, R. E., *et al.* (2013). Galaxy formation in WMAP1 and WMAP7 cosmologies. *MNRAS*, **428**, 1351.

GUTH, A. H. (1981). Inflationary universe: A possible solution to the horizon and flatness problems. *Phys. Rev. D*, **23**, 347.

HAIMAN, Z. & HOLDER, G. P. (2003). The Reionization History at High Redshifts. I. Physical Models and New Constraints from Cosmic Microwave Background Polarization. *ApJ*, **595**, 1.

HÄRING, N. & RIX, H.-W. (2004). On the Black Hole Mass-Bulge Mass Relation. *ApJ*, **604**, L89.

Harrison, C. D., Miller, C. J., Richards, J. W., *et al.* (2012). The XMM Cluster Survey: The Stellar Mass Assembly of Fossil Galaxies. *ApJ*, **752**, 12.

Hayashi, E., Navarro, J. F., Power, C., *et al.* (2004). The inner structure of ΛCDM haloes - II. Halo mass profiles and low surface brightness galaxy rotation curves. *MNRAS*, **355**, 794.

Hernquist, L. (1992). Structure of merger remnants. I - Bulgeless progenitors. *ApJ*, **400**, 460.

Hilker, M., Infante, L., Vieira, G., Kissler-Patig, M. & Richtler, T. (1999). The central region of the Fornax cluster. II. Spectroscopy and radial velocities of member and background galaxies. *A&AS*, **134**, 75.

Hilker, M., Mieske, S. & Infante, L. (2003). Faint dwarf spheroidals in the Fornax Cluster. A flat luminosity function. *A&A*, **397**, L9.

Hinshaw, G., Larson, D., Komatsu, E., *et al.* (2013). Nine-year Wilkinson Microwave Anisotropy Probe (WMAP) Observations: Cosmological Parameter Results. *ApJS*, **208**, 19.

Hogg, D. W., Baldry, I. K., Blanton, M. R. & Eisenstein, D. J. (2002). The K correction. *ArXiv Astrophysics e-prints*.

Hopkins, P. F., Hernquist, L., Cox, T. J., *et al.* (2006). A Unified, Merger-driven Model of the Origin of Starbursts, Quasars, the Cosmic X-Ray Background, Supermassive Black Holes, and Galaxy Spheroids. *ApJS*, **163**, 1.

Hopkins, P. F., Bundy, K., Hernquist, L. & Ellis, R. S. (2007). Observational Evidence for the Coevolution of Galaxy Mergers, Quasars, and the Blue/Red Galaxy Transition. *ApJ*, **659**, 976.

Hopkins, P. F., Cox, T. J., Dutta, S. N., *et al.* (2009). Dissipation and Extra Light in Galactic Nuclei. II. "Cusp" Ellipticals. *ApJS*, **181**, 135.

Hopkins, P. F., Keres, D., Onorbe, J., *et al.* (2013). Galaxies on FIRE (Feedback In Realistic Environments): Stellar Feedback Explains Cosmologically Inefficient Star Formation. *ArXiv e-prints*.

Howell, S. B. (2006). *Handbook of CCD Astronomy*.

Hoyle, F. (1953). On the Fragmentation of Gas Clouds Into Galaxies and Stars. *ApJ*, **118**, 513.

Hu, W. & Dodelson, S. (2002). Cosmic Microwave Background Anisotropies. *ARA&A*, **40**, 171.

Huang, S., Ho, L. C., Peng, C. Y., Li, Z.-Y. & Barth, A. J. (2013). Fossil Evidence for the Two-phase Formation of Elliptical Galaxies. *ApJ*, **768**, L28.

Hubble, E. (1929). A Relation between Distance and Radial Velocity among Extra-Galactic Nebulae. *Proceedings of the National Academy of Science*, **15**, 168.

Hubble, E. P. (1926). Extragalactic nebulae. *ApJ*, **64**, 321.

Huchra, J. P. & Geller, M. J. (1982). Groups of galaxies. I - Nearby groups. *ApJ*, **257**, 423.

Humphrey, P. J., Buote, D. A., Gastaldello, F., *et al.* (2006). A Chandra View of Dark Matter in Early-Type Galaxies. *ApJ*, **646**, 899.

Hunter, D. A., Elmegreen, B. G. & Martin, E. (2006). Mid-Infrared Images of Stars and Dust in Irregular Galaxies. *AJ*, **132**, 801.

Janz, J., Laurikainen, E., Lisker, T., *et al.* (2012). Dissecting Early-type Dwarf Galaxies into Their Multiple Components. *ApJ*, **745**, L24.

Jarrett, T. H., Polletta, M., Fournon, I. P., *et al.* (2006). Remarkable Disk and Off-Nuclear Starburst Activity in the Tadpole Galaxy as revealed by the Spitzer Space Telescope. *AJ*, **131**, 261.

Jeans, J. H. (1902). The Stability of a Spherical Nebula. *Royal Society of London Philosophical Transactions Series A*, **199**, 1.

Jedrzejewski, R. I. (1987). CCD surface photometry of elliptical galaxies. I - Observations, reduction and results. *MNRAS*, **226**, 747.

Jerjen, H., Kalnajs, A. & Binggeli, B. (2000). IC3328: A "dwarf elliptical galaxy" with spiral structure. *A&A*, **358**, 845.

Jones, L. R., Ponman, T. J. & Forbes, D. A. (2000). Multiwavelength observations of an evolved galaxy group: an end-point of galaxy merging? *MNRAS*, **312**, 139.

Jones, L. R., Ponman, T. J., Horton, A., *et al.* (2003). The nature and space density of fossil groups of galaxies. *MNRAS*, **343**, 627.

Jorgensen, I., Franx, M. & Kjaergaard, P. (1996). The Fundamental Plane for cluster E and So galaxies. *MNRAS*, **280**, 167.

Jungman, G., Kamionkowski, M. & Griest, K. (1996). Supersymmetric dark matter. *Phys. Rep.*, **267**, 195.

Karachentsev, I. D. & Kashibadze, O. G. (2006). Masses of the local group and of the M81 group estimated from distortions in the local velocity field. *Astrophysics*, **49**, 3.

Kashikawa, N., Shimasaku, K., Malkan, M. A., *et al.* (2006). The End of the Reionization Epoch Probed by Lyα Emitters at z = 6.5 in the Subaru Deep Field. *ApJ*, **648**, 7.

Kauffmann, G., White, S. D. M. & Guiderdoni, B. (1993). The Formation and Evolution of Galaxies Within Merging Dark Matter Haloes. *MNRAS*, **264**, 201.

Kauffmann, G., Heckman, T. M., Tremonti, C., *et al.* (2003). The host galaxies of active galactic nuclei. *MNRAS*, **346**, 1055.

Kennicutt, Jr., R. C. (1998). Star Formation in Galaxies Along the Hubble Sequence. *ARA&A*, **36**, 189.

Kereš, D., Katz, N., Weinberg, D. H. & Davé, R. (2005). How do galaxies get their gas? *MNRAS*, **363**, 2.

Khochfar, S. & Burkert, A. (2005). On the origin of isophotal shapes in elliptical galaxies. *MNRAS*, **359**, 1379.

Khosroshahi, H. G., Jones, L. R. & Ponman, T. J. (2004). An old galaxy group: Chandra X-ray observations of the nearby fossil group NGC 6482. *MNRAS*, **349**, 1240.

Khosroshahi, H. G., Ponman, T. J. & Jones, L. R. (2006). The central elliptical galaxy in fossil groups and formation of brightest cluster galaxies. *MNRAS*, **372**, L68.

Klypin, A., Kravtsov, A. V., Valenzuela, O. & Prada, F. (1999). Where Are the Missing Galactic Satellites? *ApJ*, **522**, 82.

Klypin, A. A., Trujillo-Gomez, S. & Primack, J. (2011). Dark Matter Halos in the Standard Cosmological Model: Results from the Bolshoi Simulation. *ApJ*, **740**, 102.

Komatsu, E., Smith, K. M., Dunkley, J., *et al.* (2011). Seven-year Wilkinson Microwave Anisotropy Probe (WMAP) Observations: Cosmological Interpretation. *ApJS*, **192**, 18.

Kormendy, J. (1977). Brightness distributions in compact and normal galaxies. II - Structure parameters of the spheroidal component. *ApJ*, **218**, 333.

Kormendy, J. & Bender, R. (2012). A Revised Parallel-sequence Morphological Classification of Galaxies: Structure and Formation of So and Spheroidal Galaxies. *ApJS*, **198**, 2.

Kormendy, J. & Gebhardt, K. 2001. Supermassive black holes in galactic nuclei. *Pages 363–381 of:* Wheeler, J. C. & Martel, H. (eds), *20th Texas Symposium on relativistic astrophysics*. American Institute of Physics Conference Series, vol. 586.

Kormendy, J. & Kennicutt, Jr., R. C. (2004). Secular Evolution and the Formation of Pseudobulges in Disk Galaxies. *ARA&A*, **42**, 603.

Kormendy, J., Fisher, D. B., Cornell, M. E. & Bender, R. (2009). Structure and Formation of Elliptical and Spheroidal Galaxies. *ApJS*, **182**, 216.

Lacey, C. & Cole, S. (1993). Merger rates in hierarchical models of galaxy formation. *MNRAS*, **262**, 627.

Landolt, A. U. (1992). UBVRI photometric standard stars in the magnitude range 11.5-16.0 around the celestial equator. *AJ*, **104**, 340.

Larson, R. B. (1974). Effects of supernovae on the early evolution of galaxies. *MNRAS*, **169**, 229.

Larson, R. B. (1976). Models for the formation of disc galaxies. *MNRAS*, **176**, 31.

Lee, J. C., Gil de Paz, A., Tremonti, C., *et al.* (2009). Comparison of Hα and UV Star Formation Rates in the Local Volume: Systematic Discrepancies for Dwarf Galaxies. *ApJ*, **706**, 599.

Lemaître, G. (1927). Un Univers homogène de masse constante et de rayon croissant rendant compte de la vitesse radiale des nébuleuses extra-galactiques. *Annales de la Societe Scietifique de Bruxelles*, **47**, 49.

Lemaître, G. (1931). The Beginning of the World from the Point of View of Quantum Theory. *Nature*, **127**, 706.

Li, C. & White, S. D. M. (2009). The distribution of stellar mass in the low-redshift Universe. *MNRAS*, **398**, 2177.

Lieder, S. (2010). *Diploma thesis*. University Library, Heidelberg.

Lieder, S., Lisker, T., Hilker, M., Misgeld, I. & Durrell, P. (2012). A deep view on the Virgo cluster core. *A&A*, **538**, A69.

Lieder, S., Mieske, S., Sánchez-Janssen, R., *et al.* (2013). A normal abundance of faint satellites in the fossil group NGC 6482. *A&A*, **559**, A76.

Lifshitz, E. (1946). On the Gravitational Stability of the Expanding Universe. *J. Phys. (USSR)*, **10**, 166.

Liivamägi, L. J., Tempel, E. & Saar, E. (2012). SDSS DR7 superclusters. The catalogues. *A&A*, **539**, A80.

Lin, D. N. C. & Faber, S. M. (1983). Some implications of nonluminous matter in dwarf spheroidal galaxies. *ApJ*, **266**, L21.

Lin, Y.-T. & Mohr, J. J. (2004). K-band Properties of Galaxy Clusters and Groups: Brightest Cluster Galaxies and Intracluster Light. *ApJ*, **617**, 879.

Linde, A., Linde, D. & Mezhlumian, A. (1994). From the big bang theory to the theory of a stationary universe. *Phys. Rev. D*, **49**, 1783.

Linde, A. D. (1982). A new inflationary universe scenario: A possible solution of the horizon, flatness, homogeneity, isotropy and primordial monopole problems. *Physics Letters B*, **108**, 389.

Linde, A. D. (1983). Chaotic inflation. *Physics Letters B*, **129**, 177.

Lisker, T., Grebel, E. K. & Binggeli, B. (2006). Virgo Cluster Early-Type Dwarf Galaxies with the Sloan Digital Sky Survey. I. On the Possible Disk Nature of Bright Early-Type Dwarfs. *AJ*, **132**, 497.

Lisker, T., Grebel, E. K., Binggeli, B. & Glatt, K. (2007). Virgo Cluster Early-Type Dwarf Galaxies with the Sloan Digital Sky Survey. III. Subpopulations: Distributions, Shapes, Origins. *ApJ*, **660**, 1186.

Lotz, J. M., Jonsson, P., Cox, T. J. & Primack, J. R. (2008). Galaxy merger morphologies and time-scales from simulations of equal-mass gas-rich disc mergers. *MNRAS*, **391**, 1137.

Lovell, M. R., Eke, V., Frenk, C. S., *et al.* (2012). The haloes of bright satellite galaxies in a warm dark matter universe. *MNRAS*, **420**, 2318.

Lynden-Bell, D. (1967). Statistical mechanics of violent relaxation in stellar systems. *MNRAS*, **136**, 101.

Lynden-Bell, D. (1969). Galactic Nuclei as Collapsed Old Quasars. *Nature*, **223**, 690.

Lyth, D. H. & Riotto, A. (1999). Particle physics models of inflation and the cosmological density perturbation. *Phys. Rep.*, **314**, 1.

Macciò, A. V., Paduroiu, S., Anderhalden, D., Schneider, A. & Moore, B. (2012). Cores in warm dark matter haloes: a Catch 22 problem. *MNRAS*, **424**, 1105.

Maddox, S. J., Efstathiou, G. & Sutherland, W. J. (1990). The APM Galaxy Survey - Part Two - Photometric Corrections. *MNRAS*, **246**, 433.

Mahdavi, A., Trentham, N. & Tully, R. B. (2005). The NGC 5846 Group: Dynamics and the Luminosity Function to $M_R = -12$. *AJ*, **130**, 1502.

Mateo, M. L. (1998). Dwarf Galaxies of the Local Group. *ARA&A*, **36**, 435.

Mather, J. C., Cheng, E. S., Eplee, Jr., R. E., *et al.* (1990). A preliminary measurement of the cosmic microwave background spectrum by the Cosmic Background Explorer (COBE) satellite. *ApJ*, **354**, L37.

Mathews, W. G. & Brighenti, F. (2003). Hot Gas in and around Elliptical Galaxies. *ARA&A*, **41**, 191.

Matthews, L. D. & Gallagher, III, J. S. (1997). B and V CCD Photometry of Southern, Extreme Late-Type Spiral Galaxies. *AJ*, **114**, 1899.

Mayer, L., Mastropietro, C., Wadsley, J., Stadel, J. & Moore, B. (2006). Simultaneous ram pressure and tidal stripping; how dwarf spheroidals lost their gas. *MNRAS*, **369**, 1021.

McCrea, W. H. (1968). Cosmology after Half a Century. *Science*, **160**, 1295.

McGaugh, S. S., Barker, M. K. & de Blok, W. J. G. (2003). A Limit on the Cosmological Mass Density and Power Spectrum from the Rotation Curves of Low Surface Brightness Galaxies. *ApJ*, **584**, 566.

McLaughlin, D. E. (1999). Evidence in Virgo for the Universal Dark Matter Halo. *ApJ*, **512**, L9.

Mendes de Oliveira, C. L., Cypriano, E. S. & Sodré, Jr., L. (2006). The Luminosity Function of the Fossil Group RX J1552.2+2013. *AJ*, **131**, 158.

Mendes de Oliveira, C. L., Cypriano, E. S., Dupke, R. A. & Sodré, Jr., L. (2009). An Optical and X-Ray Study of the Fossil Group RX J1340.6+4018. *AJ*, **138**, 502.

Méndez-Abreu, J., Aguerri, J. A. L., Barrena, R., *et al.* (2012). Fossil group origins. II. Unveiling the formation of the brightest group galaxies through their scaling relations. *A&A*, **537**, A25.

Merline, W. J. & Howell, S. B. (1995). A Realistic Model for Point-sources Imaged on Array Detectors: The Model and Initial Results. *Experimental Astronomy*, **6**, 163.

Merritt, D., Navarro, J. F., Ludlow, A. & Jenkins, A. (2005). A Universal Density Profile for Dark and Luminous Matter? *ApJ*, **624**, L85.

Merritt, D., Graham, A. W., Moore, B., Diemand, J. & Terzić, B. (2006). Empirical Models for Dark Matter Halos. I. Nonparametric Construction of Density Profiles and Comparison with Parametric Models. *AJ*, **132**, 2685.

Mihos, J. C., Harding, P., Feldmeier, J. & Morrison, H. (2005). Diffuse Light in the Virgo Cluster. *ApJ*, **631**, L41.

Miles, T. A., Raychaudhury, S., Forbes, D. A., *et al.* (2004). The Group Evolution Multiwavelength Study (GEMS): bimodal luminosity functions in galaxy groups. *MNRAS*, **355**, 785.

Milosavljević, M., Miller, C. J., Furlanetto, S. R. & Cooray, A. (2006). Cluster Merger Variance and the Luminosity Gap Statistic. *ApJ*, **637**, L9.

Misgeld, I. & Hilker, M. (2011). Families of dynamically hot stellar systems over 10 orders of magnitude in mass. *MNRAS*, **414**, 3699.

Misgeld, I., Mieske, S. & Hilker, M. (2008). The early-type dwarf galaxy population of the Hydra I cluster. *A&A*, **486**, 697.

Misgeld, I., Hilker, M. & Mieske, S. (2009). The early-type dwarf galaxy population of the Centaurus cluster. *A&A*, **496**, 683.

Misner, C. W. (1969). Mixmaster Universe. *Physical Review Letters*, **22**, 1071.

Miyazaki, S., Komiyama, Y., Sekiguchi, M., *et al.* (2002). Subaru Prime Focus Camera – Suprime-Cam. *PASJ*, **54**, 833.

Moore, B., Katz, N., Lake, G., Dressler, A. & Oemler, A. (1996). Galaxy harassment and the evolution of clusters of galaxies. *Nature*, **379**, 613.

Moore, B., Lake, G. & Katz, N. (1998). Morphological Transformation from Galaxy Harassment. *ApJ*, **495**, 139.

Moore, B., Ghigna, S., Governato, F., *et al.* (1999). Dark Matter Substructure within Galactic Halos. *ApJ*, **524**, L19.

Mulchaey, J. S. & Zabludoff, A. I. (1999). The Isolated Elliptical NGC 1132: Evidence for a Merged Group of Galaxies? *ApJ*, **514**, 133.

Naab, T., Khochfar, S. & Burkert, A. (2006). Properties of Early-Type, Dry Galaxy Mergers and the Origin of Massive Elliptical Galaxies. *ApJ*, **636**, L81.

Naab, T., Johansson, P. H. & Ostriker, J. P. (2009). Minor Mergers and the Size Evolution of Elliptical Galaxies. *ApJ*, **699**, L178.

Navarro, J. F., Frenk, C. S. & White, S. D. M. (1996). The Structure of Cold Dark Matter Halos. *ApJ*, **462**, 563.

Navarro, J. F., Hayashi, E., Power, C., *et al.* (2004). The inner structure of ΛCDM haloes - III. Universality and asymptotic slopes. *MNRAS*, **349**, 1039.

Navarro, J. F., Ludlow, A., Springel, V., *et al.* (2010). The diversity and similarity of simulated cold dark matter haloes. *MNRAS*, **402**, 21.

Omma, H., Binney, J., Bryan, G. & Slyz, A. (2004). Heating cooling flows with jets. *MNRAS*, **348**, 1105.

Oort, J. H. (1940). Some Problems Concerning the Structure and Dynamics of the Galactic System and the Elliptical Nebulae NGC 3115 and 4494. *ApJ*, **91**, 273.

Oser, L., Ostriker, J. P., Naab, T., Johansson, P. H. & Burkert, A. (2010). The Two Phases of Galaxy Formation. *ApJ*, **725**, 2312.

Oser, L., Naab, T., Ostriker, J. P. & Johansson, P. H. (2012). The Cosmological Size and Velocity Dispersion Evolution of Massive Early-type Galaxies. *ApJ*, **744**, 63.

Padmanabhan, T. (1993). *Structure Formation in the Universe*. Cambridge University Press, Cambridge.

Peebles, P. J. E. (1982). Large-scale background temperature and mass fluctuations due to scale-invariant primeval perturbations. *ApJ*, **263**, L1.

Peebles, P. J. E. & Dicke, R. H. (1968). Origin of the Globular Star Clusters. *ApJ*, **154**, 891.

Peebles, P. J. E. & Yu, J. T. (1970). Primeval Adiabatic Perturbation in an Expanding Universe. *ApJ*, **162**, 815.

Penny, S. J. & Conselice, C. J. (2008). Keck spectroscopy of the faint dwarf elliptical galaxy population in the Perseus Cluster core: mixed stellar populations and a flat luminosity function. *MNRAS*, **383**, 247.

Penzias, A. A. & Wilson, R. W. (1965). A Measurement of Excess Antenna Temperature at 4080 Mc/s. *ApJ*, **142**, 419.

Perlmutter, S. & Supernova Cosmology Project, t. (1999). Measurements of Omega and Lambda from 42 High-Redshift Supernovae. *ApJ*, **517**, 565.

Persic, M. & Salucci, P. (1988). Dark and visible matter in spiral galaxies. *MNRAS*, **234**, 131.

Phillipps, S., Driver, S. P., Couch, W. J. & Smith, R. M. (1998). The Luminosity Distribution in Galaxy Clusters: A Dwarf Population-Density Relation? *ApJ*, **498**, L119.

Planck Collaboration, T. (2013). Planck 2013 results. XVI. Cosmological parameters. *ArXiv e-prints*.

Pointecouteau, E., Arnaud, M. & Pratt, G. W. (2005). The structural and scaling properties of nearby galaxy clusters. I. The universal mass profile. *A&A*, **435**, 1.

Ponman, T. J., Allan, D. J., Jones, L. R., *et al.* (1994). A possible fossil galaxy group. *Nature*, **369**, 462.

Press, W. H. & Schechter, P. (1974). Formation of Galaxies and Clusters of Galaxies by Self-Similar Gravitational Condensation. *ApJ*, **187**, 425.

Proctor, R. N., de Oliveira, C. M., Dupke, R., *et al.* (2011). On the mass-to-light ratios of fossil groups. Are they simply dark clusters? *MNRAS*, **418**, 2054.

Quilis, V., Moore, B. & Bower, R. (2000). Gone with the Wind: The Origin of So Galaxies in Clusters. *Science*, **288**, 1617.

Read, J. I., Pontzen, A. P. & Viel, M. (2006). On the formation of dwarf galaxies and stellar haloes. *MNRAS*, **371**, 885.

Regan, M. W., Thornley, M. D., Helfer, T. T., *et al.* (2001). The BIMA Survey of Nearby Galaxies. I. The Radial Distribution of CO Emission in Spiral Galaxies. *ApJ*, **561**, 218.

Riess, A. G., Filippenko, A. V., Challis, P., *et al.* (1998). Observational Evidence from Supernovae for an Accelerating Universe and a Cosmological Constant. *AJ*, **116**, 1009.

Riess, A. G., Macri, L., Casertano, S., *et al.* (2009). A Redetermination of the Hubble Constant with the Hubble Space Telescope from a Differential Distance Ladder. *ApJ*, **699**, 539.

Rindler, W. (1956). Visual horizons in world models. *MNRAS*, **116**, 662.

Roberts, M. S. (1969). Integral Properties of Spiral and Irregular Galaxies. *AJ*, **74**, 859.

Robertson, H. P. (1929). On the Foundations of Relativistic Cosmology. *Proceedings of the National Academy of Science*, **15**, 822.

Roediger, E. & Hensler, G. (2005). Ram pressure stripping of disk galaxies. From high to low density environments. *A&A*, **433**, 875.

Roeser, S., Demleitner, M. & Schilbach, E. (2010). The PPMXL Catalog of Positions and Proper Motions on the ICRS. Combining USNO-B1.0 and the Two Micron All Sky Survey (2MASS). *AJ*, **139**, 2440.

Rubin, V. C., Thonnard, N. & Ford, Jr., W. K. (1978). Extended rotation curves of high-luminosity spiral galaxies. IV - Systematic dynamical properties, SA through SC. *ApJ*, **225**, L107.

Sakai, S., Mould, J. R., Hughes, S. M. G., *et al.* (2000). The Hubble Space Telescope Key Project on the Extragalactic Distance Scale. XXIV. The Calibration of Tully-Fisher Relations and the Value of the Hubble Constant. *ApJ*, **529**, 698.

Sakharov, A. D. (1967). Violation of CP Invariance, C Asymmetry, and Baryon Asymmetry of the Universe. *Soviet Journal of Experimental and Theoretical Physics Letters*, **5**, 24.

Sales, L. V., Navarro, J. F., Lambas, D. G., White, S. D. M. & Croton, D. J. (2007). Satellite galaxies and fossil groups in the Millennium Simulation. *MNRAS*, **382**, 1901.

Sánchez, A. G., Baugh, C. M., Percival, W. J., *et al.* (2006). Cosmological parameters from cosmic microwave background measurements and the final 2dF Galaxy Redshift Survey power spectrum. *MNRAS*, **366**, 189.

Sánchez-Janssen, R., Iglesias-Páramo, J., Muñoz-Tuñón, C., Aguerri, J. A. L. & Vílchez, J. M. (2005). The V-band luminosity function of galaxies in A2151. *A&A*, **434**, 521.

Sánchez-Janssen, R., Aguerri, J. A. L. & Muñoz-Tuñón, C. (2008). Properties of the Dwarf Galaxy Population in Galaxy Clusters. *ApJ*, **679**, L77.

Sand, D. J., Treu, T., Smith, G. P. & Ellis, R. S. (2004). The Dark Matter Distribution in the Central Regions of Galaxy Clusters: Implications for Cold Dark Matter. *ApJ*, **604**, 88.

Sandage, A. & Bedke, J. (1994). *The Carnegie Atlas of Galaxies. Volumes I, II.*

Sandage, A. & Binggeli, B. (1984). Studies of the Virgo cluster. III - A classification system and an illustrated atlas of Virgo cluster dwarf galaxies. *AJ*, **89**, 919.

Sandage, A., Binggeli, B. & Tammann, G. A. (1985). Studies of the Virgo Cluster - Part Five - Luminosity Functions of Virgo Cluster Galaxies. *AJ*, **90**, 1759.

Sanderson, A. J. R., Ponman, T. J., Finoguenov, A., Lloyd-Davies, E. J. & Markevitch, M. (2003). The Birmingham-CfA cluster scaling project - I. Gas fraction and the M-T_X relation. *MNRAS*, **340**, 989.

Santos, W. A., Mendes de Oliveira, C. & Sodré, Jr., L. (2007). Fossil Groups in the Sloan Digital Sky Survey. *AJ*, **134**, 1551.

Schechter, P. (1976). An analytic expression for the luminosity function for galaxies. *ApJ*, **203**, 297.

Schlegel, D. J., Finkbeiner, D. P. & Davis, M. (1998). Maps of Dust Infrared Emission for Use in Estimation of Reddening and Cosmic Microwave Background Radiation Foregrounds. *ApJ*, **500**, 525.

Schwarzschild, M. (1946). On the Helium Content of the Sun. *ApJ*, **104**, 203.

Searle, L. & Zinn, R. (1978). Compositions of halo clusters and the formation of the galactic halo. *ApJ*, **225**, 357.

Secker, J., Harris, W. E. & Plummer, J. D. (1997). Dwarf Galaxies in the Coma Cluster. II. Photometry and Analysis. *PASP*, **109**, 1377.

Sérsic, J. L. (1963). Influence of the atmospheric and instrumental dispersion on the brightness distribution in a galaxy. *Boletin de la Asociacion Argentina de Astronomia La Plata Argentina*, **6**, 41.

Sersic, J. L. (1968). *Atlas de galaxias australes*.

Shandarin, S. F., Doroshkevich, A. G. & Zel'dovich, Y. B. (1983). REVIEWS OF TOPICAL PROBLEMS: The large-scale structure of the universe. *Soviet Physics Uspekhi*, **26**, 46.

Shapley, H. (1938). Two Stellar Systems of a New Kind. *Nature*, **142**, 715.

Shapley, H. (1951). Comparison of the Magellanic Clouds with the Galactic System. *Publications of the Michigan Observatory*, **10**, 79.

Sijacki, D., Springel, V., Di Matteo, T. & Hernquist, L. (2007). A unified model for AGN feedback in cosmological simulations of structure formation. *MNRAS*, **380**, 877.

Silk, J. (1968). Cosmic Black-Body Radiation and Galaxy Formation. *ApJ*, **151**, 459.

Simon, J. D. & Geha, M. (2007). The Kinematics of the Ultra-faint Milky Way Satellites: Solving the Missing Satellite Problem. *ApJ*, **670**, 313.

Smith, R. E. & Markovic, K. (2011). Testing the warm dark matter paradigm with large-scale structures. *Phys. Rev. D*, **84(6)**, 063507.

Smith, R. J., Lucey, J. R., Hudson, M. J., Schlegel, D. J. & Davies, R. L. (2000). Streaming motions of galaxy clusters within 12000kms^{-1} - I. New spectroscopic data. *MNRAS*, **313**, 469.

Smoot, G. F., Bennett, C. L., Kogut, A., Wright, E. L. & al., e. (1992). Structure in the COBE differential microwave radiometer first-year maps. *ApJ*, **396**, L1.

Somerville, R. S. & Primack, J. R. (1999). Semi-analytic modelling of galaxy formation: the local Universe. *MNRAS*, **310**, 1087.

Somerville, R. S., Primack, J. R. & Faber, S. M. (2001). The nature of high-redshift galaxies. *MNRAS*, **320**, 504.

Somerville, R. S., Lee, K., Ferguson, H. C., *et al.* (2004). Cosmic Variance in the Great Observatories Origins Deep Survey. *ApJ*, **600**, L171.

Spekkens, K., Giovanelli, R. & Haynes, M. P. (2005). The Cusp/Core Problem in Galactic Halos: Long-Slit Spectra for a Large Dwarf Galaxy Sample. *AJ*, **129**, 2119.

Spergel, D. N., Verde, L., Peiris, H. V., *et al.* (2003). First-Year Wilkinson Microwave Anisotropy Probe (WMAP) Observations: Determination of Cosmological Parameters. *ApJS*, **148**, 175.

Springel, V. & Hernquist, L. (2005). Formation of a Spiral Galaxy in a Major Merger. *ApJ*, **622**, L9.

Springel, V., White, S. D. M., Tormen, G. & Kauffmann, G. (2001). Populating a cluster of galaxies - I. Results at $z = 0$. *MNRAS*, **328**, 726.

Springel, V., Di Matteo, T. & Hernquist, L. (2005a). Modelling feedback from stars and black holes in galaxy mergers. *MNRAS*, **361**, 776.

Springel, V., White, S. D. M., Jenkins, A., *et al.* (2005b). Simulations of the formation, evolution and clustering of galaxies and quasars. *Nature*, **435**, 629.

Stanek, R., Rasia, E., Evrard, A. E., Pearce, F. & Gazzola, L. (2010). Massive Halos in Millennium Gas Simulations: Multivariate Scaling Relations. *ApJ*, **715**, 1508.

Strigari, L. E., Bullock, J. S., Kaplinghat, M., *et al.* (2007). Redefining the Missing Satellites Problem. *ApJ*, **669**, 676.

Strigari, L. E., Bullock, J. S., Kaplinghat, M., *et al.* (2008a). A common mass scale for satellite galaxies of the Milky Way. *Nature*, **454**, 1096.

Strigari, L. E., Koushiappas, S. M., Bullock, J. S., *et al.* (2008b). The Most Dark-Matter-dominated Galaxies: Predicted Gamma-Ray Signals from the Faintest Milky Way Dwarfs. *ApJ*, **678**, 614.

Sunyaev, R. A. & Zeldovich, Y. B. (1970). Small-Scale Fluctuations of Relic Radiation. *Ap&SS*, **7**, 3.

Suzuki, N., Rubin, D., Lidman, C. & the Supernova Cosmology Project. (2012). The Hubble Space Telescope Cluster Supernova Survey. V. Improving the Dark-energy Constraints above $z > 1$ and Building an Early-type-hosted Supernova Sample. *ApJ*, **746**, 85.

Thomas, D., Maraston, C., Bender, R. & Mendes de Oliveira, C. (2005). The Epochs of Early-Type Galaxy Formation as a Function of Environment. *ApJ*, **621**, 673.

Tolstoy, E., Hill, V. & Tosi, M. (2009). Star-Formation Histories, Abundances, and Kinematics of Dwarf Galaxies in the Local Group. *ARA&A*, **47**, 371.

Toomre, A. 1977. Mergers and Some Consequences. *Page 401 of:* Tinsley, B. M. & Larson, D. Campbell, R. B. G. (eds), *Evolution of Galaxies and Stellar Populations*.

Toomre, A. & Toomre, J. (1972). Galactic Bridges and Tails. *ApJ*, **178**, 623.

Tremblay, P.-E. & Bergeron, P. (2008). The Ratio of Helium- to Hydrogen-Atmosphere White Dwarfs: Direct Evidence for Convective Mixing. *ApJ*, **672**, 1144.

Trentham, N. & Tully, R. B. (2002). The faint end of the galaxy luminosity function. *MNRAS*, **335**, 712.

Tully, R. B. & Fisher, J. R. (1977). A new method of determining distances to galaxies. *A&A*, **54**, 661.

Tytler, D., O'Meara, J. M., Suzuki, N. & Lubin, D. (2000). Review of Big Bang Nucleosynthesis and Primordial Abundances. *Physica Scripta Volume T*, **85**, 12.

Unsöld, A. (1944). Quantitative Analyse des Bo-Sternes Tau Scorpii. IV. Druckverbreiterung der He und He^+ Linien. Eine neue Methode zur Bestimmung des Häufigkeitsverhältnisses von Wasserstoff und Helium. *ZAp*, **23**, 75.

Urban, O., Werner, N., Simionescu, A., Allen, S. W. & Böhringer, H. (2011). X-ray spectroscopy of the Virgo Cluster out to the virial radius. *MNRAS*, **414**, 2101.

van Albada, T. S., Bahcall, J. N., Begeman, K. & Sancisi, R. (1985). Distribution of dark matter in the spiral galaxy NGC 3198. *ApJ*, **295**, 305.

van den Bergh, S. (1976). A new classification system for galaxies. *ApJ*, **206**, 883.

van den Bosch, F. C., Yang, X., Mo, H. J., *et al.* (2007). Towards a concordant model of halo occupation statistics. *MNRAS*, **376**, 841.

van Dokkum, P. G. (2005). The Recent and Continuing Assembly of Field Elliptical Galaxies by Red Mergers. *AJ*, **130**, 2647.

Vikhlinin, A., Kravtsov, A., Forman, W., *et al.* (2006). Chandra Sample of Nearby Relaxed Galaxy Clusters: Mass, Gas Fraction, and Mass-Temperature Relation. *ApJ*, **640**, 691.

Vollmer, B. (2009). A holistic view on ram pressure stripping in the Virgo cluster. The first complete model-based time sequence. *A&A*, **502**, 427.

Vollmer, B., Cayatte, V., Balkowski, C. & Duschl, W. J. (2001). Ram Pressure Stripping and Galaxy Orbits: The Case of the Virgo Cluster. *ApJ*, **561**, 708.

von Benda-Beckmann, A. M., D'Onghia, E., Gottlöber, S., *et al.* (2008). The fossil phase in the life of a galaxy group. *MNRAS*, **386**, 2345.

Walker, A. G. (1935). On Riemanntan spaces with spherical symmetry about a line, and the conditions for isotropy in genj relativity. *The Quarterly Journal of Mathematics*, **6**, 81.

Weinberg, S. (1972). *Gravitation and Cosmology*. Wiley, New York.

Weinmann, S. M., Lisker, T., Guo, Q., Meyer, H. T. & Janz, J. (2011). Dwarf galaxy populations in present-day galaxy clusters - I. Abundances and red fractions. *MNRAS*, **416**, 1197.

White, S. D. M. & Frenk, C. S. (1991). Galaxy formation through hierarchical clustering. *ApJ*, **379**, 52.

White, S. D. M. & Rees, M. J. (1978). Core condensation in heavy halos - A two-stage theory for galaxy formation and clustering. *MNRAS*, **183**, 341.

White, S. D. M., Davis, M. & Frenk, C. S. (1984). The size of clusters in a neutrino-dominated universe. *MNRAS*, **209**, 27P.

Worthey, G. (1994). Comprehensive stellar population models and the disentanglement of age and metallicity effects. *ApJS*, **95**, 107.

Yang, X., Mo, H. J. & van den Bosch, F. C. (2008). Galaxy Groups in the SDSS DR4. II. Halo Occupation Statistics. *ApJ*, **676**, 248.

Zabludoff, A. I. & Mulchaey, J. S. (1998). The Properties of Poor Groups of Galaxies. I. Spectroscopic Survey and Results. *ApJ*, **496**, 39.

ZANDIVAREZ, A. & MARTÍNEZ, H. J. (2011). Luminosity function of galaxies in groups in the Sloan Digital Sky Survey Data Release 7: the dependence on mass, environment and galaxy type. *MNRAS*, **415**, 2553.

ZARATTINI, S., BARRENA, R., GIRARDI, M., *et al.* (2014). Fossil Groups Origins III. Characterization of the sample and observational properties of fossil systems. *ArXiv e-prints*.

ZEL'DOVICH, Y. B. (1970). Gravitational instability: An approximate theory for large density perturbations. *A&A*, **5**, 84.

ZWICKY, F. (1933). Die Rotverschiebung von extragalaktischen Nebeln. *Helvetica Physica Acta*, **6**, 110.

ZWICKY, F., HERZOG, E. & WILD, P. (1963). *Catalogue of galaxies and of clusters of galaxies, Vol. 2*.

ACKNOWLEDGMENTS

Based on data collected at Subaru Telescope, which is operated by the National Astronomical Observatory of Japan, under run ID S08B-150S.

This research has made use of the NASA/IPAC Extragalactic Database (NED) which is operated by the Jet Propulsion Laboratory, California Institute of Technology, under contract with the National Aeronautics and Space Administration.

SQL databases containing the full galaxy data for the semi-analytic model of Guo *et al.* (2011) at all redshifts and for both the Millennium and Millennium-II Simulation used in this work and the web application providing online access to them were constructed as part of the activities of the German Astrophysical Virtual Observatory (GAVO).

IRAF is distributed by the National Optical Astronomy Observatory, which is operated by the Associated Universities for Research in Astronomy, Inc., under cooperative agreement with the National Science Foundation.

This thesis has made use of SExtractor (Bertin & Arnouts 1996), and THELI (Erben *et al.* 2005).

This research has made use of NASA's Astrophysics Data System.

ACRONYMS

A/D	Analog-to-Digital (converter)
AGN	Active Galactic Nucleus
BAO	Baryon Acoustic Oscillations
BCG	Brightest Cluster Galaxy
BGG	Brightest Group Galaxy
B/T	Bulge-to-Total (ratio)
CCD	Charge-Coupled Device
CDM	Cold Dark Matter
CMB	Cosmic Microwave Background
CMD	Color-Magnitude Diagram
CMR	Color-Magnitude Relation
COBE	COsmic Background Explorer
d/g	Dwarf-to-Giant (ratio)
DM	Dark Matter
FG	Fossil Group
FLRW	Friedmann-Lemaître-Robertson-Walker (metric)
FOF	Friend-Of-Friends (algorithm)
HST	Hubble Space Telescope
HST	Hawaii Standard Time
ICM	Intra-Cluster Medium
LF	Luminosity Function
MS	Millennium Simulation
MS-II	Millennium-II Simulation
NFW	Navarro-Frenk-White (profile)
PSF	Point Spread Function
RMS	Root Mean Square
RS	Red Sequence
SAM	Semi-Analytic Model
SB	Surface Brightness
SDSS	Sloan Digital Sky Survey
SFH	Star Formation History
SFR	Star Formation Rate
SSFR	Specific Star Formation Rate
S/N	Signal-to-Noise (ratio)
SN	SuperNova